Mesozoic Rift Evolution and Crustal Structure of the Gulf of Mexico Basin from Integration of Multiple Geological and Geophysical Datasets

by
Mei Liu

A dissertation submitted to the Department of Earth and Atmospheric Sciences,
College of Natural Sciences and Mathematics
in partial fulfillment of the requirements for the degree of

Doctor of Philosophy

in Geology

Chair of Committee: Paul Mann

Committee Member: Dale Bird

Committee Member: William Sager

Committee Member: Anahita Tikku

University of Houston
August 2021

Copyright 2021, Mei Liu

ACKNOWLEDGMENTS

I am grateful to Dr. Paul Mann for his guidance and support on my dissertation and his supervision throughout my three-year graduate career at the University of Houston. His knowledge, experience, philosophy, and passion encouraged and influenced me deeply and profoundly. I thank the industry sponsors of the Conjugate Basins, Tectonics, and Hydrocarbons (CBTH) for their financial support for my graduate research assistantship and travel support during this study. Special thanks to Drs. Dale Bird, Will Sager, and Anahita Tikku for their service on my dissertation committee and their willingness to provide contributions to my research.

I thank Mike Saunders at Spectrum Geo, Inc (now TGS) for providing the seismic reflection data and Scott Paton from Bell Geospace for providing the full tensor gravity gradient data that was used in this dissertation.

I would like to thank the numerous academic researchers, industry professionals, and CBTH graduate and undergraduate students who contributed their support and insights for this project.

Finally, I would like to thank my family and friends for their support throughout my graduate career.

ABSTRACT

The Gulf of Mexico basin (GOM) is one of the most prolific, hydrocarbon-producing basins in the world. However, our understanding of the Triassic-Jurassic rift history and crustal structure of the GOM is limited. This dissertation integrates free-air gravity data, full-tensor gravity gradient data, 104,000 line-kilometers of 2D reflection data, and refraction data and deep wells over 4.2 million km^2 to improve our understanding of the GOM rift history.

Chapter 1 summarizes the development of this study. In **Chapter 2**, 2D gravity models are used to constrain two zones of southward-dipping reflectors associated with 7-10 km, dense and magnetic material. The marginal rift width varies from 28 km to 42 km in both models and was formed during a tectonic transition from late Triassic-early Jurassic, northwest-to-southeast rifting to late Jurassic north-south rifting. In **Chapter 3**, I test two GOM opening models by integrating reflection data, refraction data, gravity data, and well data from the greater GOM area. Inversion of gravity data for crustal thickness used constraints from 178 refraction stations to produce a regional map of crustal domains. The best full-fit restoration was achieved using the two-phase model that consists of a first phase of Triassic-early Jurassic, northwest-southeast continental rifting followed by a second phase of late Jurassic north-south rifting and oceanic crust formation.

In **Chapter 4**, I use 12 2D seismic profiles from the northeastern GOM and northern Yucatan to map the 1056-km-long marginal rift system that is adjacent to the late Jurassic oceanic crust of the central GOM. Analysis of the seismic, gravity, and magnetic data shows the crust underlying the marginal rift is thinned continental crust formed by necking of the continental crust. 2D gravity models show that the marginal rift sedimentary fill consists of volcaniclastic and

sedimentary rocks. In **Chapter 5**, full tensor gravity gradient was used to model the base of salt and geometry of the salt canopy in the north-central US GOM. The components Txz and Tyz were used to interpret the edges of the salt canopy.

Table of Contents

LIST OF FIGURES

LIST OF TABLES

CHAPTER 1: INTRODUCTION TO THIS DISSERTATION

1.1 History and development of this dissertation

I was born and raised in Xianyang, China, a city of 1.7 million people that is located in the central Shaanxi Province of western China. Xianyang was once the historical capital of the Qin dynasty (221-206 BC) that was the first dynasty of Imperial China. The city is best known for the Terracotta Army, a collection of thousands of terracotta sculptures depicting the armies of the Chinese emperor that were part of his much larger necropolis that has now been excavated by archeologists.

BS and MS study at the University of Nebraska (2014-2018)

I took geology courses at the University of Nebraska in geology starting in August 2014 and attended departmental field camp in Shell, Wyoming for the first six weeks of the summer of 2015. During the latter part of the summer of 2015, I was an intern with the CNPC Great Wall Drilling Company in Beijing, China, where I worked on a well database from the Melut Basin, in South Sudan, Central Africa. I completed my bachelor of science degree in geology at the University of Nebraska and graduated in December 2016.

I was mentored as an undergraduate student and encouraged to continue as an MS student in geology and geophysics by Dr. Irina Filina, who had left the oil industry in Houston, Texas, and arrived at the University of Nebraska as an assistant professor in 2016, where she had taught my undergraduate geophysics class in fall 2016. I began the MS program in geology in January 2017 and was supported as a research assistant under a grant from Dr. Filina from January 2017 to

January 2018 and as a graduate teaching assistant from the geology department for the physical geology course from January 2018 to May 2018. I worked in the research group of Dr. Filina and my MS project that was entitled “Integrated Geophysical Analysis in the northeastern Gulf of Mexico." For this study, I used gravity modeling and seismic reflection data to better understand the crustal structure of the northern US Gulf of Mexico, which was the main research focus of Dr. Filina’s research group of graduate and undergraduate students.

At the University of Nebraska, I presented the results of MS research at five conferences as summarized in Table 1. I am including these here to show how the MS research under Dr. Filina formed the foundation for my Ph.D. study at the University of Houston. I received a student travel grant from GSA to attend the GSA Annual meeting in 2017 and I received a Best Earth Science presentation award from the Nebraska Geological Society in 2017.

Table 1. Presentations from MS research supervised by Dr. Irina Filina at the University of Nebraska:

Event	Title of presentation	Date/Award
University of Nebraska Research Fair	Potential fields modeling in the northeastern Gulf of Mexico	April 5, 2017
Nebraska Academy of Sciences	Integrated geophysical studies in the northeastern Gulf of Mexico	April 21, 2017 Award for Best Earth Science presentation
GSA Annual Meeting (Seattle, Washington)	Delineation of crustal domains in the northeastern Gulf of Mexico from integrated geophysical analysis	October 23, 2017 GSA student travel award
AGU Annual Meeting (New Orleans, Louisiana)	Variations of oceanic crust in the northeastern Gulf of Mexico from integrated geophysical analysis	December 12, 2017
AAPG ACE Annual Meeting (Salt Lake City, Utah)	Potential fields modeling in the northeastern Gulf of Mexico	May 21, 2018

Through the encouragement of Dr. Filina and other faculty members at the University of Nebraska, I decided to apply for Ph.D. programs to continue my education in geosciences and my

research on the Gulf of Mexico tectonic history. In February of 2018, I visited Dr. Paul Mann and the CBTH project at the University of Houston and was accepted into the Ph.D. program in August 2018.

Ph.D. study at the University of Houston (2018-2021)

During the fall of 2018, I started on a manuscript (Chapter 2 of this dissertation) that combined gravity modeling results from my University of Nebraska master's thesis on the northeastern Gulf of Mexico with deep-penetration seismic reflection data that I was able to access through a data-sharing agreement between Spectrum (now TGS) in Houston, Texas, and Dr. Mann and the CBTH project at the University of Houston. I thank Mike Saunders from Spectrum (now at TGS) for his support in accessing these and other important seismic reflection data used in this dissertation. This paper was submitted to the journal *Interpretation* in December 2018, was revised in the fall of 2019, and published in November 2019. The journal reviewers for *Interpretation* included Drs. Erin Beutel (College of Charleston, South Carolina), Randy Keller (University of Oklahoma), and Cian O'Reilly (TGS, Houston).

During the summer and fall of 2019, I worked at the offices of Spectrum in Houston, Texas, to compile other seismic reflection lines for the chapters of this dissertation on the crustal thickness map and reconstruction of the entire GOM (Chapter 3) and the GOM marginal rift system on both the Florida and Yucatan conjugate margins (Chapter 4). These chapters made use of the following Spectrum (now TGS) seismic reflection datasets: Deep East survey acquired in 2007, regional Mexico 2D survey acquired in 2015, and Yucatan regional seismic reflection dataset acquired in (2015). I also integrate some results from the Dynamic deep-penetration SuperCache seismic data set that was acquired in 2011-2012 and provided to me in the February of 2021 through a data-

sharing agreement between Dynamic in Houston, Texas, and Dr. Mann and the CBTH project at the University of Houston. I thank Dr. Peter Nuttall of Dynamic for his assistance with the SuperCache data.

The work of previous UH and CBTH students benefitted and helped focus Chapters 3 and 4 of this dissertation. My crustal thickness study in Chapter 3 grew out of the previous research by former UH BS and MS student Luan Nguyen that included GOM basin-wide gravity and magnetic mapping (Nguyen and Mann, 2015) and a previous Ph.D. dissertation by Pin Lin that included gravity mapping and modeling of the eastern GOM (Lin, Ph.D., 2018).

In November of 2018, I presented at the Sheriff conference and met Scott Paton of Bell Geospace, who kindly offered the use of their full-tensor gravity (FTG) gradient data from the north-central GOM that I used in Chapter 5 of this dissertation. I greatly appreciate the efforts of Scott Paton and his colleague at Bell Geospace, Dr. Alan Morgan, for their efforts in making this cutting-edge, FTG gravity data set available for my research at the University of Houston. I also greatly appreciate the supervision of Dr. Dale Bird on this chapter, which has been submitted for publication in June 2021 to the Journal of Applied Geophysics.

In 2019 and 2020, I continued to collaborate with Dr. Filina and Dr. Erin Beutel and co-authored a paper published in the journal *Tectonophysics* in 2019 that is entitled: *Evidence of ridge propagation in the eastern Gulf of Mexico from integrated analysis of potential fields and seismic data*. As I was a second author and many of these results were based on work at the University of Nebraska, I did not include this work as part of this dissertation.

In April-June, 2019, I volunteered to participate in a 40-day marine geophysical cruise on the RV *Marcus Langseth* that was led by Drs. Donna Shillington (Northern Arizona University), Dr. Robert Dunn (the University of Hawaii at Manoa), and Dr. Tony Watts (Oxford University).

The cruise left from Honolulu, Hawaii, on April 21, 2019, and surveyed the Emperor seamount chain in the central Pacific Ocean, and returned to Kodiak, Alaska, on June 3, 2019. During the cruise, I processed multi-channel seismic reflection data and swath bathymetry data, assisted in recoveries of ocean bottom seismometers and XBTs, and stood scientific watches in the lab area. I greatly appreciate the mentorship of Drs. Shillington, Dunn, and Watts and for providing me the opportunity to participate in the cruise and improve my understanding of the acquisition and processing of marine geophysical data.

During the three-year period of this dissertation, I have made 27 presentations on my GOM research that included four national and six international conferences along with 17 in-person or online visits to the offices of the company sponsors of the CBTH consortium. Constructive feedback gained from these meetings was instrumental in the improvement of the quality of my research. I greatly appreciate the financial support from Dr. Mann and the CBTH project that covered my registration and travel costs for attending these meetings. I also thank Jon Blickwede (Meeting co-convenor) and AAPG for providing my registration and travel cost to attend the AAPG Hedburg Conference on the GOM in Mexico City in February 2020. The presentations and meetings attended in relation to the Ph.D. study are summarized below:

Event	**Title of presentation**	**Date/Award**
AAPG Student Expo, Houston, TX	New regional gravity constraints on two phases of Late Jurassic oceanic spreading in the eastern Gulf of Mexico	September 13, 2018
CBTH Year-End Meeting, University of Houston	New potential fields constraints on ridge reorganization of late Jurassic oceanic spreading in the eastern Gulf of Mexico	September 21, 2018

HGS Sheriff Lecture, Houston, TX	New potential fields constraints on ridge reorganization of late Jurassic oceanic spreading in the eastern Gulf of Mexico	November 12, 2018
American Geophysical Union Fall Meeting (San Francisco, CA)	Two extinct spreading centers in the eastern Gulf of Mexico from integrated geophysical analysis	December 8, 2018
CBTH Mid-Year Meeting, University of Houston	Oceanic crustal architecture in the western Gulf of Mexico	March 22, 2019
Visit by CBTH to Chevron office, Houston, TX	New constraints on crustal structure of the Gulf of Mexico	April 9, 2019
AAPG Student Expo, Houston, TX	Crustal structure of Mesozoic rifting in the northeastern Gulf of Mexico from integration of seismic and potential fields data	September 5, 2019
CBTH Year-End Meeting, University of Houston	Oceanic crustal architecture and its marginal rifts from integration of marine seismic reflection, refraction, and gravity data	September 27, 2019
Gulf Coast Association of Geological Societies conference (now called GeoGulf), Houston, TX	Crustal structure of oceanic crust in the western Gulf of Mexico from integration of marine seismic reflection, refraction, and gravity data	October 24, 2019 Awarded Second Place Poster award https://www.uh.edu/nsm/earth-atmospheric/news-events/stories/2019/1122-poster-award.php
CBTH visit to Kosmos, Houston, TX (online)	Crustal architecture of Gulf of Mexico, Late Jurassic, oceanic crust and significance of the marginal rift system during Gulf of Mexico opening	November 7, 2019
HGS Sheriff Lecture, Houston, TX	Crustal architecture of Gulf of Mexico, Late Jurassic, oceanic crust and significance of the marginal rift system during Gulf of Mexico opening	November 11, 2019
American Geophysical Union Fall Meeting (San Francisco, CA)	Geophysical framework of the extinct Jurassic spreading center in the Gulf of Mexico: an integration of marine seismic reflection, refraction, and gravity data	December 7, 2019
AAPG Hedburg Conference: Geology and Hydrocarbon	Marginal rift system along late Jurassic, conjugate margins of	February 4, 2020

Potential of the Circum Gulf of Mexico Pre-salt Section, Mexico City, Mexico	the Gulf of Mexico: rift continuity, age, and tectonic significance	
Visits by CBTH to Oxy, Houston, TX (online)	Crustal architecture of Gulf of Mexico, Late Jurassic, oceanic crust and significance of the Marginal Rift System during Gulf of Mexico opening	March 19, 2020
Visits by CBTH to Exxon, Houston, TX (online)	Crustal architecture of Gulf of Mexico, Late Jurassic, oceanic crust and significance of the Marginal Rift System during Gulf of Mexico opening	March 20, 2020
Visits by CBTH to Total, Houston, TX (online)	Crustal architecture of Gulf of Mexico, Late Jurassic, oceanic crust and significance of the Marginal Rift System during Gulf of Mexico opening	April 9, 2020
Visits by CBTH to Shell, Houston, TX (online)	Crustal architecture of Gulf of Mexico, Late Jurassic, oceanic crust and significance of the Marginal Rift System during Gulf of Mexico opening	April 29, 2020
Visits by CBTH to Hess, Houston, TX (online)	Crustal structure of the greater Gulf of Mexico area and its relation to the two-phase basin opening model	May 21, 2020
Visits to BellGeospace, Houston, TX (online)	Crustal thickness mapping and salt modeling of the Gulf of Mexico	July 30, 2020
AAPG Southeast Caribbean Virtual Conference (online)	Using regional gravity model to define the crustal setting of recent, giant oil discoveries in Guyana and Suriname	September 17, 2020
CBTH Year-End Meeting, University of Houston	Crustal structure of the greater Gulf of Mexico area and its relation to the two phase basin opening model	September 25, 2020
AAPG ACE Annual Meeting (online)	Regional extent and tectonic origin of the Mesozoic marginal rift system of the deep water Gulf of Mexico basin	September 29, 2020
Visits to Seequent (North America and UK group) (Invited talk - online)	Crustal thickness mapping and salt modeling of the Gulf of Mexico	October 6, 2020
HGS Sheriff Student Poster Presentations (online)	Regional extent and tectonic origin of the Mesozoic	November 9, 2020

	marginal rift system of the deep water Gulf of Mexico basin	
American Geophysical Union Fall Meeting (online)	Distribution and thickness of crustal types of the greater Gulf of Mexico region based on constrained 3D gravity inversion	December 15, 2020
Baton Rouge Geological Society (Invited - online)	Crustal thickness of the greater Gulf of Mexico region based on constrained 3D gravity inversion and its implication on the tectonic history	January 8, 2021
UH Student Research Day, University of Houston (online)	Crustal thickness variations of the greater Gulf of Mexico region from integrated geological and geophysical analysis	April 30, 2021

1.2 Rationale, topics, and organization of this dissertation

The purpose of this dissertation is to improve understanding of how regional tectonic events have controlled or influenced the Mesozoic structure of rifted continental crust of the Gulf of Mexico. This dissertation includes three chapters focused on the crustal structure of the Gulf of Mexico and one chapter focused on salt mapping using full tensor gravity gradient data.

The four chapters of this dissertation addresses these topics:

Chapter 2 delineates the crustal structure in the northeastern Gulf of Mexico using potential fields models integrated with deep-penetration seismic reflection data. Chapter 2 has been published as Liu, M., Filina, I., and Mann, P., 2019, Crustal structure of Mesozoic rifting in the northeastern Gulf of Mexico from integration of seismic and potential fields data. *Interpretation*, vol. 7, No. 4, 857-867.

Chapter 3 uses an integration of subsurface mapping from seismic reflection data and integration with gravity models to understand the tectonic origin of the Mesozoic marginal rift

system that is present along the conjugate margins of Florida and Yucatan. Chapter 3 is in preparation for the journal *Tectonophysics*.

Chapter 4 uses 3D gravity inversion to make a regional map of the variations in crustal types and thicknesses of the Greater Gulf of Mexico region in the context of its Mesozoic tectonic framework. Chapter 4 is in preparation for the journal *Marine and Petroleum Geology*.

Chapter 5 used full tensor gravity gradient data from the north-central Gulf of Mexico to map the edges of remobilized Mesozoic. Chapter 5 was submitted on June 7, 2021 to the Journal *of Applied Geophysics*.

1.2.1 Summary of Chapter 2

Chapter 2 investigates the crustal structure of a 400-km-wide zone of thinned continental crust in the northeastern Gulf of Mexico (GOM) using gravity and magnetic modeling along two deep-penetration seismic transects. Using this approach, two zones of prominent, southward-dipping reflectors are inferred to be a 7–10 km thick layer of dense and highly magnetic, igneous rock. Previous workers have interpreted the zones as either coarse clastic redbeds of Mesozoic age that are tilted within half-grabens or seaward-dipping reflectors of magmatic origin. I support the latter interpretation based on the information I present in this chapter.

Two seismic reflection lines reveal a 10-km-thick and 67-km-wide northern zone of high density that corresponds to the Apalachicola rift (AR) near the coastline of the Florida panhandle coastline of the GOM. The southern zone of high density occurs 70 km to the south in the deep-water central GOM along the northern flank of the marginal rift, a 48-km-wide, southeast trending structure of inferred Late Jurassic age that is filled by 3 km of low-density and low-magnetic

susceptibility sediments including complexly deformed salt deposits. I propose that these two subparallel rifts and their associated magmatic belts formed in the following sequence: (1) AR formed during Triassic-early Jurassic (210–163 Ma) phase 1 of diffuse continental stretching and was partially infilled on its northern edge by southward-dipping volcanic flows; and (2) the similarly southward-dipping southern magmatic zone formed adjacent to the marginal rift during the early phase 2 of late Jurassic (161–153 Ma) rifting of the GOM continental extension; this southern area of SDR formation preceded the formation of the adjacent oceanic crust that separated the rift-related evaporite deposits of the northern and southern GOM. This integrated approach combining 2D seismic, gravity, and magnetic data sets results in an improved delineation of these deep crustal features.

1.2.2 Summary of Chapter 3

Mesozoic continental rifting and oceanic spreading between North America and Yucatan block has formed the present-day Gulf of Mexico (GOM) basin. Despite several decades of research, the timing and directions of GOM basin opening remain elusive. For Chapter 3, I integrated three 2D seismic reflection grids that cover an area of 745,000 km^2, 178 seismic refraction data, and 45 wells in a 3D gravity model and derived crustal thickness for the GOM and its peripheral regions. Four crustal domains were delineated according to the crustal thickness that varies from 6-51 km. I restored rifted conjugate margins to its pre-rift locations and performed full-fit reconstruction using the restored continent-ocean boundary locations near a pole located in Africa. Two different motions of the Yucatan block were tested: 1) the Yucatan block continues being rotated clockwise and to the northeast until ~200 Ma and prior to the formation of oceanic crust at 160 Ma; 2) the Yucatan block translates to the northwest prior to the formation of oceanic crust at 160Ma.

My result supports the latter interpretation by showing that the northwestward translation of the Yucatan block at ~200 Ma produces less overlap (49 km^2) with the continental area of the northern South American plate. My result supports the presence of the magmatic underplating in the northeastern GOM as underplating reduced the overall misfit between the restored continent-ocean boundaries by 39 km.

1.2.3 Summary of Chapter 4

The deep-water area of the central Gulf of Mexico (GOM) remains less understood than the shallow-water margins of the GOM because the deep-water area has far fewer wells and seismic reflection surveys than the shallow-water margins. My study uses 12 2D pre-stack, depth

migrated (PSDM) seismic profiles from the conjugate margins of the northeastern GOM and northern Yucatan margin to interpret the GOM marginal rift system, a continuous, 378-km-long rift that bounds both conjugate margins of the late Jurassic, oceanic crust of the deep central GOM.

2D gravity models were built alone two regional profiles in the northern Yucatan margin. The modeled density of 2.6 g/cc reflects the marginal rift fill consists of volcaniclastic rocks and is consistent with the density for this unit obtained by gravity modeling in Chapter 2. Analysis of seismic, gravity, and magnetic data shows that the crust underlying the marginal rift is thinned continental crust, and that tectonic origin of the circum-GOM marginal rift system is the result of extension and necking of the continental crust. The sequential restoration of a regional dip transect suggests the salt present in the distal Yucatan margin was deposited within a topographic low that formed during the late Jurassic (170-163 Ma) and formed the major depocenter for both sedimentary rocks and salt that is up to 7 km in thickness. I provide analogs for similar marginal rift systems from the rifted margins of the South China Sea, Brazil, and the North Sea.

1.2.4 Summary of Chapter 5

Full-Tensor Gravity Gradient (FTG) data are the XYZ rates of change of the Earth's gravitational vector field and reveal subtle density variations in the subsurface. FTG data is similar to vertical gravity data but is far more sensitive to subtle density variations in the subsurface because FTG data consists of the measured directional gradient components of the gravity field. The northwestern to north-central areas of the Gulf of Mexico basin are underlain by thick, shallow layers of salt that obscure seismic data imaging of deeper sedimentary layers. I used high-resolution FTG data to model and map the allochthonous salt canopy in a 19,100 km^2 area of the northern Gulf of Mexico basin.

The base of the remobilized, late Jurassic salt canopy was inverted into a 3D model using the vertical gradient component of the FTG data and satellite-derived gravity data. Minima/maxima of horizontal FTG components are located over near-vertical boundaries formed by density contrasts and provide directional guidance to the source body of the salt canopy and allow its geometry to be mapped. The inverted base of salt from FTG data is consistent with the base of salt interpreted from 2D seismic reflection data - except for the northeastern part of the study area where the inverted base salt is deeper.

The following chapter is: Liu, M., Filina, I., and Mann, P., 2019. Crustal structure of Mesozoic rifting in the northeastern Gulf of Mexico from integration of seismic and potential fields data. Interpretation, vol. 7, No. 4., T857-T867.

CHAPTER 2: CRUSTAL STRUCTURE OF MESOZOIC RIFTING IN THE NORTHEASTERN GULF OF MEXICO FROM INTEGRATION OF SEISMIC AND POTENTIAL FIELDS DATA

2.1 Introduction

Since the publication of high-resolution satellite gravity images of the Gulf of Mexico basin (GOM) by Sandwell et al. (2014), most workers now accept that the GOM opened during a first phase from the late Triassic to middle Jurassic and a second phase from the late Jurassic to earliest Cretaceous (Hudec et al., 2013; Eddy et al., 2014; Nguyen and Mann, 2016). The late Triassic-middle Jurassic (210-163 Ma) Phase 1 presalt rifting was recorded by a broad zone of northeast-trending rifts in the northeastern GOM that reflected northwest to southeast continental extension between the North and South American continents and the intervening, continental Yucatan block (Figure 2.1) (Buffler and Sawyer, 1985; Hudec et al., 2013; Snedden et al., 2014; Steier and Mann, 2019). The aftermath of Phase 1 rifting included the formation of a large unfaulted sag basin where the Louann-Campeche salt of Callovian age (163-161 Ma) was deposited (Hudec et al., 2013; Snedden et al., 2014). Salt deposits thicken over individual sags either as a result of increasing accommodation and enhanced deposition related to thermal subsidence of the underlying rift and/or from post-depositional, downslope movement along mobile salt rollers (Steier and Mann, 2019). This extensive salt basin formed a broad (200-688 km) and thick (6 km) basin in the western GOM but thinned to zero along a narrow (68 km wide) seam in the eastern GOM (Steier and Mann, 2019) (Figure 2.1). This eastward-thinning pattern of the extensive evaporite deposit has led previous workers to propose that oceanic spreading propagated across the incipient central GOM from west to east (Marton and Buffler, 1994) and that influx salt water from the Pacific Ocean into

the western GOM provided the source for thicker and more extensive salt deposits in the western GOM (Steier and Mann, 2019).

Figure 2.1 Tectonic map of the eastern GOM showing the location of the two megaregional seismic lines in heavy black lines relative to the locations of (1) Late Triassic-Early Jurassic Phase 1 rifts, (2) Callovian salt deposits (Steier and Mann, 2019), (3) Late Jurassic Phase 2 rifts, and (4) Late Jurassic-earliest Cretaceous spreading ridges and its flanking area of oceanic crust in the deep central GOM (Lin, 2018) in the northeastern GOM. The light-green polygon shows the SSDR province mapped by Eddy et al. (2014). The dashed purple line shows the outline of the Apalachicola Basin (AB) from the mapping of a seismic reflection grid by Dobson and Buffler (1997). Salt diapirs from Huffman et al. (2004) and Steier and Mann (2019) are shown as pink polygons. The yellow dotted line shows the up-dip limit of Louann salt compiled from Rowan (2014) and Steier and Mann (2019).

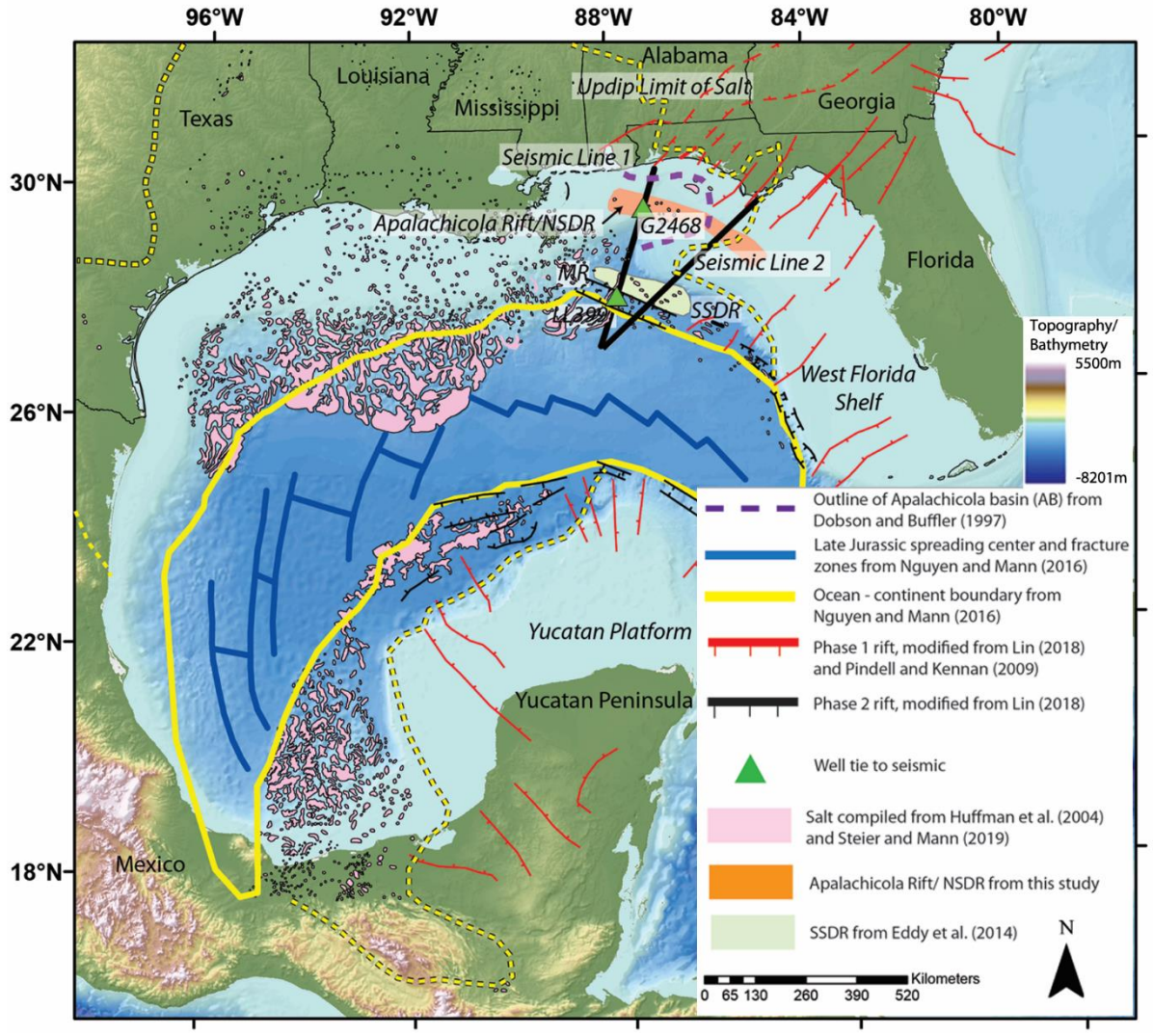

Rift phase 2 of late Jurassic age (161-153 Ma) – was recorded by a more localized and crosscutting pattern of "marginal rifts" or "outer troughs" that immediately preceded the formation of late Jurassic-earliest Cretaceous (154-137 Ma) oceanic crust in the central deepwater GOM (Hudec et al., 2013; Snedden et al., 2014; Lin et al., 2019) (Figure 2.1). These Phase 2 marginal rifts are immediately adjacent to and sub-parallel with the continent-ocean boundary (COB) along the Yucatan-Florida conjugate margins (Escalona and Yang, 2013; Steier and Mann, 2019; Lin et al., 2019) as well as the northwestern GOM-Campeche conjugate margins (Hudec and Norton, 2019). This crescent-shaped area of central GOM oceanic crust with its complex pattern of short spreading ridges offset by fracture zones (Figure 2.1) had been previously mapped from regional seismic refraction surveys, potential field studies, and deeply-penetrating seismic profiles (Buffler and Sawyer, 1985; Marton and Buffler, 1999; Bird et al., 2005; Pindell and Kennan, 2009; Pindell et al., 2016).

The formation of the late Jurassic-earliest Cretaceous oceanic crust split the single pre-oceanic salt basin into two widely separated salt areas: the Louann salt in the US GOM and the Campeche salt in the Mexico GOM (Pindell and Kennan, 2009; Hudec et al., 2013; Pindell et al., 2016; Steier and Mann, 2019) (Figure 2.1). Snedden et al. (2014) and Lin et al. (2019) documented late Jurassic-recent sedimentary infilling of the area of oceanic crust and used the age of downlap to infer the timing of formation of oceanic crust from earliest late Jurassic (154 Ma) to the earliest Cretaceous (137 Ma) along a slow (2.2-2.4 cm/yr) spreading ridge (Figure 2.1) (Hudec et al., 2013; Snedden et al., 2014).

One area of continuing controversy for the GOM opening history that also forms the main objective of this paper is the geologic record of Phase 1 rifting and associated magmatic activity

that is deeply buried beneath the thick, Cretaceous-Cenozoic sedimentary rocks of the northeastern GOM (Figure 2.1). Because Phase 1 structures in this area are older, more deeply buried to depths around 10 km, and locally mantled by a 2-5 km thick salt layer, seismic reflection data are more challenging to interpret and needs careful integration with gravity and magnetic observations and models.

Previous workers such as MacRae and Watkins (1995) and Dobson and Buffler (1997) used industry seismic grids to propose that thick, layered units seen on seismic lines in the northeastern GOM are coarse conglomerate and sandstone that are equivalent to the coarse-grained clastic rocks of the Eagle Mills Formation described from the subsurface of the northern GOM (Warwick, 2017). These workers also proposed that these units were uniformly tilted southwards in the direction of oceanic crust in the central GOM because of their Mesozoic deposition and rotation in Phase 1 half-grabens. In contrast, more recent studies - including Imbert (2005), Imbert and Philippe (2005), Eddy et al. (2014), Van Avendonk et al. (2015), Pascoe et al. (2016), and Curry et al. (2018) - all proposed that these reflectors represented "seaward-dipping reflectors (SDR)"- or layered volcanic flows - that accompanied the Phase 1 rifting event prior to late Jurassic salt deposition (163-161 Ma).

Eddy et al. (2014) used 2D industry seismic lines to identify two zones of SDR's: 1) a southern zone adjacent to the COB that was previously described by MacRae and Watkins (1995) and Dobson and Buffler (1997); and 2) a northern zone that corresponds to the Apalachicola rift (AR) ~180 km north of the oceanic COB (Figure 2.1). Eddy et al. (2014) suggested that: 1) the northern zone may be part of an "inner wedge" system of syn-rift basins that were filled with both basalts and volcaniclastic sedimentary rocks during continental extension; and 2) that the southern

zone was an “outer wedge” overlying more thinned and distal continental crust as described by Planke et al. (2000) from other rifted continental margins.

This study combines the following geophysical and geologic datasets to better understand the rifted crustal structure in this area: 1) two regional seismic profiles (lines DeepEast 533 and DeepEast 1547) ranging in length up to ~370 km that were kindly provided to us by Spectrum Geo (Figure 2.1); 2) published satellite gravity data (Sandwell et al., 2014); 3) published magnetic data (Bankey et al., 2002; Meyer et al., 2017); and 4) public well data (Buffler et al., 1984; Hilterman, 1998; BOEM, https://www.boem.gov).

All of these datasets were used to constrain two integrated geophysical models that improve the locations of the COB, the Apalachicola and marginal rifts, and both magmatic zones. The spatial analysis of gravity and magnetic fields was performed to improve the interpretation of tectonic structures.

2.2 Data and methods

2.2.1 Seismic data

In 2010, investigators of the Gulf of Mexico Basin Opening Project (GUMBO) used seismic refraction transects to study the lithological composition and structural evolution of the GOM (Duncan, 2013; Christeson et al., 2014; Eddy et al., 2014). Ocean Bottom Seismometers (OBS) and an air-gun seismic source were employed to collect seismic refraction data along four dip profiles of the US northern GOM. The OBS spacing for transects in the northeastern GOM is 12 km with a time sampling interval of 5 ms and a shot spacing of 150 m (Duncan, 2013).

GUMBO line 3 (Model 1 in Figure 2.1; Figure 2.2A) extends from offshore Florida, across De Soto Canyon, to the deep central GOM. Figure 2.2A shows the interpretation of three major

subsurface layers from seismic refraction data based on velocity structure. Eddy et al. (2014) interpreted the COB to be located at 290 km along the profile. The first 330 km of this profile was used to study the architecture of the rifted continental margin. Two zones of relatively fast seismic velocity were imaged within the lower crustal layer and can be interpreted as underplating in the lower crust. These zones correlate with high-amplitude anomalies in the observed magnetic field, as noted by Eddy et al. (2014).

Figure 2.2 (a) Cross-section modified from seismic refraction experiment along GUMBO line 3 (Eddy et al., 2014). This GUMBO profile was used to constrain the crustal layers of the integrated geophysical model 1 that is shown in Figure 2.3a. NSDR, northern SDR; AR, Apalachicola rift. (b) Seismic reflection profile 1 is from the Spectrum DeepEast 533 seismic reflection line and was used to constrain the sedimentary layers and the basement of model 1 as shown in Figure 2.3a. (c) Seismic reflection profile 2 is from the Spectrum DeepEast 1547 seismic reflection line and was used to build model 2 as shown in Figure 2.3b. The boxed areas on seismic lines shown in (b and c) are magnifications of both lines in Figure 2.5d and 2.5f, respectively, in the area of the AR basin.

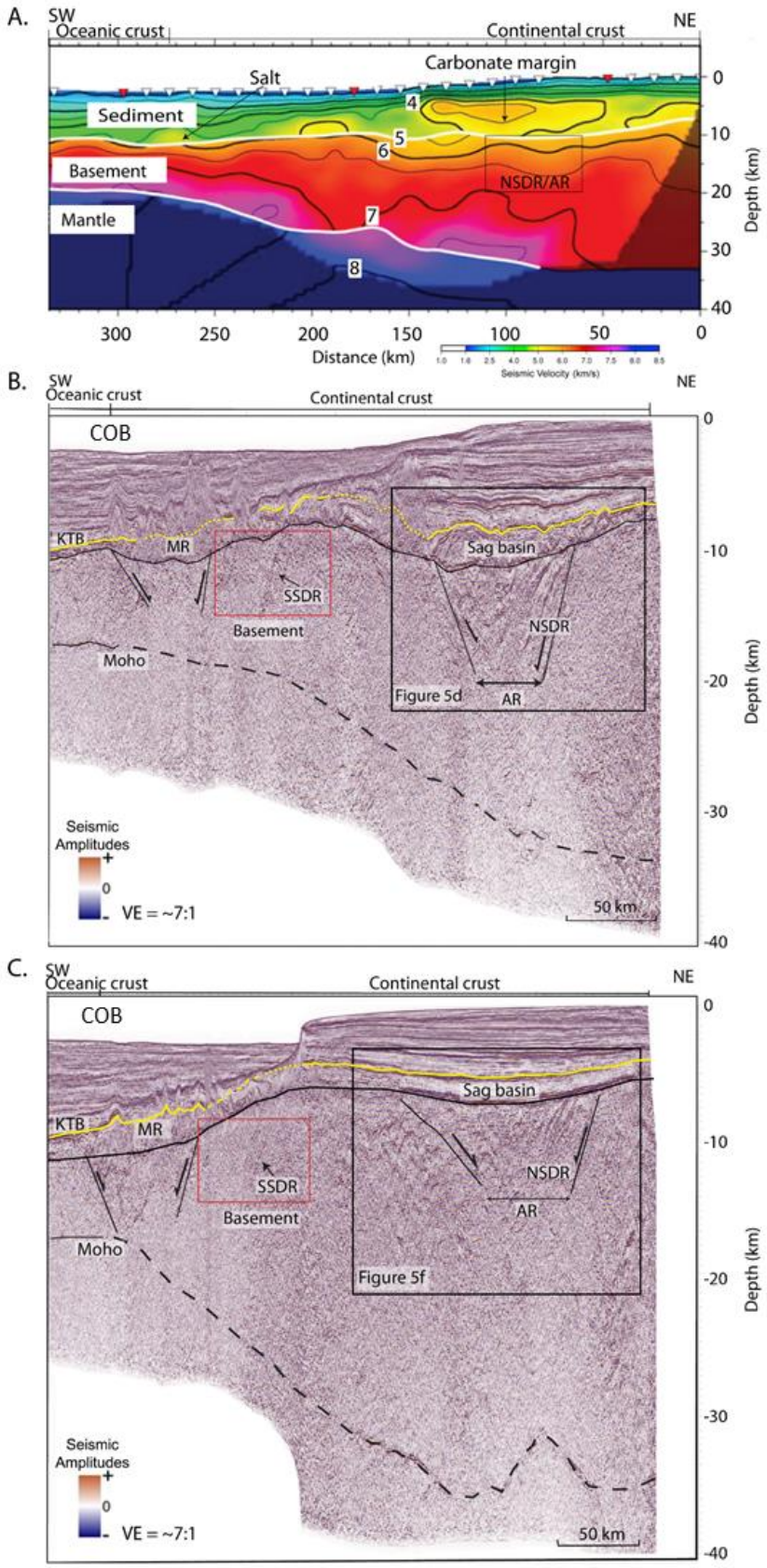
A.
SW
Oceanic crust
Continental crust
NE
Carbonate margin
Salt
Sediment
Basement
Mantle
NSDR/AR
4
5
6
7
8
0
10
20
30
40
Depth (km)
300
250
200
150
100
50
0
Distance (km)
Seismic Velocity (km/s)
B.
SW
Oceanic crust
Continental crust
NE
COB
KTB
MR
SSDR
Basement
Moho
Sag basin
NSDR
AR
Figure 5d
Seismic Amplitudes
+
0
-
VE = ~7:1
50 km
0
-10
-20
-30
-40
Depth (km)
C.
SW
Oceanic crust
Continental crust
NE
COB
KTB
MR
SSDR
Basement
Moho
Sag basin
NSDR
AR
Figure 5f
Seismic Amplitudes
+
0
-
VE = ~7:1
50 km
0
-10
-20
-30
-40
Depth (km)

Two seismic profiles from Spectrum Geo DeepEast dataset were used to interpret crustal features and to build 2D crustal models using potential fields data. The DeepEast survey was acquired in 2007 with a shot point interval of 37.5 m and a two-way-time record length of 14 seconds. The seismic data were depth migrated.

Figure 2.2B shows the first 330 km of seismic reflection profile DeepEast 533 that is coincident with the GUMBO line 3. Geophysical Model 1 was built along GUMBO line 3 to better constrain the sedimentary section and the upper crust. GUMBO line 3 was used to constrain the crustal thickness and the intrusions within the lower crust (Figure 2.2A). Figure 2.2C shows part of 2D seismic reflection line DeepEast 1547 that was used to constrain the sedimentary section and upper crust of geophysical Model 2.

2.2.2. Integrated geological and geophysical analysis

Free-air satellite gravity field data (Sandwell et al., 2014) and the USGS regional magnetic compilation (Bankey et al., 2002) were used in developing both integrated geophysical models and for mapping the major tectonic structures such as the COB, SDR province(s), and the marginal rift that flanks the area of the late Jurassic oceanic crust underlying the deepwater GOM (Lin et al., 2019). The reported accuracy of the free-air gravity dataset is about two mGal (Sandwell et al., 2014).

Before sampling and modeling, the magnetic dataset was reduced to the pole (RTP) to remove the skewness of magnetic anomalies due to non-verticality of the ambient magnetic field and to make interpretations easier - although there is clear indication whether these anomalies are caused by induced or by remnant magnetization (Bankey et al., 2002. Because most of the USGS magnetic data were collected in 1985 in the northeastern GOM (Bankey et al., 2002, the following

parameters from the magnetic epoch for 1985 were used during the reduction to the pole transformation; inclination of 55.77 degrees, declination of 4.21 degrees, and total intensity of 48785 nT.

The subsurface of the GOM was divided into several layers and physical properties (density and magnetic susceptibility) were assigned to each layer based on well data (sedimentary layers and the upper continental crust) or published values for various types of rocks (lower continental and oceanic crustal units).

Exploration well G2468 (BOEM) located 8 km west of line DeepEast 553 (Figure 2.1) was used to constrain the top of the carbonate platform (91.44 m or 300 ft). With limited basement penetrated wells in the GOM, we used a DSDP well at site 538A (Buffler et al., 1984) in the southeastern GOM to constrain the bulk density of the upper continental crust. The general density-velocity trend from 447 deepwater wells (Hilterman, 1998) was modified from Filina et al. (2015). The potential fields' response was computed for each model and compared with the observed signal. The model was then adjusted to ensure a good match between observed and calculated signals in both gravity and magnetic data and was checked for consistency with seismic, gravity, magnetic, and well log information. All gravity and magnetic modeling were performed using Seequent's Oasis Montaj software.

2.2.3 Spatial analysis

Major geological boundaries are manifested by different polarities, amplitudes, and wavelengths of the potential fields data and are delineated as boundaries by the magnitude of contrast in physical properties, geometry, and the depth of the contact between the juxtaposed rocks. For these reasons, the recorded potential fields represent the combination of all the signals

related to various geological structures in the subsurface. In order to highlight the specific crustal structures, its important to remove other competing signals as a first step.

Bouguer correction was performed on the free-air gravity field by taking into account the gravity effect of water (density of 1.03 g/cc) over the unconsolidated sediments with an assumed density of 2.0 g/cc. The regional trend due to gravity effects of deep structures was removed, including the Moho boundary, by an upward continuation to the elevation of 40 km.

Despite its finer sampling interval of 1 km, the USGS magnetic dataset does not cover the region of offshore Florida (Bankey et al., 2002). Instead, the spatial analysis was performed using the EMAG_V3 dataset (Meyer et al., 2017) from the National Oceanic and Atmospheric Administration (NOAA) with a spatial resolution of 2-arc-minutes (about 3.6 km in the GOM). According to NOAA, some grids and track line data that were collected during the period of 1946 to 2014 have been included in EMAG2_V3. Lacking the detailed information about when the magnetic data in northeastern GOM were collected, the same parameters from the USGS magnetic dataset (Bankey et al., 2002) were used from 1985 to reduce EMAG2_V3 to the pole.

A series of derivative filters (mathematical transformations) were applied to highlight the lineaments in both potential field datasets . The correlations of the observed lineaments with the geological structures determined from the two modeled profiles were used to extend the interpretation to the areas outside of the area of my seismic coverage (Figure 2.4). Information from the analysis of the gravity and magnetic data (Figure 2.4) were used to map the extent of the marginal rift basin, the SDR provinces, and the COB.

2.3 Results

2.3.1 Model 1

Model 1 (Figure 2.3A) comprises seventeen layers each with its own density and magnetic susceptibility. The top ~10 km consists of eight sedimentary layers with their modeled densities that include: Pleistocene (2.25 g/cc), Pliocene (2.35 g/cc), Miocene (2.4 g/cc), Paleogene (2.45 g/cc), Mesozoic (2.55 g/cc), salt (2.15 g/cc), carbonate rocks (2.6 g/cc), and marginal rift sedimentary rocks (2.55 g/cc). The magnetic susceptibility of the sedimentary section was assumed to be 0 SI except for the marginal rift sediments (0.005 SI), which has been proposed by Weil and Yonkee (2009) and Tan et al. (2007) to consist of redbeds. The southern SDR (SSDR in Figure 2.3A) province was assigned the density of 2.85 g/cc and magnetic susceptibility of 0.05 SI. The northern province (NSDR/AR in Figure 2.3A) was assigned the same physical properties as the SSDR.

Figure 2.3 (a) Integrated geophysical model 1 that is coincident with the GUMBO3 refraction line (Figure 2.2a) and the Spectrum DeepEast 533 reflection line (Figure 2.2b). The black lines outline the subsurface layers. The SSDR province is adjacent to the marginal rift basin that filled with the sediments, reactivated salt, whereas the NSDR province is contained within the AR. The dashed white line shows the proposed boundary between sedimentary-filled AR to the southwest and the NSDR to the northeast. The interpreted COB is shown as a blue dotted line. (b) Integrated geophysical model 2 that is constrained by the Spectrum DeepEast 1547 seismic reflection profile. The black lines in the bottom panel outline subsurface layers. The NSDR/AR province is located above an elevated Moho, whereas the SSDR province occurs adjacent to the marginal rift basin. The COB is shown as a blue dotted line.

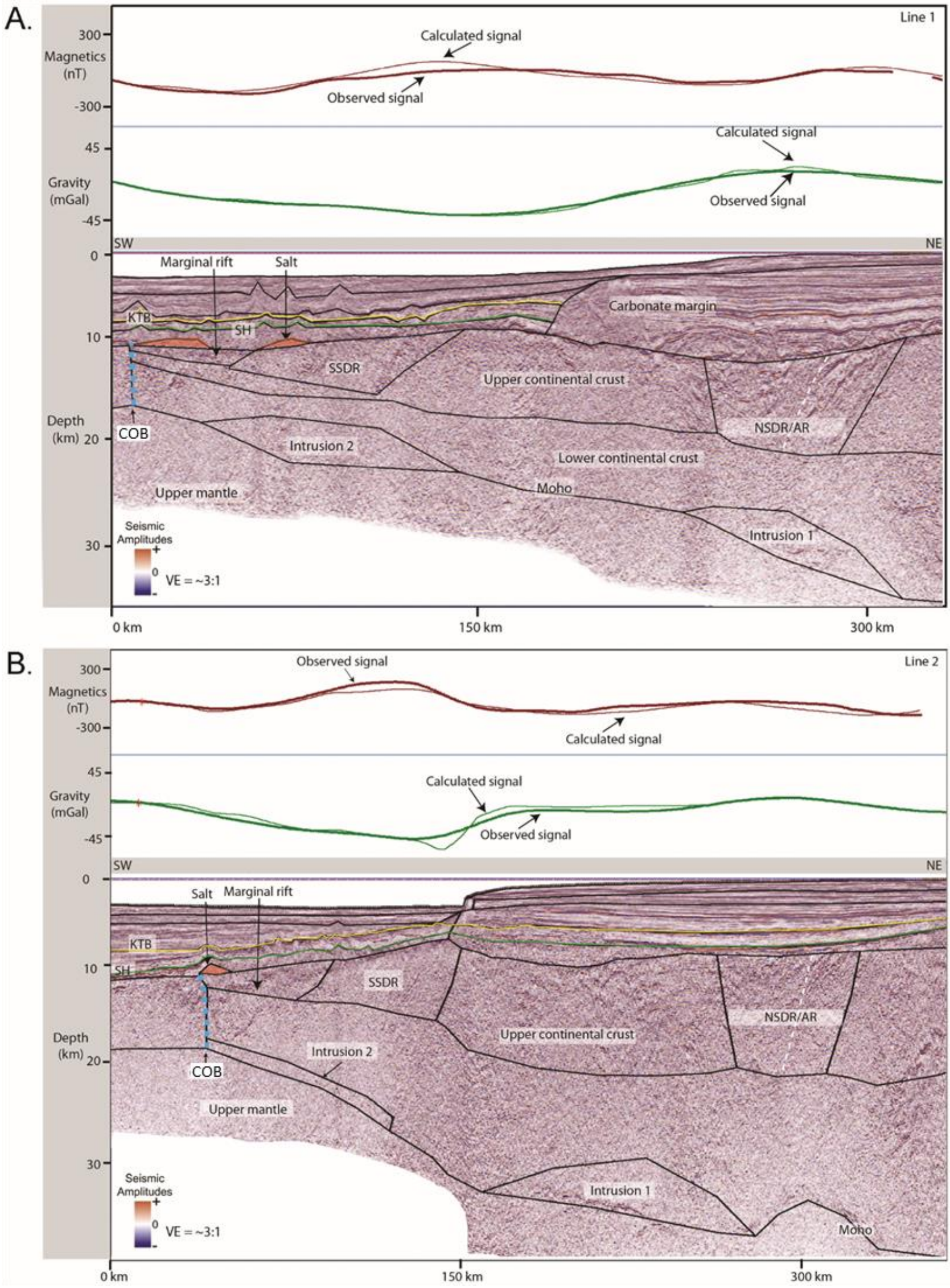
A.
Line 1
300
Magnetics
(nT)
-300
Calculated signal
Observed signal
45
Gravity
(mGal)
-45
Calculated signal
Observed signal
SW
NE
0
Marginal rift
Salt
KTB
SH
Carbonate margin
10
SSDR
Upper continental crust
Depth
(km)
20
COB
Intrusion 2
NSDR/AR
Lower continental crust
Moho
Upper mantle
Seismic
Amplitudes
+
0
-
VE = ~3:1
30
Intrusion 1
0 km
150 km
300 km
B.
Line 2
300
Magnetics
(nT)
-300
Observed signal
Calculated signal
45
Gravity
(mGal)
-45
Calculated signal
Observed signal
SW
NE
0
Salt
Marginal rift
KTB
SH
10
SSDR
NSDR/AR
Depth
(km)
20
Upper continental crust
Intrusion 2
COB
Upper mantle
Seismic
Amplitudes
+
0
-
VE = ~3:1
30
Intrusion 1
Moho
0 km
150 km
300 km

The crust along Model 1 changes from a relatively unstretched continental crust at the northeastern end of the line to a much thinner oceanic crust of the central deepwater GOM at the southwestern end of the line (Figure 2.3A). The bottom layer of the model is the mantle with a density of 3.3 g/cc and magnetic susceptibility of 0 SI. The overall physical properties of the modeled rocks are consistent with similar studies performed by Filina (2018), Filina (2019), and by Filina and Hartford (2018, 2019) in the southern GOM. The only difference between Model 1 and the lines modeled by Filina (2018), and Filina (2019) is the increased magnetic susceptibilities of the crustal rocks in the northeastern GOM with respect to the northwestern and central GOM. This magnetic variation at the scale of the entire GOM is consistent with the west to east increase in magmatism in the GOM (Eddy et al., 2018).

In the northern continental area of Model 1, the crust is composed of two layers – the upper and the lower continental crust units. The thickness of the upper continental crust varies between 6 and 13 km. This layer has a density of 2.78 g/cc as constrained by DSDP well 538A (Buffler et al., 1984) and is assigned a magnetic susceptibility value of 0.04 SI. The NSDR region is constrained within the Apalachicola rift as previously interpreted by Dobson and Buffler (1997) and shown on the Spectrum seismic reflection line in Figure 2.3. The NSDR is 67 km wide and up to 10 km thick (at the model distance of 22-89 km, Figures 2B, 3, and 4).

From seismic reflection data alone it is difficult to distinguish layered infill related to magmatic SDRs within the Apalachicola rift from layered sedimentary infill as previously noted by MacRae and Watkins (1995), who ultimately favored a volcanic origin for the layering. Due to the observed and modeled potential fields, this study proposes a magmatic SDR origin for the

layering as proposed by Imbert (2005), Imbert and Philippe (2005), Eddy et al. (2014), Van Avendonk et al. (2015), Pascoe et al. (2016), and Curry et al. (2018).

For both the SSDR and the Apalachicola rift in the north, the strongest and most planar reflectors dip southward towards the oceanic crust of the deepwater GOM and are located within or along the northern flanks of the rifts (Figure 2.3A). To satisfy gravity and magnetic signals, both regions must be filled with rocks of a higher density of 2.85 g/cc and higher magnetic susceptibility of 0.05 SI than the upper crust. The SSDR province has a lateral extent of 40 km in Figure 2.3A and is 12 km wider than the SDR province interpreted by Eddy et al. (2014) on GUMBO line 3. According to Model 1, this inferred SSDR province is 10 km thick (Figure 2.3A). The marginal rift in the south is 3 km thick, 48 km wide, and bounded by the SSDR in the north and by the COB in the south. The density of the marginal rift section is assumed to be 2.6 g/cc, and magnetic susceptibility is assigned as 0.005 SI.

The lower continental crust was assumed to have a density of 2.92 g/cc (Carlson and Herrick, 1990) with a magnetic susceptibility of 0.06 SI. These parameters were determined during the modeling based on an improved fit between the observed and computed magnetic fields. The derived magnetic susceptibility is generally consistent with the range of 0.025 to 0.086 SI for the rocks of the lower continental crust as proposed by Schnetzler (1985). The ocean crust was assigned a density of 2.85 g/cc and magnetic susceptibility of 0.075 SI for Models 1 and 2.

The interpreted COB is located at a distance of 301 km along Model 1, which is coincident with a prominent magnetic trough (Figure 2.3A). The magnetic signal is very sensitive to the location of the COB in this model. The model also suggests the presence of two anomalous, high-density bodies (intrusions 1 and 2) within the lower continental crust that are located between 46-

119 km and 196-280 km along the length of Model 1. These intrusive bodies were modeled with a density of 2.95 g/cc and magnetic susceptibility of -0.1 SI.

The presence of intrusive bodies was constrained by their magnetic signal. Intrusions 1 and 2 are inversely magnetized and are coincident with the zones of fast seismic velocities (~7.5 km/s) in the lower continental crust that was mapped in the refraction experiment (Figure 2.2A). The inferred intrusive bodies are dense, highly magnetic and characterized by fast Vp value. Similar intrusive bodies were interpreted by Filina (2019) in the northwestern and central GOM, and by Filina and Hartford (2018) in the southern GOM. The dense intrusive structures in the lower crust can explain the presence of a flat Moho because the intrusions of mafic melts can compensate for crustal thinning and a shallow Moho as observed in other rifts (Nielsen and Thybo, 2009).

2.3.2 Model 2

Model 2 was built along the Spectrum seismic reflection profile DeepEast 1547 (Figure 2.2C) and extends from offshore Florida toward the Yucatan margin (see location in Figure 2.1). Model 2 consists of fourteen layers up to a depth of 40 km (Figure 2.3B). Subsurface rocks were assigned the same physical properties as used in Model 1 shown in Figure 2.3A. One autochthonous salt body over the marginal rift deposits was included in the model based on the interpretation of the seismic reflection image (Figure 2.2C).

The COB is located at 336 km along Model 2 and is manifested as a magnetic low similarly to the magnetic low observed along the COB in Model 1 (Figure 2.3B). The continental crust for Model 2 was also modeled with an upper and lower continental crust with the same physical properties as seen in Model 1 (Figure 2.3A). Similar to Model 1, two intrusive bodies were added to the lower continental crust of the Model 2 at distances along the length of the seismic line

between 70-200 km (intrusion 1) and 280-323 km (intrusion 2). These intrusions in the lower crust are required to fit the magnetic profile and are consistent with high-density, magmatic bodies that underlie other continental rifts worldwide as discussed by Nielsen and Thybo (2009).

As no seismic refraction data are available for Model 2, its correlation with higher seismic velocities cannot be established. Both intrusions have negative magnetic polarity and are modeled with a magnetic susceptibility of -0.1 SI, which is the same value with the magnetic susceptibility used for Model 1. Similarly, one SDR province, the Apalachicola rift, and the marginal rift were interpreted from seismic data and were included in Model 2 (Figure 2.3B). The rift to the north occurs between the model distances of 40-103 km, and the SSDR is to the south (216 - 273 km) and occurs adjacent to the marginal rift basin.

2.3.3 Tectonic structures from spatial analysis

This study determined the locations of the COB, the marginal rift basin, and both SDR provinces from the 2D models and correlated them with the lineaments in filtered potential fields that could be traced outside of seismic coverage (Figure 2.4). The tilt derivative transformation of the residual Bouguer gravity map (Figure 2.4A) and the first derivative filter of the residual RTP magnetic field (Figure 2.4D) were used to map the lateral extents of the COB, the marginal rift, and both SDR provinces. In general, the magnetic lineaments appear to be less pronounced than the gravity lineaments and likely reflect the different resolutions of these two datasets. As the anomalies are better highlighted in the filtered gravity field than from magnetic data, the spatial analysis was primarily constrained using the filtered gravity map and then validated with the filtered magnetic field.

Figure 2.4 Continental margin rift structure, northern and southern SDR provinces, and the COB as interpreted from spatial analysis of potential fields and constrained from models 1 and 2. The filtering process is described in the text. (a) Tilt derivative of the residual Bouguer gravity map. (b) Tilt derivative of the residual Bouguer gravity map showing locations of the SSDR and NSDR/AR provinces, COB, and marginal rift basin. (c) First vertical derivative of the RTP magnetic map. (d) First vertical derivative of the RTP magnetic map with interpretations from this study. The purple line marks the boundaries of the NSDR/AR province, whereas the brown line shows the SSDR province. The dashed lines on the two sides of the mapped structures indicate the uncertainty of the spatial interpretation. The marginal rift basin is outlined by a dark blue line, and the COB is shown in green. The black dotted line shows the updip limit of the Louann salt from Rowan (2014) and Steier and Mann (2019). The dashed white line shows the eastern boundary of the AB from Dobson and Buffler (1997).

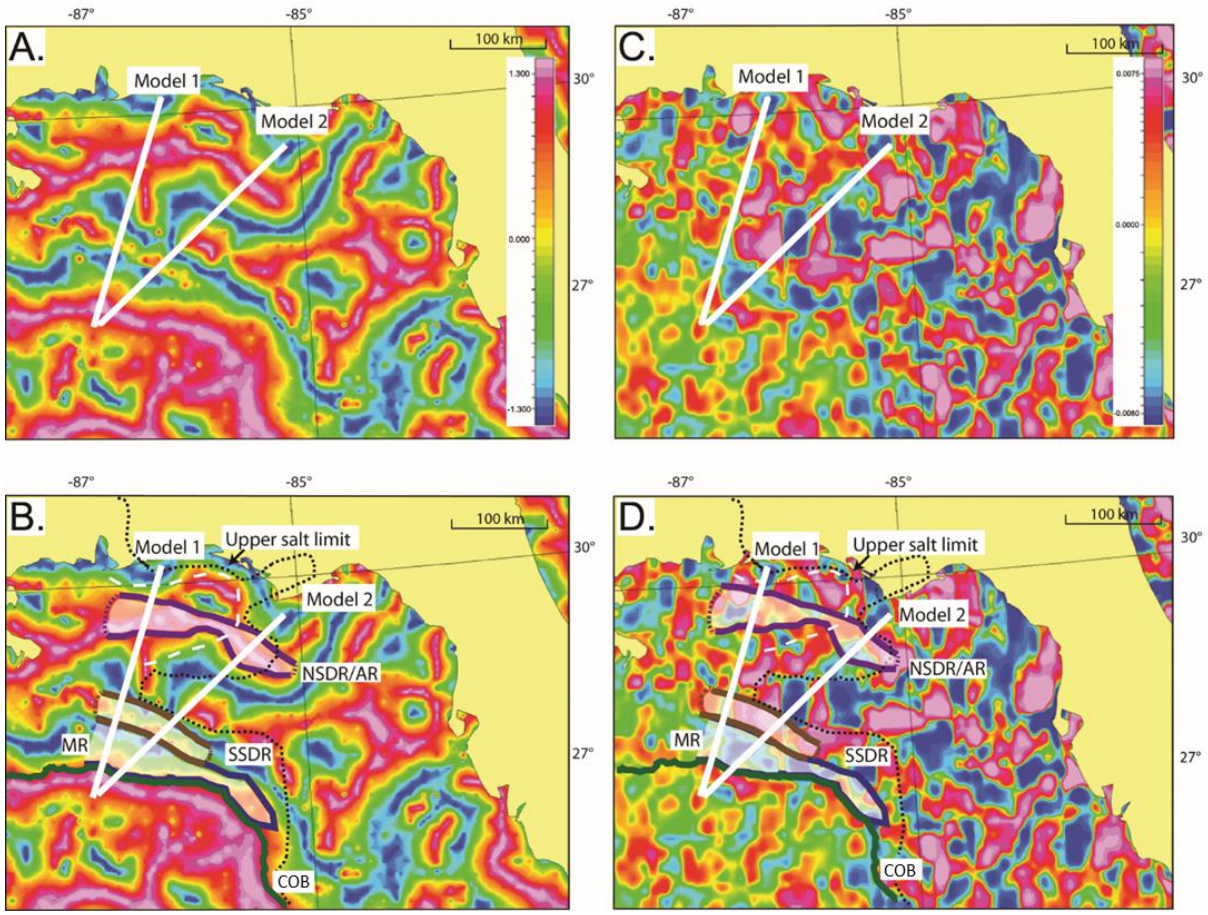
A.
-87°
-85°
100 km
30°
27°
Model 1
Model 2
1.300
0.000
-1.300
C.
-87°
-85°
100 km
30°
27°
Model 1
Model 2
0.0075
0.0000
-0.0080
B.
-87°
-85°
100 km
30°
27°
Model 1
Upper salt limit
Model 2
NSDR/AR
MR
SSDR
COB
D.
-87°
-85°
100 km
30°
27°
Model 1
Upper salt limit
Model 2
NSDR/AR
MR
SSDR
COB

The locations of the COB from the two models, i.e., 301 km along Model 1 (GUMBO3) and 336 km along Model 2, were shown on the filtered potential fields as black ticks (Figure 2.4B and 4D). These COB locations correspond to the same gradient in the filtered gravity, which is the edge of a pronounced high. On magnetic data, the COB locations are marked by a linear magnetic low. These correlations were used to trace the COB for the entire study area as shown in Figure 2.4. Both the SSDR province and NSDR/AR correspond to gravity and magnetic highs, while the marginal rift basin is expressed by gravity and magnetic lows.

The modeled result suggests that the width of the marginal rift basin decreases from 48 km to 28 km on Models 1 and 2, respectively. The thickness of the sedimentary fill in the marginal rift basin is 3 km in both models. According to the spatial analysis, the marginal rift sedimentary basin wedges out to the east of the Model 2 and is bounded by the SSDR province in the north and by the COB in the south (Figure 2.4B and 4D). The Apalachicola rift has an average width of 65 km and an average thickness of 10 km, while the SSDR province is 48 km wide and 7 km thick (Figure 2.4).

2.4 Discussion

As a result of the integrated modeling, this study has derived physical properties (density and magnetic susceptibility) of the subsurface rocks that are consistent for both models (Figure 2.3A and 3B). These physical properties are either constrained by well data (sedimentary layers and upper continental crust) or with published values from previous gravity and magnetic models for the GOM (Filina et al., 2015). The modeled intrusive bodies share the same value of magnetic susceptibility, and their magnetic polarity pattern is also consistent between both models. The

locations of the intrusions 1 and 2 on Model 1 correspond to the fast Vp zone in the refraction experiment results described by Eddy et al. (2014) (Figure 2.2A) and Van Avendonk et al. (2015).

The derived COB locations for Models 1 (Figure 2.3A) and 2 (Figure 2.3B) are constrained from both potential field datasets, although the magnetic field appears to be more sensitive than the gravity field for better defining the COB location. The 3-km-thick marginal rift section interpreted in Model 1 from seismic reflection data (Figure 2.2B) is also consistent with the observed magnetic profile. The marginal rift section thins to the southwest in both models and likely reflects the extreme thinning of the underlying, continental crust in the direction of the adjacent oceanic crust (Figure 2.3A, B). The NSDR and SSDR provinces require denser and more magnetic rocks with respect to the upper continental crust in order to explain observed gravity and magnetic signals (Figure 2.4A and 4B). The NSDR province appears to be wider (65 km) and longer (285 km) than the SSDR (48 km wide and 235km long). The SSDR province is about 22 km wider and 63 km longer than the same province as determined by Eddy et al. (2014) (Figure 2.1, 26 km wide and 172 km long). The northwestern edge of the SDR province from Eddy et al. (2014) appears to be limited than what was proposed in this study based on the potential field data (Figure 2.1). Using the DeepEast seismic reflection dataset, the SDR was extended to the northwest beyond the original SDR area mapped by Eddy et al. (2014).

This study supports previous workers that the layered units associated with the Apalachicola rift in the north and adjacent to the marginal rift in the south are SDRs of magmatic origin. These previous SDR studies include Imbert (2005), Imbert and Philippe (2005), Eddy et al. (2014), van Avendonk et al. (2015), Pascoe et al. (2016), and Curry et al. (Curry et al., 2018).

A magmatic origin for the SDRs is consistent with the observed and modeled higher densities and magnetic susceptibilities in both these areas (Figures 3A and 3B) and the uniform seaward dip of the reflectors in both areas. It is clear that the northern area of SDRs was erupted into the Apalachicola rift (Figure 2.4), and the southern area of SDRs erupted adjacent to the marginal rift about 162 Ma (Eddy et al., 2014). The top of the NSDR unit is truncated by the sag basin overlying the Apalachicola rift (Figure 2.5D and 5F).

Figure 2.5 (a) Uninterpreted depth-migrated seismic reflection data of the marginal rift on line 1. (b) Seismic interpretation for the juxtaposition of the marginal rift and SSDR. The age control is from well LL399 (Figure 2.1). KTB, Navarro-Taylor Formations (66–123 Ma); SH, Sligo-Hosston Formations (123–138 Ma); CVB, Cotton Valley-Bossier Formations (138–142 Ma); and HVB, Top Haynesville-Buckner Formations (152 Ma) are the horizons interpreted in this study based on ties shown in Snedden et al. (2013) and Lin et al. (2019). (c) Uninterpreted depth migrated seismic reflection data of the AR and its overlying sag basin. (d) Seismic interpretation of the infill and bounding normal faults of the 10 km thick AR. The red polygon shows the 10 km thick, volcanic flows along the northeastern edge of the rift. (e) Uninterpreted depth-migrated seismic reflection section of the Spectrum DeepEast 1547. (f) Interpretation of the 8 km thick, eastern AR with a 7 km thick NSDR shown in the red. Previous workers have noted that the AR thins and eventually disappears in an eastward direction.

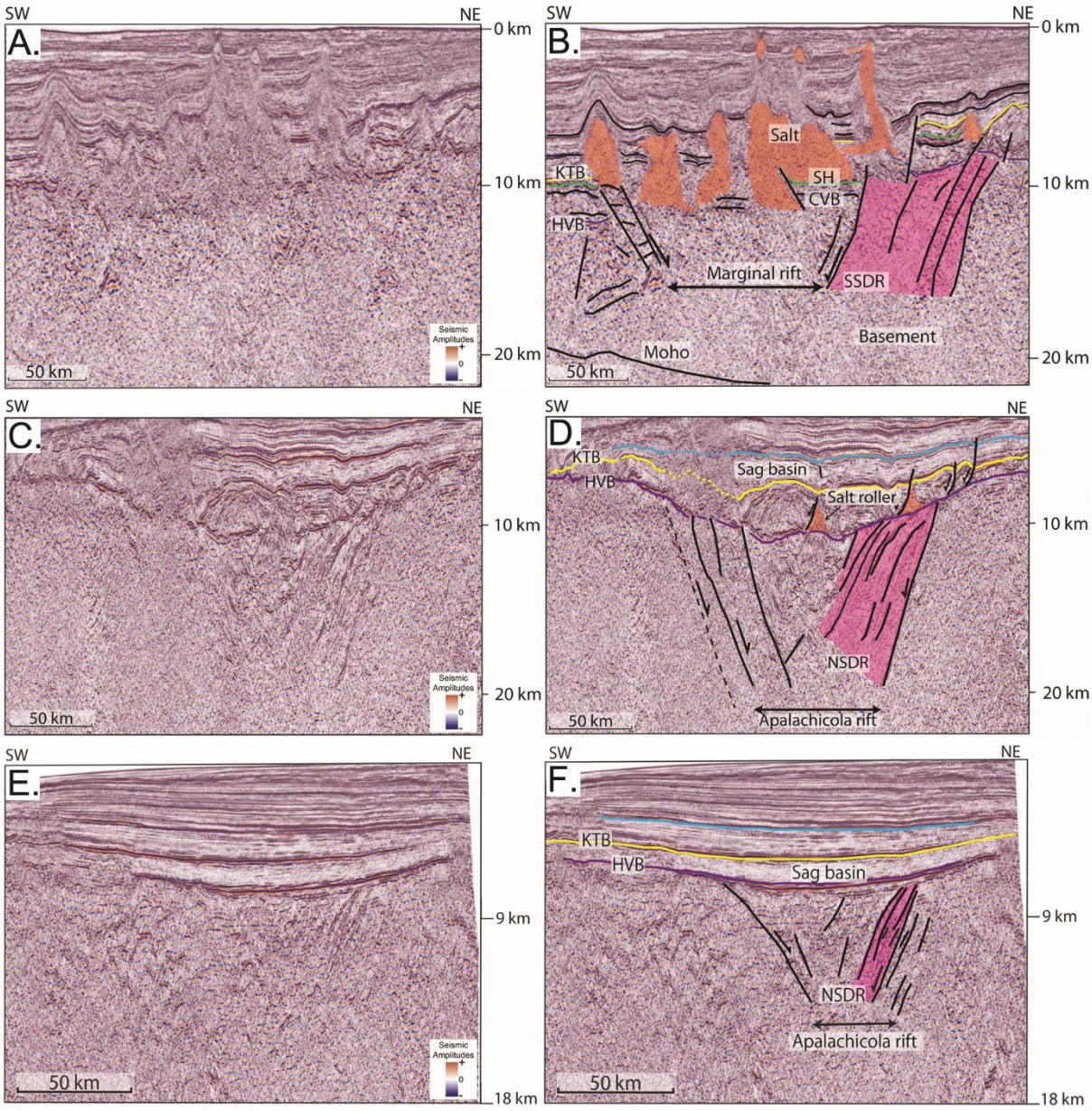
SW
NE
A.
0 km
10 km
20 km
Seismic Amplitudes
+
0
-
50 km
B.
Salt
KTB
SH
CVB
HVB
Marginal rift
SSDR
Basement
Moho
C.
D.
Sag basin
Salt roller
NSDR
Apalachicola rift
E.
9 km
18 km
F.

The dip of these volcanic rocks was likely controlled by the topographic depression of the rift valley and eruption along bounding normal faults which in the case appear to be along the northern edge of the rift (Figure 2.5D and 5F). A Precambrian analog for voluminous volcanic rocks infilling the Apalachicola rift is the Midcontinent rift beneath Lake Superior where 8 km of volcanics and interbedded sedimentary rocks (velocity of 5.0-6.5 km/s) infilled the central axis of the rift (Behrend et al., 1988; Shay and Tréhu, 1993). A well developed, symmetrical sag basin up to 1-3 km in thickness overlies the Apalachicola rift. Vertical relief of the sag promoted the downslope motion of salt rollers (Figure 2.5D).

In contrast to the NSDR volcanics confined to the Apalachicola rift, the SSDR province appears to have formed in an unconfined continental margin setting (Figure 2.5B) as observed on coeval Mesozoic Atlantic rifted margins (Eldholm et al., 1995; Tian and Buck, 2019). The SSDR in the northern GOM sits at a structurally higher level relative to the adjacent marginal rift and appears to have formed prior to the Phase 2 marginal rift adjacent to oceanic crust beneath the central GOM (Figure 2.5B).

The west-to-northwest orientation of the marginal rift and parallelism with the COB is consistent with its formation during the late Jurassic Phase 2 rifting during rotation of the Yucatan block and immediately preceded the formation of late Jurassic oceanic crust (Steier and Mann, 2019; Lin et al., 2019) (Figure 2.1). The parallel, west-northwest orientation and shape of the Apalachicola rift and its overlying sag basin indicate that it likely propagated in an eastward direction (Figure 2.5D and 5F). Salt thickens in the sag basin overlying the wider western end of the rift (Figure 2.5D) but thins and disappears in the thinner sag overlying the narrower eastern end of the basin (Figure 2.5F). The unusual, west-northwest trend of the Apalachicola rift in

comparison with more northeasterly Phase 1 rifts may indicate that the Apalachicola rift may have formed as a transitional rift between the northeast-striking Phase 1 rifts and the marginal rifts that formed adjacent to the initial, late Jurassic oceanic crust (Lin et al., 2019).

2.5 Conclusions

This study developed two integrated geophysical models in the northeastern GOM based on combined analysis of seismic, gravity, magnetics, and well data. The seismic data and gravity and magnetic modeling constrain a 3 km thick sedimentary fill in the marginal rift that includes reactivated and highly-deformed salt deposits that are thicker in the marginal rift than in adjacent areas (Figure 2.2B, 2C, 3A, and 3B). Gravity and magnetic modeling show that the marginal rift basin is 42 km wide along seismic line 1, narrows to a width of 28 km along seismic line 2, and disappears to the east. The marginal rift from this study is similar in dimensions and thickness to those described along the Yucatan-Florida conjugate margin (Steier and Mann, 2019) and the northwestern GOM-Campeche conjugate margin (Hudec and Norton, 2019) (Figure 2.1).

The marginal rift in the study area is bounded by the 48 km wide SSDR magmatic province of southward-dipping reflectors along its northern flank and by the down-to-the-north "step-up fault" bounding the COB along its southern flank (Figure 2.4B and 4D). The SSDR magmatic province is estimated to be 48 km wide and 235 km long.

A 65 km wide and 285 km long province of dense and highly magnetic rocks similar to SSDR that is entirely contained within the Apalachicola rift is well defined on both seismic reflection lines (Figure 2.2B and 2C). Based on the potential fields modeling, this study supports the interpretation that the high density (2850 kg/m^3), 7-10 km thick, layered sections are of magmatic origin as proposed by Imbert (2005), Imbert and Philippe (2005), Eddy et al. (2014),

Van Avendonk et al. (2015), Pascoe et al. (2016), and Curry et al. (2018). These rocks exhibit densities and magnetic susceptibilities that are consistent with rocks of magmatic origin. This is not a typical SDR as the unit is confined within a rift basin setting (Figure 2.5D and 5F).

This study proposes that the Apalachicola rift may have propagated eastward as it becomes narrower and exhibits a smaller overlying sag basin in the eastern area (Figure 2.5F). The anomalous east to the southeast trend of the Apalachicola rift contrasts with other Triassic-Early Jurassic rifts and may indicate that the Apalachicola rift may have formed as a transitional rift between the northeast-trending Phase 1 rifts and the more east-west Phase 2 marginal rift adjacent to oceanic crust (Figure 2.1). The integration of multiple geophysical datasets resulted in much better constrained crustal structures than derived from 2D seismic alone.

2.6 Bibliography

Bankey, V., Cuevas, A., Daniels, D., Finn, C. A., Hernandez, I., Hill, P., Kucks, R., Miles, W., Pilkington, M., Roberts, C., Roest, W., Rystrom, V., Shearer, S., Snyder, S., Sweeney, R., Velez, J., Phillips, J. D., Ravat, D., 2002. Digital data grids for the magnetic anomaly map of North America: open-file report 02-414.

Behrend, J. C., Green, A. G., Cannon, W. F., Hutchinson, D. R., Lee, M. W., Milkereit, B., Agena, W. F., Spencer, C., 1988. Crustal structure of the Midcontinent rift system: results from GLIMPCE deep seismic reflection profiles: Geology, 16, 81–85.

Bird, D. E., Burke, K., Hall, S. A., Casey, J. F., 2005. Gulf of Mexico tectonic history: h otspot tracks, crustal boundaries, and early salt distribution: AAPG Bulletin, 89, 311–328.

Buffler, R. T., Sawyer, D. S. 1985. Distribution of crust and early history, Gulf of Mexico Basin: Gulf Coast Association of Geological Societies Transactions, 35, 333–344.

Buffler, R. T., Schlager, W., Bowdler, J. L., Cotillon, P. H., Halley, R. B., Kinoshita, H., Magoon III, L. B., Mcnulty, C. L., Patton, J. W., Pisciotto, K. A., Silva, I. P., Suarez, O. A., Testarmata, M. M., Tyson, R. V., Watkins, D. K., 1984. Site 538: Deep Sea Drilling Project, 77, 279–336.

Carlson, R. L., Herrick, C. N., 1990. Densities and porosities in the oceanic crust and their variations with depth and age: Journal of Geophysical Research: Solid Earth, 95, 9153–9170.

Christeson, G. L., Van Avendonk, H. J. A., Norton, I. O., Snedden, J. W., Eddy, D. R., Karner, G. D., Johnson, C. A., 2014. Deep crustal structure in the eastern Gulf of Mexico: Journal of Geophysical Research: Solid Earth, 119, 6782–6801.

Curry, M. A. E., Peel, F. J., Hudec, M. R., Norton, I. O., 2018. Extensional models for the development of passive margin salt basins, with application to the Gulf of Mexico: Basin Research, 30, 1180–1199.

Dobson, L. M., Buffler, R. T., 1997. Seismic stratigraphy and geologic history of Jurassic rocks, northeastern Gulf of Mexico: AAPG Bulletin, 81, 100–120.

Duncan, M. H., 2013. The northeastern Gulf of Mexico: volcanic or passive margin? Seismic implications of the Gulf of Mexico basin opening project: Unpublished M.S. thesis, University of Texas at Austin, 90 p.

Eddy, D. R., Van Avendonk, H. J. A., Christeson, G. L., Norton, I.O., 2018. Structure and origin of the rifted margin of the northern Gulf of Mexico: Geosphere, 14, 1804–1817.

Eddy, D. R., Van Avendonk, H. J. A., Christeson, G. L., Norton, I. O., Karner, G. D., Johnson, C. A., Snedden, J. W., 2014. Deep crustal structure of the northeastern Gulf of Mexico: Implications for rift evolution and seafloor spreading: Journal of Geophysical Research: Solid Earth, 119, 6802–6822.

Eldholm,O., Skogseid, J., Planke, S., Gladczenko, T. P., 1995. Volcanic margin concepts, in E. Banda, M. Torné, and M. Talwani, eds., Rifted ocean-continent boundaries: Springer, Dordrecht, 1–16.

Escalona, A., Yang, W., 2013. Subsidence controls on foreland basin development of northwestern offshore Cuba, southeastern Gulf of Mexico: AAPG Bulletin, 97, 1–25.

Filina, I., 2018. Integration with non-seismic methods: An example from the Northern Gulf of Mexico: AAPG Datapages/Search and Discovery Article 2856122.

Filina, I., Delebo, N., Mohapatra, G., Coble, C., Harris, G., Layman, J., Strickler, M., Blangy, J.-P., 2015. Integration of seismic and gravity data — A case study from the western Gulf of Mexico: Interpretation, 3, no. 4, SAC99–SAC106.

Filina, I., 2019. Crustal architecture of the northwestern and central Gulf of Mexico from integrated geophysical analysis: Interpretation, 1–61.

Filina, I., Hartford, L., 2018. Subsurface structures along the western Yucatan from integrative geophysical analysis: AGU Fall Meeting.

Filina, I., Hartford, L., 2019. Integrated analysis of seismic data and potential fields in Southeastern Gulf of Mexico with implications to pre-salt sediments and crustal architecture: AAPG Annual Convention, Program with Abstracts.

Gulf Oil Corporation, 1975, Scanned well report of Gulf of Mexico well OCSG02468, https://www.boem.gov, accessed 16 April 2018.

Hilterman, F., 1998. Rock property framework for comprehending deep-water seismic response: Presented at the 14th Annual SEG Gulf Coast Technical Meeting.

Hudec, M. R., Norton, I. O., 2019. Upper Jurassic structure and evolution of the Yucatán and Campeche subbasins, southern Gulf of Mexico: AAPG Bulletin, 103, 1133–1151.

Hudec, M. R., Norton, I. O., Jackson, M. P. A., Peel, F. J., 2013. Jurassic evolution of the Gulf of Mexico salt basin: AAPG Bulletin, 97, 1683–1710.

Huffman, A. C. J., Kinney, S. A., Biewick, L., Mitchell, H. R., Gunther, G. L., 2004. Gulf Coast Geology (GCG) Online—Miocene of Southern Louisiana, Version 1: USGS Data Series 90-A.

Imbert, P., 2005. The Mesozoic opening of the Gulf of Mexico—Part 1: Evidence for oceanic accretion during and after salt deposition: 25th Annual Bob F. Perkins Research Conference: Petroleum Systems of Divergent Continental Margin Basins, 1119–1150.

Imbert, P., Philippe, Y., 2005. The Mesozoic opening of the Gulf of Mexico — Part 2: Integrating seismic and magnetic data into a general opening model: 25th Annual Bob F. Perkins Research Conference: Petroleum Systems of Divergent Continental Margin Basins, 1151–1189.

Tan X., Kodama, K.P., Gilder, S., Courtillot, V., 2007. Rock magnetic evidence for inclination shallowing in the Passaic Formation red beds from the Newark basin and a systematic bias of the

Late Triassic apparent polar wander path for North America, Earth and Planetary Science Letters, v. 254, 345-357.

Lin, P., 2018. Crustal structure and tectonostratigraphic evolution of the eastern Gulf of Mexico Basin: Unpublished Ph.D. dissertation, University of Houston, 154p.

Lin, P., Bird, D. E., Mann, P., 2019. Crustal structure of an extinct, late Jurassic-to-earliest Cretaceous spreading center and its adjacent oceanic crust in the eastern Gulf of Mexico: Marine Geophysical Research, 1–24.

MacRae, G., Watkins, J. S., 1995. Early Mesozoic rift stage half-graben formation beneath the DeSoto Canyon salt basin, northeastern Gulf of Mexico: Journal of Geophysical Research: Solid Earth, 100, 17795–17812.

Marton, G., Buffler, R. T., 1994. Jurassic reconstruction of the Gulf of Mexico Basin: International Geology Review, 36, 545–586.

Marton, G. L., Buffler, R. T., 1999. Jurassic-early Cretaceous tectono-paleogeographic evolution of the southeastern Gulf of Mexico basin, in P. Mann, ed., *Caribbean Basins: Sedimentary Basins of the World*: Elsevier Science B. V., Amsterdam, 4, 63–91.

Meyer, B., Saltus, R., Chulliat, A., 2017. EMAG2: Earth magnetic anomaly grid (2-arc-minute resolution) version 3: National Center for Environmental Information, NOAA.

Nguyen, L. C., Mann, P., 2016. Gravity and magnetic constraints on the Jurassic opening of the oceanic Gulf of Mexico and the location and tectonic history of the Western Main transform fault along the eastern continental margin of Mexico: *Interpretation*, 4, no. 1, SC23–SC33.

Nielsen, C.,Thybo, H., 2009. No Moho uplift below the Baikal rift zone: Evidence from a seismic refraction profile across southern Lake Baikal: Journal of Geophysical Research: Solid Earth, 114, 1–22.

Pascoe, R., Nuttall, P., Dunbar, D., Bird, D., 2016. Constraints on the timing of continental rifting and oceanic spreading for the Mesozoic Gulf of Mexico Basin, in C. M. Lowery, J. W. Snedden, and N. C. Rosen, eds., *Mesozoic of the Gulf Rim and Beyond: New progress in science and exploration of the Gulf of Mexico Basin*, Gulf Coast Section SEPM Foundation, 81–122.

Pindell, J., Miranda, E. C., Cerón, A., Hernandez, L., 2016. Aeromagnetic map constrains Jurassic-Early Cretaceous syn-rift, breakup, and rotational seafloor spreading history in the Gulf

of Mexico, in C. M. Lowery, J. W. Snedden, and N. C. Rosen, eds., *Mesozoic of the Gulf Rim and Beyond: New Progress in Science and Exploration of the Gulf of Mexico Basin*: SEPM Society for Sedimentary Geology 35, 123–153.

Pindell, J. L., Kennan, L., 2009. Tectonic evolution of the Gulf of Mexico, Caribbean and northern South America in the mantle reference frame: An update, in K. H. James, M. A. Lorente, and J. L. Pindell, eds., *The origin and evolution of the Caribbean plate*: Geological Society of London Special Publications 328, 1–55.

Planke, S., Symonds, P. A., Alvestad, E., Skogseid, J., 2000. Seismic volcanostratigraphy of large-volume basaltic extrusive complexes on rifted margins: Journal of Geophysical Research: Solid Earth, 105, 19335–19351.

Rowan, M. G., 2014. Passive-margin salt basins: Hyperextension, evaporite deposition, and salt tectonics: Basin Research, 26, 154–182.

Sandwell, D. T., Muller, R. D., Smith, W. H. F., Garcia, E., Francis, R., 2014. New global marine gravity model from CryoSat-2 and Jason-1 reveals buried tectonic structure: Science, 346, 65–67.

Schnetzler, C. C., 1985. An estimation of continental crust magnetization and susceptibility from Magsat data for the conterminous United States: Journal of Geophysical Research: Solid Earth, 90, 2617–2620.

Shay, J., Tréhu, A., 1993. Crustal structure of the central graben of the Midcontinent Rift beneath Lake Superior: Tectonophysics, 225, 301–335.

Snedden, J., Eddy, D., Christeson, G., Van Avendonk, H., Olson, H., Ganey-Curry, P., Norton, I., 2013. A new temporal model for Eastern Gulf of Mexico Mesozoic deposition: Gulf Coast Association of Geological Societies Transactions, 63, 609–612.

Snedden, J. W., Norton, I. O., Christeson, G. L., Sanford, J. C., 2014. Interaction of deepwater deposition and a mid-ocean spreading center, Eastern Gulf of Mexico Basin, USA: Gulf Coast Association of Geological Societies Transactions, 64, 371–383.

Steier, A., Mann, P., 2019. Late Mesozoic gravity sliding and Oxfordian hydrocarbon reservoir potential of the northern Yucatan margin: Marine and Petroleum Geology, 103, 681–701.

Tian, X., Buck, W. R., 2019. Lithospheric thickness of volcanic rifting margins: Constraints from seaward- dipping reflectors: Journal of Geophysical Research: Solid Earth, 124, 3254–3270.

Van Avendonk, H. J. A., Christeson, G. L., Norton, I. O., Eddy, D. R., 2015. Continental rifting and sediment infill in the northwestern Gulf of Mexico: Geology, 43, 631–634.

Warwick, P. D., 2017. Geologic assessment of undiscovered conventional oil and gas resources in the Lower Paleogene Midway and Wilcox Groups, and the Carrizo Sand of the Claiborne Group, of the Northern Gulf coast region: USGS open-file report 2017-1111.

Weil. A.B., Yonkee, A., 2009. Anisotropy of magnetic susceptibility in weakly deformed red beds from the Wyoming salient, Sevier thrust belt: Relations to layer-parallel shortening and orogenic curvature, Lithosphere, v1, No. 4, 235-256.

The following chapter is intended for submission to the Tectonophysics.

CHAPTER 3: MESOZOIC OPENING HISTORY OF THE GREATER GULF OF MEXICO BASIN BASED ON A 3D GRAVITY INVERSION TO DERIVE CRUSTAL THICKNESS

3.1 Introduction

After several decades of research, the Gulf of Mexico (GOM) basin opening history remains controversial, especially for its deeply-buried, Phase 1 continental rifting stage during the late Triassic and early Jurassic (Eddy et al., 2014). The rifted continental margins between the North American plate and the Yucatan plate have been debated for decades for three reasons: 1) no magnetic isochrons have been identified for the late Jurassic oceanic spreading history of Phase 2 (Lin et al., 2019); 2) deeply-buried Phase 1 Mesozoic rifts that underlie the coastal plains deepwater areas of the GOM have not been directly dated and are known mainly from indirect, geophysical imaging; and 3) the southern conjugate margin of the Gulf of Mexico and Yucatan margins in the Caribbean and northern South America region have been strongly overprinted by Cenozoic, convergent and strike-slip tectonics (Frederick et al., 2020).

Several models exist for the rigid reconstruction of seafloor spreading in the GOM and include the models of Pindell (1985), Nguyen and Mann (2016), Pindell et al. (2016), and Minguez et al. (2020). In addition to these rigid plate models, Dunbar and Sawyer (1987) and Kneller and Johnson (2011) performed non-rigid plate reconstruction by estimating crustal thickness from local isostasy and restored the stretched margins to a pre-rift thickness. However, both these rigid and non-rigid reconstructions were carried out prior to the release of the latest satellite gravity data from Sandwell et al. (2014) that clearly delineated the spreading centers, fracture zones in late

Jurassic oceanic crust that underlies the central GOM basin and the COBs separating oceanic and thinned continental crust (Figure 3.1).

In addition to the advances in satellite gravity, the Gulf of Mexico Basin Opening (GUMBO) project for collecting long crustal refraction lines across the northern GOM basin provided new rifting constraints that included the discovery of several high-velocity zones within the lower continental crust that were interpreted as magmatic underplating beneath the northeastern GOM basin (Christeson et al., 2014; Eddy et al., 2014).

Figure 3.1. A) Geographic setting of the Gulf of Mexico (GOM) with the black line representing the continent-ocean boundary (COB) from Sandwell et al. (2014) and the yellow lines representing the extinct late Jurassic, oceanic spreading center and fracture zones from Lin et al. (2019). The black dashed line shows the up-dip limit of Jurassic salt deposition from Rowan (2014). Triassic rifts in red are compiled from Liu and Mann (2021, Chapter 4) and Lin (2018). The white line adjacent to the oceanic crust is the marginal rift from Liu and Mann (2021, Chapter 4). B) Map showing the datasets used in this study overlain onto a bathymetric map. Thin, white lines show the locations of depth-converted 2D seismic reflection data from Spectrum (now TGS). Black inverted triangles are seismic refraction stations from the USGS earthquake database and the following publications: Ewing et al., 1960; Cram, 1961; Antoine and Ewing, 1963; Hales et al., 1970; Del Castillo G, 1974; Ibrahim et al., 1981; Ibrahim and Uchupi, 1982; Ebeniro et al., 1986; Nakamura et al., 1988; Kim et al., 2000. Yellow dots represent the wells that were used for density information used in gravity modeling. C) Depth to basement map compiled from seismic interpretations and published datasets by Bayley and Muehlberger (1968), Laske et al. (2013), and Straume et al. (2019). Numbers are different basement terranes from Netto and Dunbar (2019). 1 = Precambrian Granite rhyolite province. 2 = late Paleozoic Appalachian deformation front; 3 = Peri-Laurentian terranes; 4 = Peri-Gondwanan terranes; 5 = Suwannee terrane; 6 = Wiggins arch; 7 = Sabine block; 8 = Grenville terranes; 9 = Coahuila; 10 = Yucatan block; 11 = Tamaulipas arch; 12 = Chicxulub impact site. D) Map summarizing the confidence levels for mapping the top of crystalline basement based on seismic reflection and refraction data of areas within the GOM and southern Appalachians (higher confidence) and gridded satellite gravity data (lower confidence) covering the entire areas of the map that includes the GOM and its surrounding land areas. Lower confidence assigned to global grids of gravity and magnetic data reflects smoothing between actual data points. Oceanic crust is easily recognizable based on its distinctive seismic reflector and therefore mapped with intermediate to high confidence. The seismic interpretation of thinned continental crust region is considered an intermediate confidence zone as these areas are deeply buried and not always well imaged.

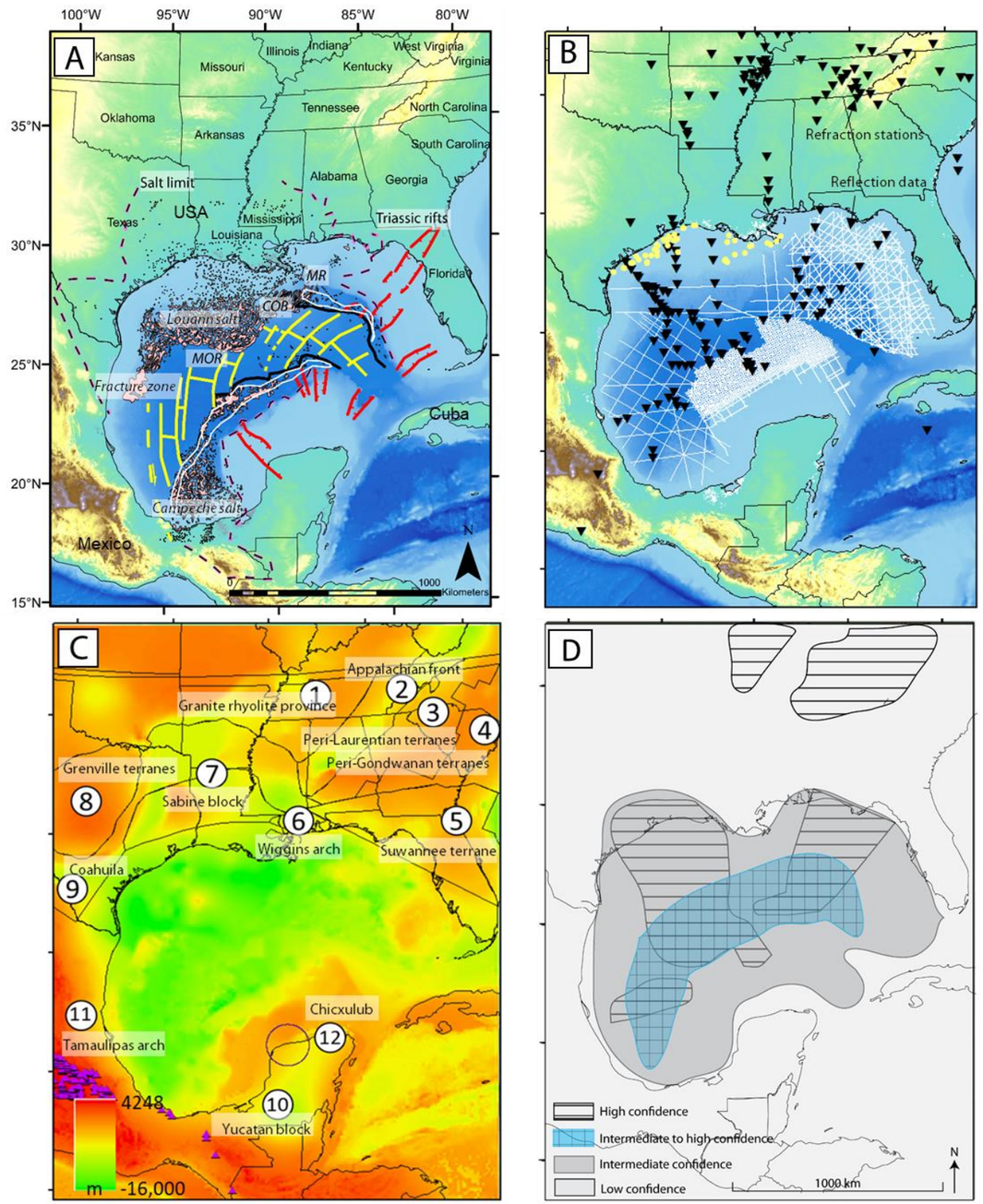
A
100°W
95°W
90°W
85°W
80°W
35°N
30°N
25°N
20°N
15°N
Kansas
Missouri
Illinois
Indiana
Kentucky
West Virginia
Virginia
Oklahoma
Arkansas
Tennessee
North Carolina
South Carolina
Alabama
Georgia
Salt limit
USA
Texas
Mississippi
Louisiana
Triassic rifts
Florida
MR
COB
Louann salt
MOR
Fracture zone
Cuba
Campeche salt
Mexico
N
0
1000
Kilometers
B
Refraction stations
Reflection data
C
Appalachian front
Granite rhyolite province
Peri-Laurentian terranes
Peri-Gondwanan terranes
Grenville terranes
Sabine block
Wiggins arch
Suwannee terrane
Coahuila
Chicxulub
Tamaulipas arch
Yucatan block
4248
m
-16,000
D
High confidence
Intermediate to high confidence
Intermediate confidence
Low confidence
1000 km
N

This study follows the methodology that has been previously applied to derive full-fit tectonic reconstructions for the Australia-Antarctica conjugate margin (Williams et al., 2011) and conjugate margins of the South China Sea (Bai et al., 2015). Estimates of the total thickness and variability of the crust is crucial for constructing crustal-scale gravity models because of the large density contrast between crust and mantle rocks.

In this chapter, I develop a new 3D crustal model based on the integration of an extensive GOM database of seismic reflection data, seismic refraction data, well data, and public-access gravity and magnetic grids. This chapter uses a full-fit restoration of the extended continental crust of the conjugate margins to estimate the pre-rift locations of the restored continent-ocean boundary (RCOB) and more precise displacement paths for the continental blocks during Phases 1 and 2 of the Mesozoic GOM opening history.

3.2 Tectonic setting

The formation of the GOM is associated with the breakup of Pangea during the late Triassic to earliest Cretaceous (Salvador, 1987; Marton and Buffler, 1994; Bird et al., 2005; Nguyen and Mann, 2015; Lin et al., 2019). The GOM is surrounded by several tectonic terranes of Precambrian and Paleozoic age (Netto and Dunbar, 2019; Figure 3.1C). These terranes were juxtaposed and deformed during several tectonic events that included the Precambrian Grenville orogeny, the opening of the Iapetus Ocean, multiple Appalachian orogenic episodes, and Mesozoic rifting that led to the opening of the Atlantic Ocean (Klitgord and Schouten, 1986; Bajgain, 2011; Singleton, 2016).

The rocks underlying the southeastern United States and its coastal plain were deformed during the Late Paleozoic Alleghenian orogeny that formed when Gondwana collided with Peri-

Gondwana/Laurentia to form the Appalachian-Ouachita fold-thrust belt (Hatcher, 2002; Nance et al., 2012) along a Late Paleozoic suture zone now marked by the Higgins-Zietz magnetic boundary in the southeastern USA (Marzen et al., 2020).

GOM rifting began in the Late Triassic between the North and South American plates and the intervening Yucatan continental block and was followed by late Jurassic seafloor spreading that accompanied a 40º counterclockwise rotation of the Yucatan block (Salvador, 1987; Marton and Buffler, 1994). Oceanic spreading separated a single large, late Jurassic salt basin into the Louann salt basin in the US GOM and the Campeche salt basin in the Mexican GOM (Hudec et al., 2013; Eddy et al., 2014; Nguyen and Mann, 2016; Steier and Mann, 2019; Lin et al., 2019Hudec and Norton, 2019).

3.3 Methodology

3.3.1 Seismic data and basement mapping

A detailed map of the top of the crystalline basement is one of the critical components for a 3D gravity inversion. This study creates a top basement map of the GOM across a 754,000 km^2 area of the Florida and Mexico using 2D seismic reflection data that were pre-stack, depth-converted in offshore Mexico and Florida (Figure 3.1b). To interpret the top of the basement, this chapter integrates 2D seismic reflection data with 178 seismic refraction data points compiled from the USGS earthquake database and published literature (Ewing et al., 1960; Cram, 1961; Antoine and Ewing, 1963; Hales et al., 1970; Del Castillo G, 1974; Ibrahim et al., 1981; Ibrahim and Uchupi, 1982; Ebeniro et al., 1986; Nakamura 1988; Kim et al., 2000).

The top of oceanic crust is interpreted based on the oceanic crustal velocities of 4.44 to 5.70 km/s and the top of continental crust is interpreted based on continental velocities of 6.22 to

6.88 km/s (Christensen and Mooney, 1995; White et al., 1992). Refraction data results were used to interpret the top of crystalline basement in the continental domain because the seismic reflector is commonly subtle or absent in the continental domain.

The top of the oceanic crust horizon on the reflection data is easily recognizable as a rugose boundary with underlying chaotic reflectors that are overlain by coherent and stratified reflectors of the overlying Paleozoic and Mesozoic sedimentary layers (Figure 3.1C). I integrated from published maps of the top crystalline basement by Bayley and Muehlberger (1968), Laske et al. (2013), Straume et al. (2019) in areas that were not covered by any other seismic reflection or refraction data.

3.3.2 3D gravity modeling

For 3D gravity modeling, this study uses: 1) free-air gravity grid from Sandwell et al. (2014) for the offshore area; 2) the Decade of North American Geology (DNAG) gravity grid that was compiled by the National Oceanic and Atmospheric Administration for the onshore USA; and 3) the Earth Gravitational Model (EGM2008) from Pavlis et al. (2012) for onshore area of Mexico.

The 3D gravity model consists of four horizons that include: 1) a surface station, 2) a merged topographic and bathymetric surface, 3) the top of the crystalline basement, and 4) the Moho surface. The topographic data is from the public-access Terrain Base and the bathymetric data is compiled from the high-resolution bathymetry from the Bureau of Ocean Energy Management (BOEM) combined with Terrain Base. The top of the crystalline basement was from seismic interpretation merged with published grids and the initial Moho surface was derived from an Airy isostatic calculation from Blakely (1995):

$$d_m = h(\rho_t / \Delta\rho) + d_s$$

In this equation, all depths are in km and d_m is the theoretical, isostatic Moho depth, h is the topographic elevation, ρ_t is average crustal density, $\Delta\rho$ is the density contrast between crystalline crust and upper mantle, and d_s is isobaric Moho depth at the coast (assumed to be 33 km as the start value for iterations).

The density of water, crystalline crust, and upper mantle used in this model were 1.03, 2.85, and 3.3 g/cm^3, respectively. These values are consistent with the values used in a 3D gravity model for the eastern GOM by Lin et al. (2019). The density of the sedimentary layer can be approximated by a continuous function (Cordell, 1973). Therefore, this study uses an exponential decay function (1) below that was derived from 45 wells along the coast with the depth in meters.

$$D= 2.7-0.65*\exp(-0.0002*\text{depth}) \quad (1)$$

Unconstrained inversion allows the inversion to modify the Moho surface freely; refraction stations were then used to constrain the inversion process because the Moho surface movement is restricted during the inversion by a constraining grid that limits this movement as a function of control (refraction stations) proximity. While gravity inversion can produce a range of solutions, I integrated seismic reflection, refraction, and well data to minimize this range. The forward calculations prior to structural gravity inversion were performed using Seequent Oasis Montaj, which was based on a frequency-domain. I used the Fourier transform of the gravitational anomaly to calculate the gravity anomaly produced by the uneven layers as described by Parker (1973). The one-dimensional expression of the sum of Fourier transforms is defined as:

$$F(\Delta g) = -2\pi G\rho e^{(-kz_0)} \sum_{n=1}^{\infty} \frac{k^{n-2}}{n!} F[h^n(x)] \quad (2)$$

In this equation, $F(\Delta g)$ is the Fourier transform of the gravity anomaly, G is the Newton's gravitational constant, ρ is the density contrast across the interface, k is the wave number, h(x) is the depth to the interface and z_0 is the observing plane given by $z=z_0$ in Cartesian axes.

The gravity structural inversion schemes are based on unpublished algorithms developed by Bill Pearson and implemented in the GM-SYS 3D module.

The beta factors implied by the crustal thickness model are calculated from the equation $\beta=tc_0/tc_{now}$, where tc_0 is the thickness of unstretched crust and tc_{now} is the present-day crustal thickness from gravity inversion.

3.3.3 Restoring the COBs

The reconstruction involves two steps: 1) performing a rigid reconstruction to close the area of late Jurassic oceanic crust using the fracture zones visible on marine gravity images; and 2) performing a non-rigid reconstruction that takes into account the crustal extension during rifting.

In order to estimate the location of the previous un-rifted margin, several 2D crustal profiles were extracted from the 3D crustal thickness model in order to estimate the areas of the extended, conjugate margins. I assumed a pre-rift crustal thickness of 36 km, which is the average continental crustal thickness of North America (Braile, 1989; Chulick and Mooney, 2002); I then calculated the distance to the RCOB (Figure 3.2). The RCOB locations are used as inputs for the plate reconstruction using GPlates software.

Figure 3.2. 2D, northwest to southeast, cross-sectional profile A-A’ as taken from the 3D crustal model. A) Location of the profile A-A' on the regional crustal thickness map. B) Present-day crustal profile of the GOM from 3D gravity inversion showing its two rifted conjugate margins with an area of late Jurassic oceanic crust in the center. C) Schematic cross-section of the pre-rift GOM crustal structure based on the assumption of a pre-rift crust thickness of 36 km.

A.

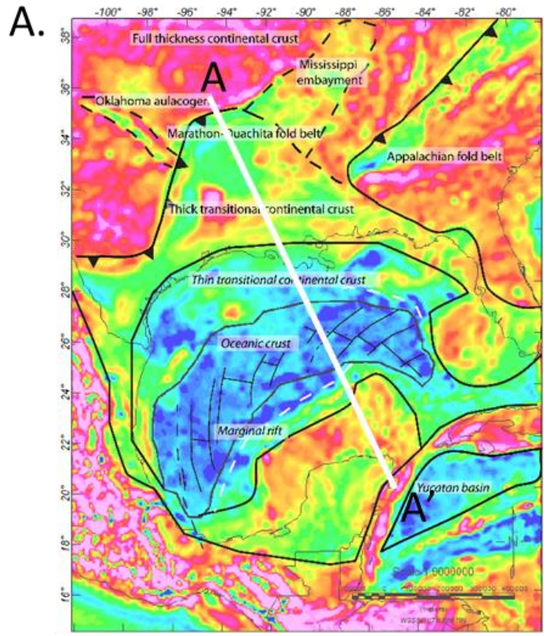
Full thickness continental crust
Mississippi embayment
Oklahoma aulacogen
Marathon-Ouachita fold belt
Appalachian fold belt
Thick transitional continental crust
Thin transitional continental crust
Oceanic crust
Marginal rift
Yucatan basin
A
A'

B.

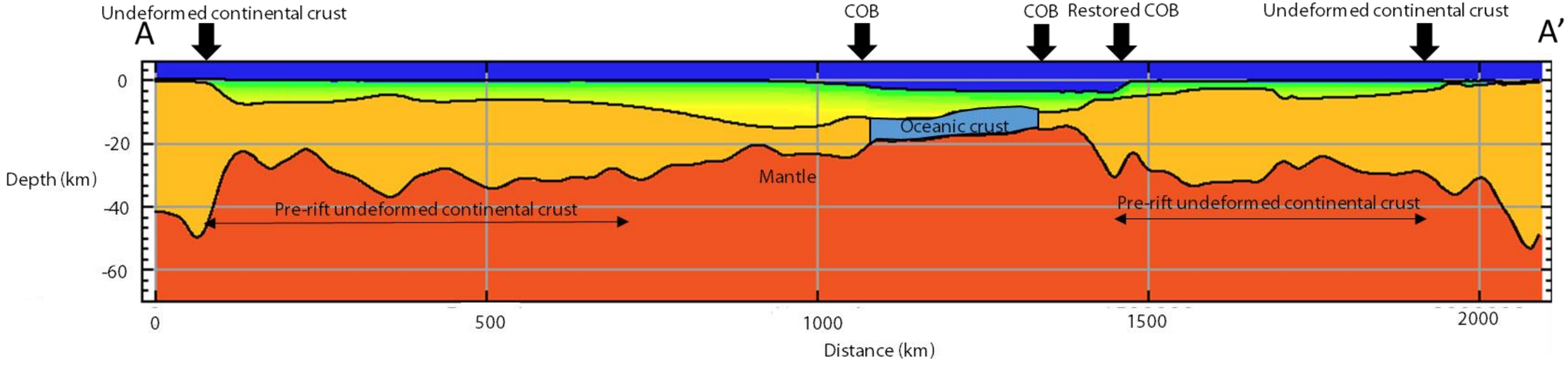
US GOM
Yucatan GOM
Undeformed continental crust
COB
COB
Restored COB
Undeformed continental crust
A
A'
Oceanic crust
Mantle
Pre-rift undeformed continental crust
Pre-rift undeformed continental crust
Depth (km)
0
-20
-40
-60
0
500
1000
1500
2000
Distance (km)

C.

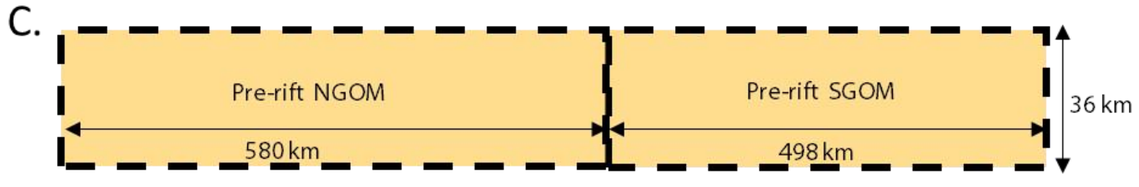
Pre-rift NGOM
580 km
Pre-rift SGOM
498 km
36 km

The relative motion between North American plate, South American plate, and African plate is taken from the GPlates global reconstructions as summarized by Matthews et al. (2016). This study tests two different plate tectonic scenarios for the directions of plate motion of the Yucatan block relative to North America and examines the overlap or underlap consequences of both scenarios for the full-fit GOM reconstruction.

3.3.4 Euler poles for reconstruction

Nguyen and Mann (2016) mapped the fracture zones and calculated the rotation pole of the Yucatan block during the seafloor spreading stage at ~160 Ma using marine satellite gravity data from Sandwell et al. (2014). This chapter adopts the pole of rotation located in western Cuba (84°W, 22.5°N) from Nguyen and Mann (2016) and uses it for rigid reconstructions. This chapter calculates the small circle paths for the conjugate margins based on the finite rotation pole generated in GPlates for the Jurassic-Cretaceous period from 160 Ma to 140 Ma.

For the continental rifting stage, this study uses two methods to estimate the rotation pole. The first method is based on the work of Hellinger (1981), who fitted magnetic isochrons and fracture zones by great circle segments, calculated the best fit rotation poles within a search matrix (longitude and latitude matrix), and used a least-squares fitting method to minimize the weighted least squares measure of the fit.

This study uses the RCOB from each conjugate margin of the GOM as inputs that are analogous to using magnetic isochron picks that would carry the assumption that the GOM continental rifting occurred synchronously - rather than diachronously from west to east as proposed by Marton and Buffler (1999). This study also uses a method by Bird et al. (2007) which

takes an input geographic seed location for the center of a scan matrix (latitude and longitude) and a scan increment (in degrees) to search for the best-fit pole until a 90% confidence solution is achieved.

3.4 Results and interpretation

3.4.1 Crustal structure of the GOM

The initial inversion-derived Moho surface result that was created without using constraints from seismic refraction data is shown in Figure 3.3A. The calculations were iterated until the setup parameter convergence limit of 1.0 mgal was achieved. The initial unconstrained inversion of the initial Moho shows that the Moho elevation depth ranges from -48.2 km to -10.4 km (Figure 3.3A). After the initial unconstrained Moho was determined, the compiled refraction data was stitched to the modeled Moho horizon.

Figure 3.3. A) Moho surface of the GOM derived from an unconstrained 3-D gravity structural inversion. B) Moho surface derived from constrained 3-D gravity structural inversion. The black dots are refraction stations from compiled literature that were used for Moho corrections. The COB is defined by the crustal thickness less than 10 km except in the NW GOM where the COB is adjacent to a northeast-trending deeper Moho expression. The extinct spreading center and fracture zones are compiled from Lin et al. (2019).

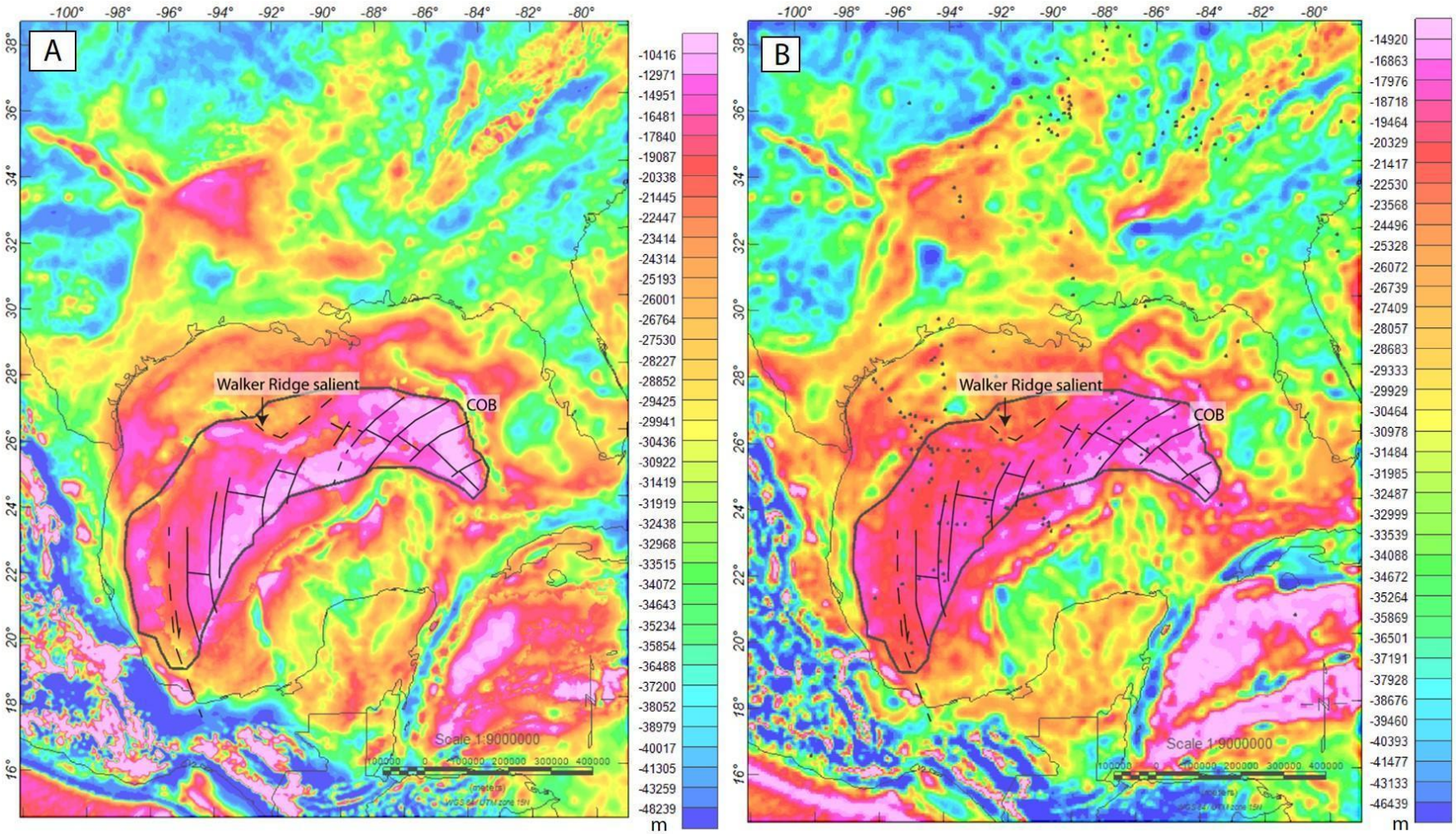
A
B
Walker Ridge salient
COB
Scale 1:9000000
m

The gravity inversion constrained by the seismic refraction data derived the Moho depth from -46.4 km to -14.9 km (Figure 3.3B). The most significant difference between the unconstrained inversion and constrained inversion results are most apparent in regions of younger oceanic crust in the Caribbean Sea - such as the Yucatan basin and Cayman trough. The Moho near the Yucatan Basin and the Cayman trough were adjusted upwards by the constrained inversion.

Crustal thickness was calculated by subtracting the basement from the inverted Moho. The resulting crustal thickness varies from 6.6 km to 50.7 km (Figure 3.4). Four distinct crustal domains are delineated from this crustal thickness mapping. Refraction profile GUMBO line 3 in the northeastern GOM shows that the oceanic crust has an average thickness of 8.1 km with a maximum thickness of > 10 km (Eddy et al., 2014). Therefore, the continent-ocean boundary (COB) was defined for this study based on a crustal thickness of 10 km - except for the Bravo trough area in the western GOM that is separated from the GOM oceanic crust by an area of thicker crust known as the BAHA high (Hudec et al., 2013). I acknowledge the presence of the thin crust to the northwest of the BAHA high, and for this study I adopt the conclusion from the GUMBO experiment for that this area is thinned continental crust (Van Avendonk et al., 2015; Eddy et al., 2018;).

Figure 3.4 A) Uninterpreted crustal thickness map of the GOM derived from constrained 3-D gravity structural inversion. B) Interpreted crustal thickness map showing four crustal provinces discussed in the text.

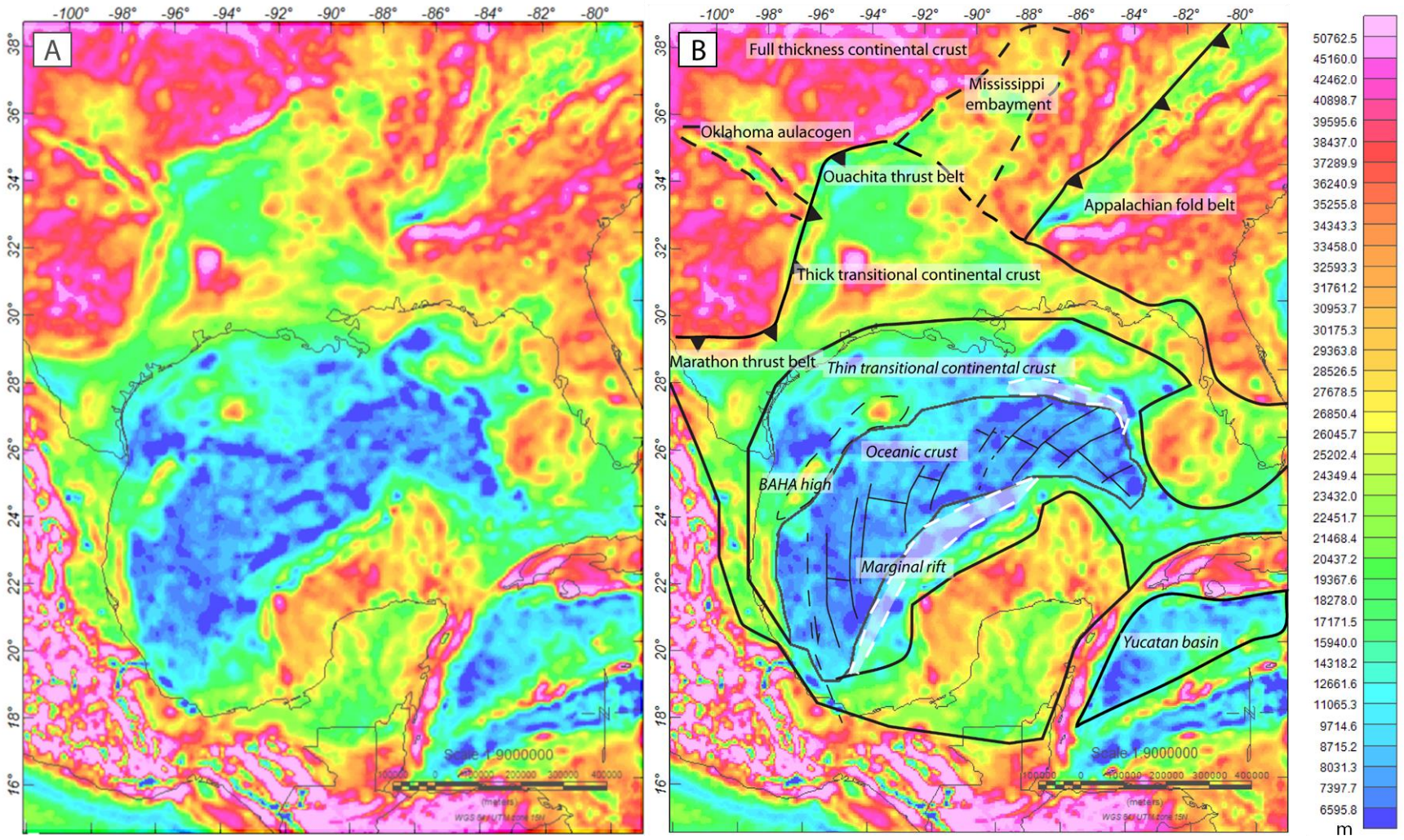
A
B
Full thickness continental crust
Mississippi embayment
Oklahoma aulacogen
Ouachita thrust belt
Appalachian fold belt
Thick transitional continental crust
Marathon thrust belt
Thin transitional continental crust
Oceanic crust
BAHA high
Marginal rift
Yucatan basin
50762.5
45160.0
42462.0
40898.7
39595.6
38437.0
37289.9
36240.9
35255.8
34343.3
33458.0
32593.3
31761.2
30953.7
30175.3
29363.8
28526.5
27678.5
26850.4
26045.7
25202.4
24349.4
23432.0
22451.7
21468.4
20437.2
19367.6
18278.0
17171.5
15940.0
14318.2
12661.6
11065.3
9714.6
8715.2
8031.3
7397.7
6595.8
m

The oceanic crust that underlies the deep, central GOM has a crustal thickness of less than 10 km (Lin et al., 2019) (Figure 3.4). The thin transitional continental crust in the landward directions shows the crustal thicknesses increase to 10-20 km. Thick transitional continental crust occurs farther landwards with these thicker areas of crust varying from 20-36 km. Crust thicker than 36 km is considered to be unstretched continental crust underlying the cratonic areas of the plates. The crustal domain identification is consistent with thicknesses that were previously identified for each of these crustal domains (Sawyer et al., 1991). The geometry of the basin shows apparent asymmetry where the northern GOM margin extends in width over 1000 km in the north-south direction - while the southern GOM margin only extends 600 km in north-south direction, as seen on the regional cross-section shown in Figure 3.2B (Marton and Buffler, 1999).

To evaluate the 3D gravity inversion, the spatial distribution of the difference between the calculated gravity response and the observed gravity data is shown in Figure 3.5A. The misfit distribution is normally distributed without any significant systematic trends and shows a mean of -0.85 mgal with a standard deviation of 14.6 mgal. A comparison between unconstrained inversion and constrained inversion calculation results are shown in Table 1.

The highest misfit is located onshore Mexico (Figure 3.5C) that is understandable given the complex density structures associated with the Cenozoic volcanic and orogenic activity in this large, continental region. Comparison between Moho depths inverted from gravity and derived from refraction data shows the root mean square difference between the two methods is 4.08 km with an average difference of 3.12 km (Figure 3.5B).

Figure 3.5. A) Map of the gravity inversion error grid shows the misfit between the calculated and observed fields. The inversion error is low and uniform for most areas except for the area of onshore Mexico. B) Crossplot of seismic Moho and gravity inverted Moho. Overall, the RMS misfit is ~4 km. C) Misfit statistics of the error grid show the mean of misfit is -0.85 mgal and the standard deviation is 14.6 mgal.

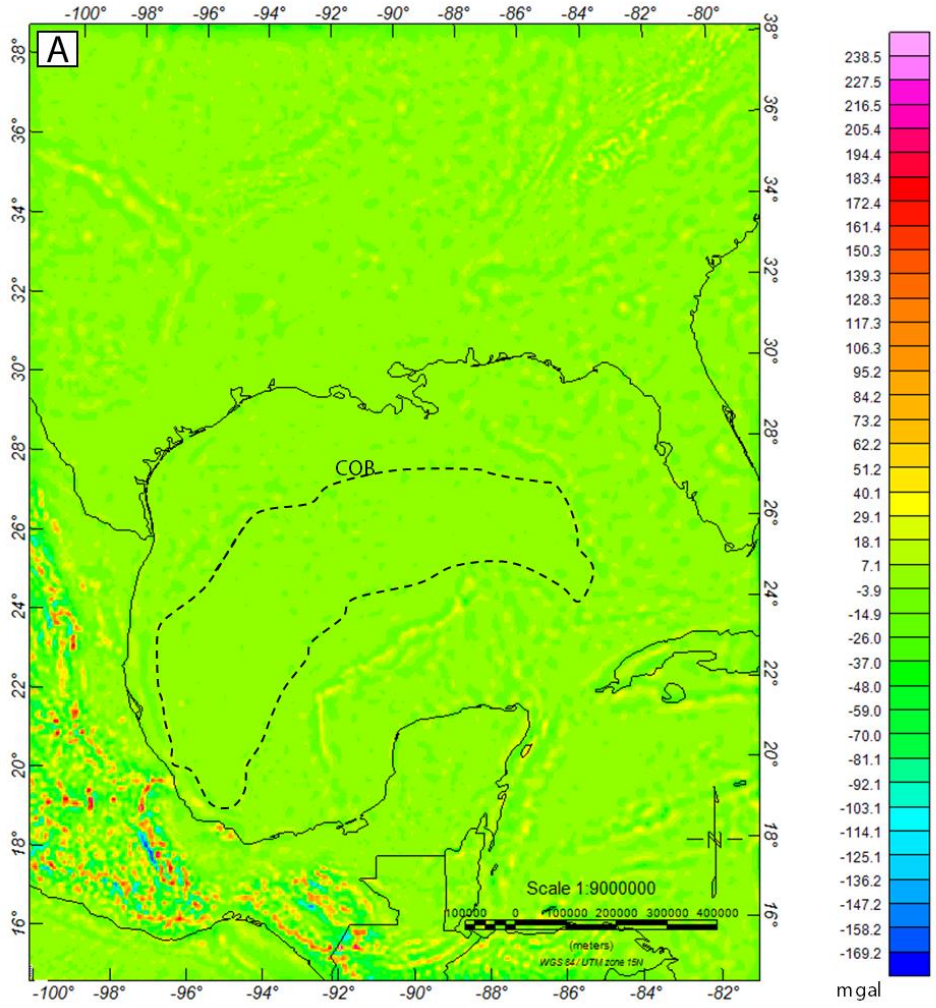
A
COB
Scale 1:9000000
(meters)
WGS 84 / UTM zone 15N
238.5
227.5
216.5
205.4
194.4
183.4
172.4
161.4
150.3
139.3
128.3
117.3
106.3
95.2
84.2
73.2
62.2
51.2
40.1
29.1
18.1
7.1
-3.9
-14.9
-26.0
-37.0
-48.0
-59.0
-70.0
-81.1
-92.1
-103.1
-114.1
-125.1
-136.2
-147.2
-158.2
-169.2
mgal

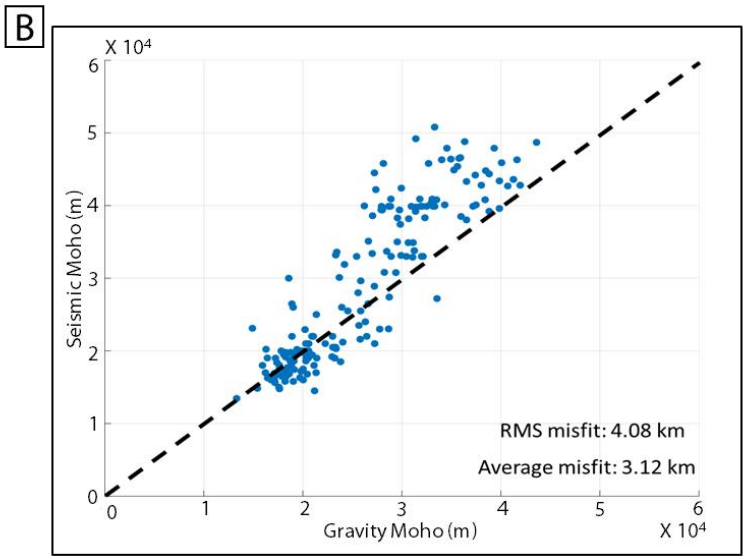
B
X 10⁴
Seismic Moho (m)
Gravity Moho (m)
RMS misfit: 4.08 km
Average misfit: 3.12 km

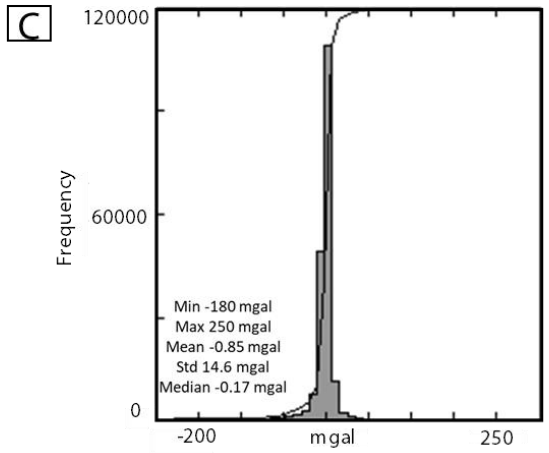
C
Frequency
Min -180 mgal
Max 250 mgal
Mean -0.85 mgal
Std 14.6 mgal
Median -0.17 mgal
mgal

Table 1. Comparison of misfit between calculated gravity response and observed gravity response during unconstrained inversion and constrained inversion.

(mgal)	Unconstrained inversion	Constrained inversion
Minimum value	-223.6	-180
Maximum value	615.44	250
Mean value	1.32	-0.85
Standard deviation	32.89	14.6
Median	0.6	-0.17

A beta or stretch factor map is shown in Figure 3.6. This map highlights the variable amounts of extension of different crustal domains along the approximate trends of those extended areas. The Apalachicola rift, Tampa embayment, South Florida basin, and GOM marginal rift system all show high stretch factors in the 4-5 range in the offshore region. The stretch factor varies from 1-2 in the thick transitional continental crustal domain and 3-6 in the thin transitional continental crustal domain.

The up-dip limit of salt from Rowan (2014) and Dooley et al. (2013) correlates with edges of stretched continental crust except near the center of the Ouachita thrust front. This is consistent with models for the salt forming in an unfaulted sag basin developed above rifts that formed during the Triassic-Jurassic Phase 1rift phase (Eddy et al., 2014; Chapter 4, this dissertation).

Figure 3.6. Map of beta or stretch factor (β) variations for the greater GOM region. Beta factor is calculated from β =Tc0/Tcnow – where Tc0 is the initial thickness of crust and Tcnow is the present-day crustal thickness from gravity inversion. Tc0 is assumed to be 36 km based on compiled data.

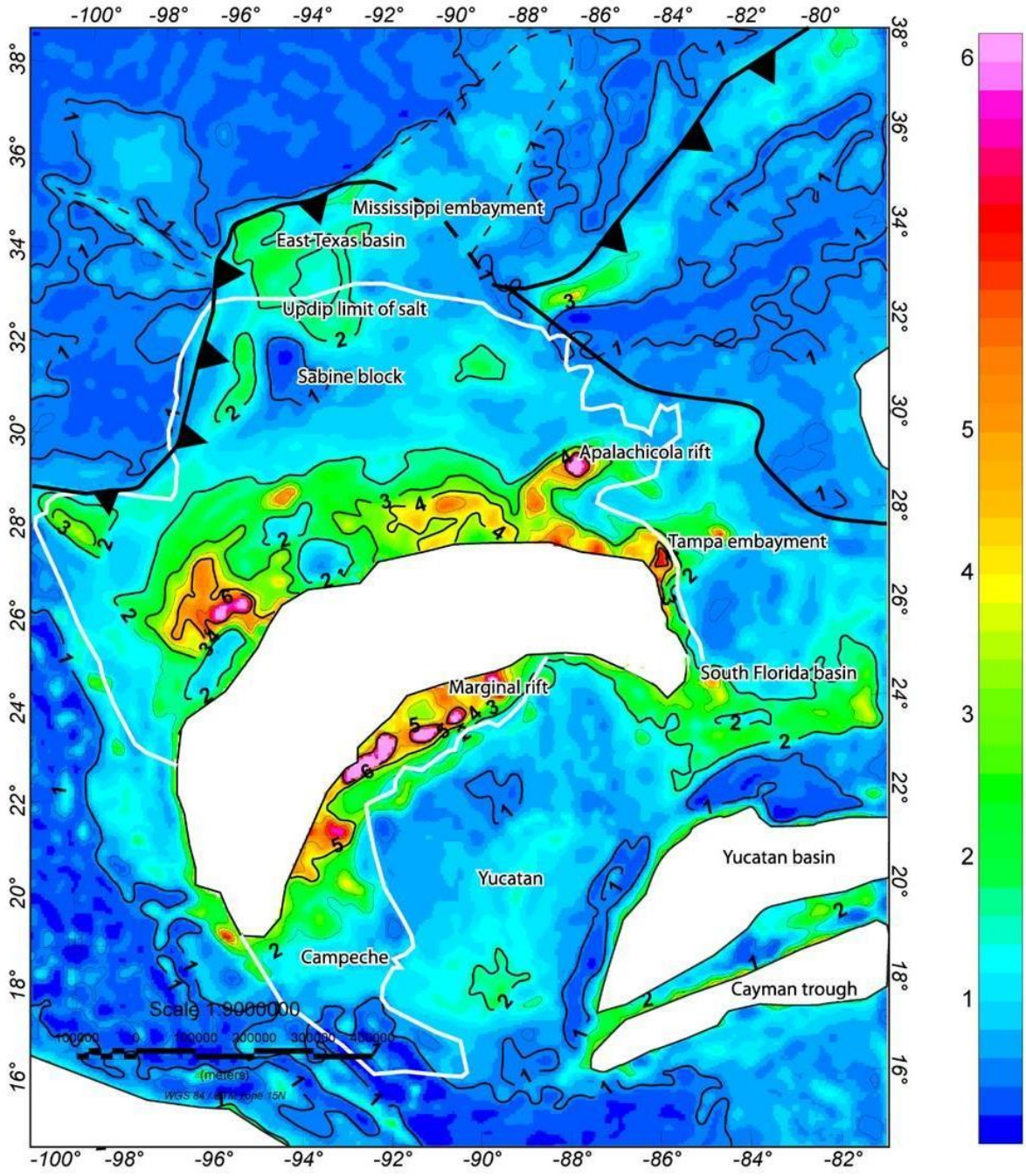

3.4.2 Full-fit reconstruction of the GOM basin

The rigid reconstruction using the pole of rotation from Nguyen and Mann (2016) rotated the Yucatan block counterclockwise through an angle of 43 degrees. In the late Jurassic (160 Ma), the Yucatan block is restored to its relative position prior to seafloor spreading (Figures 3.7A and 3.9A). The RCOB location is estimated based on palinspastic restoration by assuming the volume of the crust remains the same through the rifting process.

Figure 3.7. A) Rigid reconstruction restoring the Yucatan block prior to seafloor spreading along the oceanic fracture zones using a pole in NW Cuba from Nguyen and Mann (2016) with plate motion overlay. B) Plate configuration achieved by a continuous clockwise rotation of the Yucatan block following the same small circles. Yellow triangles are the restored COB (RCOB) on the US GOM. Blue circles are the RCOB on the Yucatan side. The brown area shows the maximum overlap between the Yucatan block and the South American plate is 319,323 km^2. The shaded area shows the minimum overlap between the Yucatan block and South American plate is 45,730 m^2.

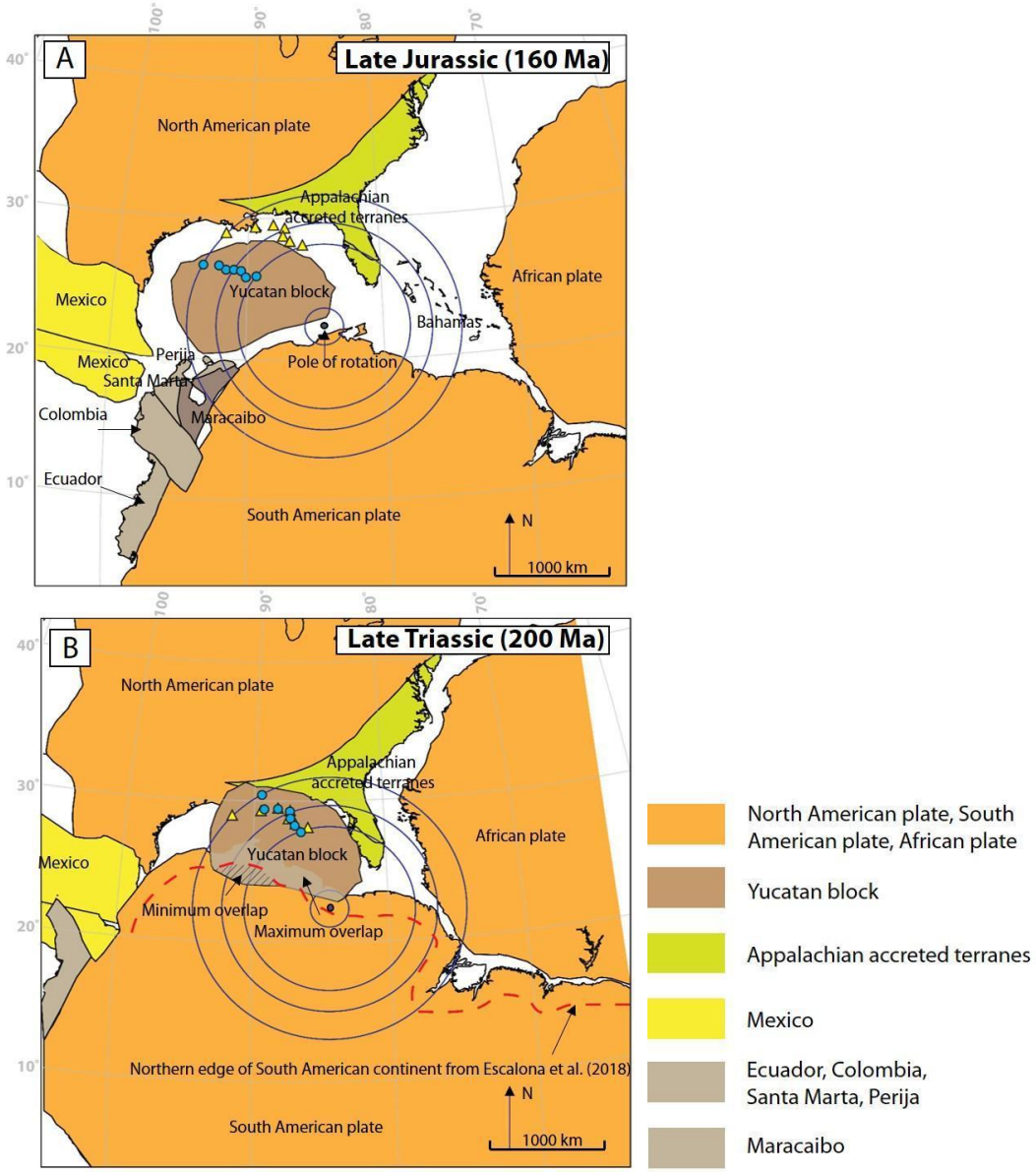
A
Late Jurassic (160 Ma)
North American plate
Appalachian
accreted terranes
African plate
Yucatan block
Mexico
Bahamas
Perija
Pole of rotation
Mexico
Santa Marta
Colombia
Maracaibo
Ecuador
South American plate
N
1000 km
B
Late Triassic (200 Ma)
North American plate
Appalachian
accreted terranes
African plate
Mexico
Yucatan block
Minimum overlap
Maximum overlap
Northern edge of South American continent from Escalona et al. (2018)
South American plate
N
1000 km
North American plate, South American plate, African plate
Yucatan block
Appalachian accreted terranes
Mexico
Ecuador, Colombia, Santa Marta, Perija
Maracaibo

This chapter tests two different scenarios for the displacement history of the Yucatan block. The first scenario uses the same pole as the seafloor spreading pole of Nguyen and Mann (2016) and continues rotating the Yucatan block clockwise until the early Triassic (200 Ma). The second scenario translates the Yucatan block in a northwestward direction to account for the thinned crust in that has been documented in offshore and onshore Texas and Louisiana (Eddy et al., 2014) (Figure 3.6).

This chapter uses both present-day coastline geometry and the restored, pre-late Cretaceous, South American plate boundary from Escalona et al. (2018), whose restoration of Cenozoic deformation determined the amount of crustal attenuation and calculated a restored northern margin of the South American plate that is 120 km inboard away from the present-day coastline. Other pre-rift plate reconstruction models of the South America region, such as Pindell et al. (2006), discussed the syn-rift Mesozoic extension of South American margin and its later Cenozoic post-rift deformation but did not provide a quantitative amount for these deformations.

The result of rotating the Yucatan block clockwise is shown in Figure 3.7B. The North American plate was kept fixed during this reconstruction and created a maximum overlap of 319,323 km^2 using the present-day South America coastline from Matthews et al. (2016) and a minimum overlap of 45,730 km^2 between the Yucatan and South American plates using the South American plate boundary that was restored 120 km southwards from Escalona et al. (2018) (Figure 3.7B). The result of restoring the Yucatan in the northwestward direction introduced a maximum overlap with the South American plate of 48,941 km^2, and the reconstruction of the northern margin of the South American continental edge from Escalona et al. (2018) results in no overlap (Figure 3.8) and therefore is favored as the best fit of the two tested scenarios.

Figure 3.8. A) Rigid reconstruction restoring the Yucatan block prior to seafloor spreading along the oceanic fracture zones using a pole in NW Cuba from Nguyen and Mann (2016) with plate motion overlay. B) Plate configuration achieved by NW translation of the Yucatan block. Yellow triangles are the RCOB on the US GOM. Blue circles are the RCOB on the Yucatan side. The brown area shows the overlap between the Yucatan block and the South America plate is 48,941 km^2. The red dashed line is the boundary for South America from 200 Ma-152 Ma, according to Escalona et al. (2018). White lines connect the RCOBs with the same strike in the US GOM. Dark red lines connect the RCOBs with the same strike in the Mexico GOM.

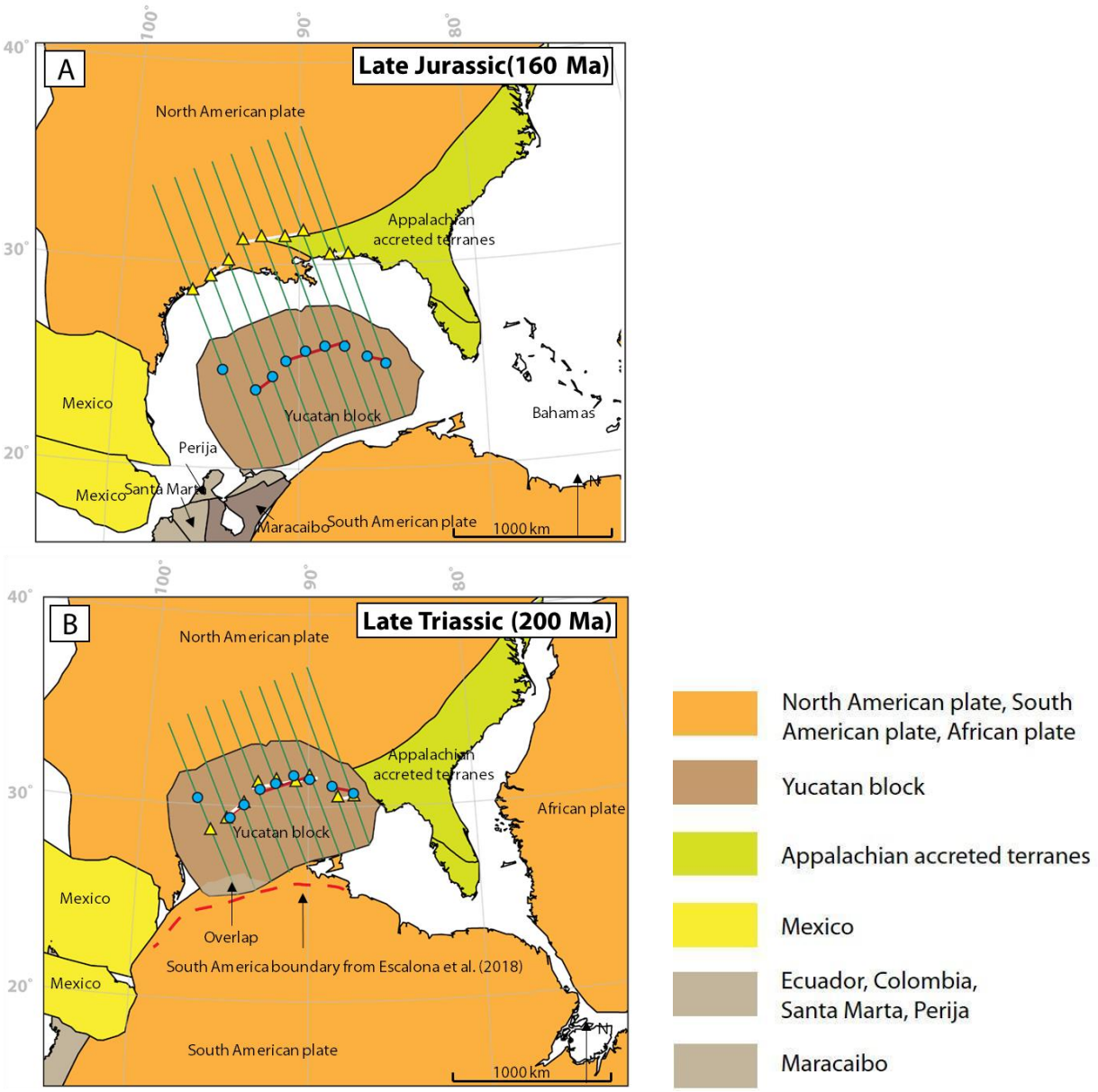
A
Late Jurassic(160 Ma)
North American plate
Appalachian
accreted terranes
Mexico
Yucatan block
Bahamas
Perija
Mexico
Santa Marta
Maracaibo
South American plate
1000 km
B
Late Triassic (200 Ma)
North American plate
Appalachian
accreted terranes
African plate
Yucatan block
Mexico
Overlap
South America boundary from Escalona et al. (2018)
Mexico
South American plate
1000 km
North American plate, South American plate, African plate
Yucatan block
Appalachian accreted terranes
Mexico
Ecuador, Colombia, Santa Marta, Perija
Maracaibo

3.5 Discussion

3.5.1 Underplating in the northeastern GOM inferred from reconstruction

The GUMBO profile 3 in the northeastern GOM shows high-velocity zones (7.2 km/s) in the lower crust in the interval between 70 km and 270 km on the modeled cross section (Eddy et al., 2014; Figure 3.9B). This high-velocity zone in the lower crust zone is interpreted to represent syn-rift magmatic underplating of a mafic/gabbroic layer near the Moho during the Late Triassic-Early Jurassic onset of rifting in the northeastern GOM (Eddy et al., 2014; Liu et al., 2019). It is necessary to remove these magmatic additions to the crust prior to the full-fit reconstruction. The area of the rifted margin would be decreased after subtracting the underplated material and therefore, the distance that is required to restore the COB back to the RCOB location would be increased if it is assumed that the original volume of continental crust is conserved.

Figure 3.9. Illustration of the full-fit reconstruction by a northwestward motion of the Yucatan block after taking into account the magmatic underplating in the areas of the eastern GOM. A) Location of the GUMBO 3 profile in the northeastern GOM. B) Structure along the GUMBO 3 profile in the northeastern GOM from Eddy et al. (2014). The high-velocity zone outlined by the green dash line in the lower crust is likely the result of crustal underplating. C) The RCOB misfit distance was reduced by 39% after subtracting the effect of underplated crustal materials. The orange triangle shows the new RCOB for the US margin of the GOM. The red dashed line is the boundary for South America from 200 Ma-152 Ma according to plate reconstructions by Escalona et al. (2018).

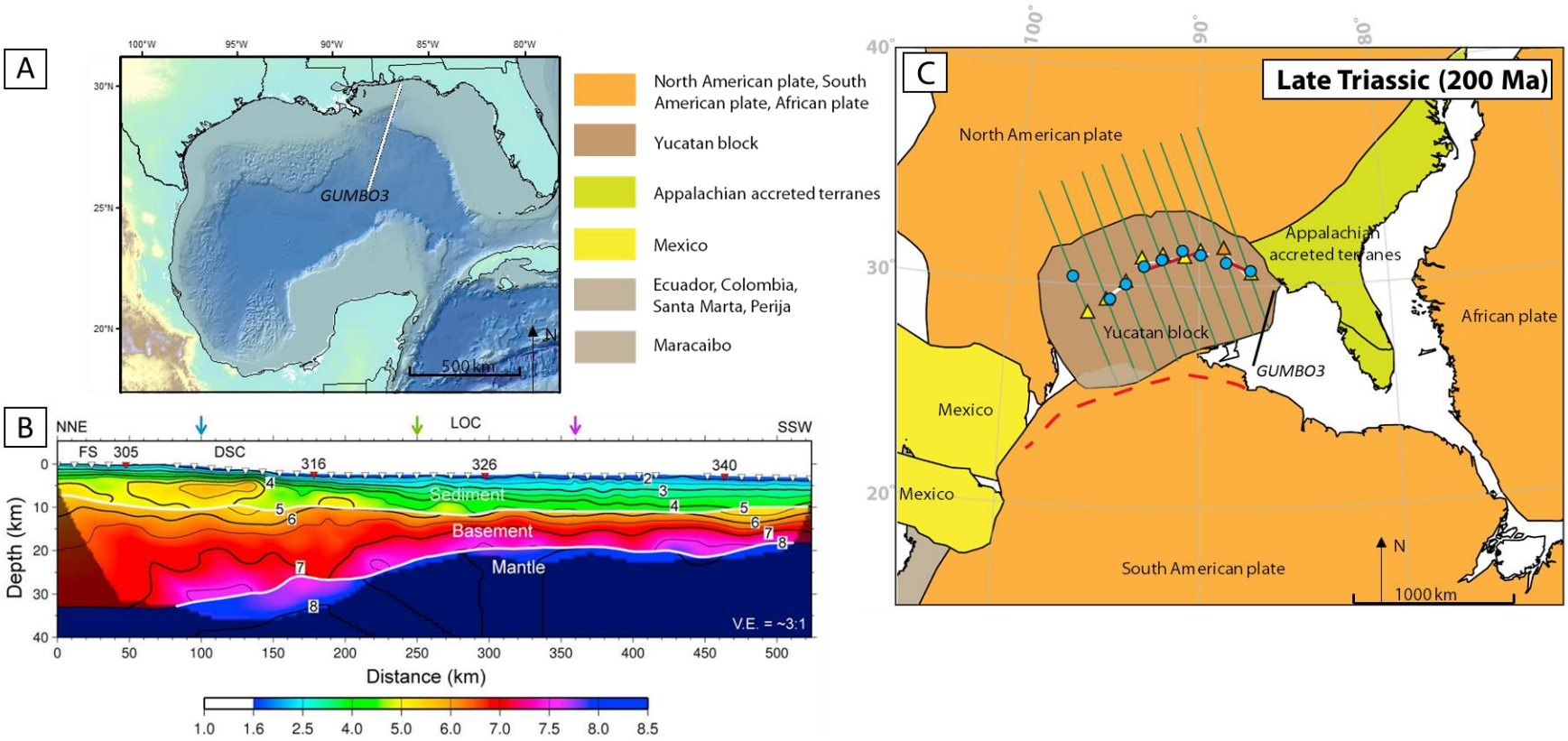
A
100°W
95°W
90°W
85°W
80°W
30°N
25°N
20°N
GUMBO3
500 km
N
North American plate, South American plate, African plate
Yucatan block
Appalachian accreted terranes
Mexico
Ecuador, Colombia, Santa Marta, Perija
Maracaibo
B
NNE
LOC
SSW
FS
305
DSC
316
326
340
Sediment
Basement
Mantle
V.E. = ~3:1
Depth (km)
Distance (km)
1.0
1.6
2.5
4.0
5.0
6.0
7.0
7.5
8.0
8.5
C
Late Triassic (200 Ma)
North American plate
Appalachian accreted terranes
Yucatan block
GUMBO3
African plate
Mexico
Mexico
South American plate
N
1000 km

To the southeast of the GUMBO profile 3, the high velocity lower crust zone that is greater than 7.2 km/s was also observed along GUMBO profile 4 and was previously interpreted to be the result of increased magmatic input during rifting (Christeson et al., 2014). The extracted profiles from the 3D crustal model do not coincide with the GUMBO 4 profile location; therefore, the area of underplated crust from the GUMBO 4 profile was not used in this study. The underplating area was estimated and integrated into the palinspastic reconstruction and reduced the misfit between the RCOB by 39 km (Figure 3.9C). Eddy et al. (2014) inferred the presence of an abnormally hot geotherm along the GUMBO 3 profile and suggested that the mantle underwent higher than normal temperatures during rifting in the northeastern GOM.

The elevated mantle temperatures inferred from CAMP-aged volcanics also exist in the South Georgia rift basin and Suwannee terrane of Florida during the onset of continental rifting (McBride, 1991; Heatherington and Mueller, 2003; Heffner et al., 2012; Eddy et al., 2014). Alternatively, Bird et al. (2005) suggested a mantle plume occurred at ~ 160 Ma in the central GOM, which could have provided an alternative source for the magmatic underplating.

3.5.2 Locating Euler Poles for the continental rifting stage of the GOM

Late Paleozoic arc volcanic rocks are in the Sabine uplift area of the northern GOM and pre-Mesozoic plutonic rocks are present in the Wiggins uplift area and been proposed by Marton and Buffler (1994) as evidence for a late Paleozoic rifting event in these areas. However, no magnetic isochrons and fracture zones can be identified for this proposed early rifting phase.

This study uses the RCOB locations as magnetic isochron picks as a method to restore the earliest inferred phase of rifting This assumption may or may not be valid, depending on whether the rift propagated along the margin, such as in the Jurassic opening of the Atlantic Ocean (e.g.,

Vink, 1982) or was synchronous along the entire margin. In addition, limited well data is available from the rift zone to gain a good understanding of the timing and duration of the early phase rifting. Therefore, the location of this Euler pole and reconstruction is an approximation of the pre-rift kinematics.

Figure 3.9A shows the computed Euler pole locations based on the methods of Hellinger (1981) and Bird et al. (2007) and using my definition of the conjugate segments. The westernmost pair of RCOBs has a larger misfit and for this reason, my study excludes it for the pole calculation using the method from Hellinger (1981). Because the method of Hellinger (1981) used great circle arcs to fit the segmentation of the target line, the rest of the RCOBs from this study were grouped into three segments based on their orientation (Figure 3.8). The results of the two methods are very similar to each other with both predicted pole locations in the center of Africa. These pole locations are similar to the pole location of Klitgord et al. (1984) who originally proposed that the early GOM opening was associated with the breakup of the Pangea.

The pole for the non-rigid reconstruction from this study using the method by Hellinger (1981) is located at 8.86°N, 27.8°W - with a rotation angle of ~6.4° (Figure 3.10). The pole using the method by Bird et al. (2007) is at 11.11°N, 20.6°W - with a rotation angle of ~12° (Figure 3.9). An uncertainty ellipse was calculated for each of the two methods (Figure 3.10A).

Figure 3.10. Full-fit reconstruction pole locations based on the method by Hellinger (1981) and Bird et al. (2007) that are marked as red and green stars, respectively. The red ellipse represents the uncertainty of the pole position using the method of Hellinger (1981) and the green ellipse represents uncertainty pole position using the method of Bird et al. (2007).

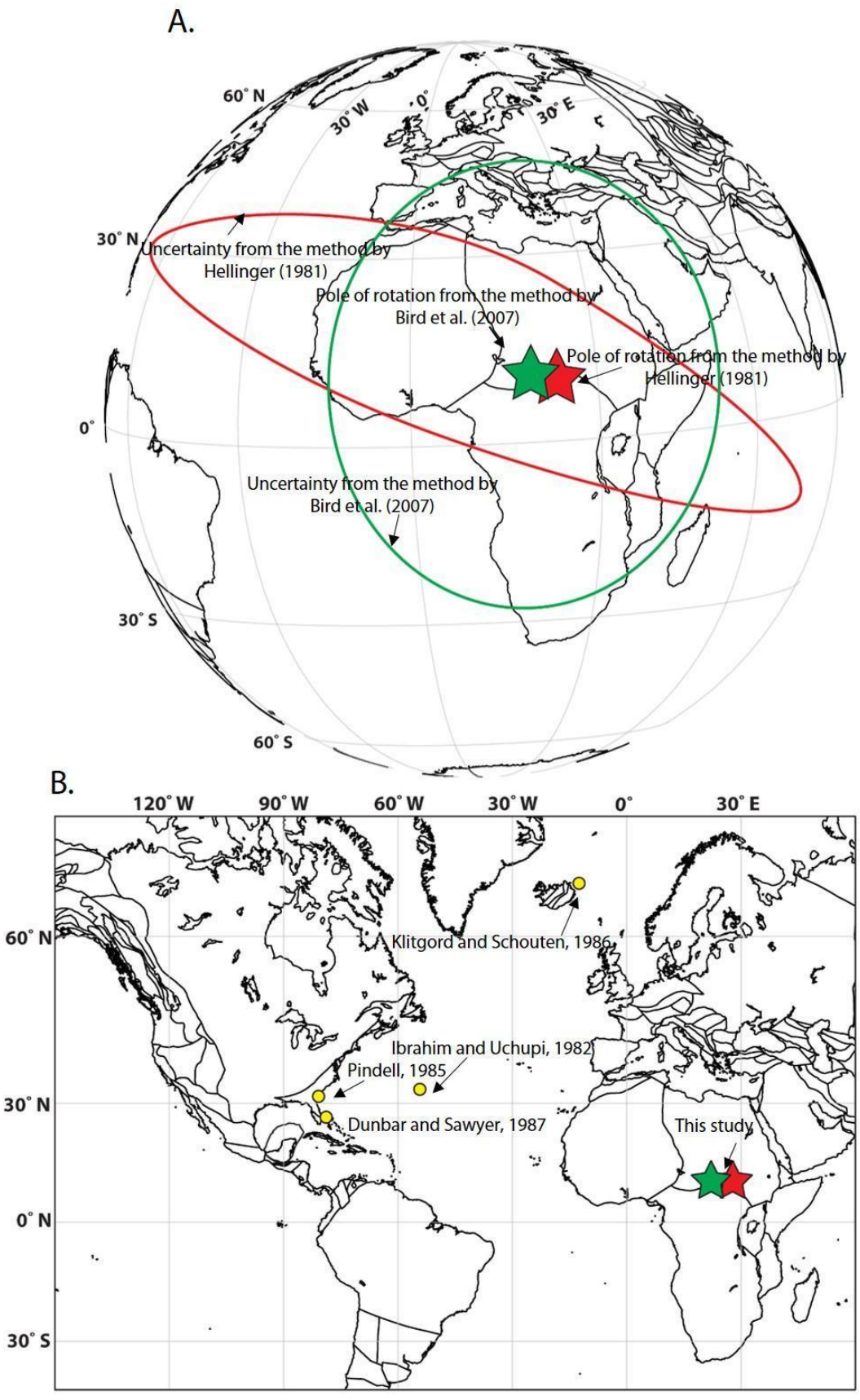
A.
60° N
30° W
0°
30° E
30° N
Uncertainty from the method by Hellinger (1981)
Pole of rotation from the method by Bird et al. (2007)
Pole of rotation from the method by Hellinger (1981)
0°
Uncertainty from the method by Bird et al. (2007)
30° S
60° S
B.
120° W
90° W
60° W
30° W
0°
30° E
60° N
Klitgord and Schouten, 1986
Ibrahim and Uchupi, 1982
Pindell, 1985
30° N
Dunbar and Sawyer, 1987
This study
0° N
30° S

The method of Hellinger (1981) results in a larger uncertainty in the longitude (small circle direction) and the method by Bird et al. (2007) results in a larger uncertainty in the latitude (great circle direction). Comparison of Euler poles for the continental rifting stage with previously published non-rigid pole locations is shown in Figure 3.10B. The previously proposed poles were located in the regions near the Atlantic Ocean. Large uncertainties for the non-rigid pole are caused by only nine pairs of RCOBs that were calculated in the model with a lack of additional constraints on the location of the RCOBs. The error estimates include the inherent bias in the data distribution and the subjective choice of the appropriate conjugate segments of the RCOBs, which was assumed as ±5 km.

The calculated pole location from this study differs from previous studies due to different assumptions and constraints. Here is a summary or how my results compare with the GOM reconstructions by previous workers: 1) Dunbar and Sawyer (1987) computed an optimal Euler pole using the distribution of oceanic crust by Ibrahim and Uchupi (1982) with a pole location at 33° N, 55°W (Figure 3.10B). In this case, the COB used during the reconstruction significantly differs from what I used in this study. The COB from Ibrahim and Uchupi (1982) extends onshore in the north-central GOM and bends to the west near the Middle Ground Arch in offshore Florida. 2) Pindell (1985) rotated the Yucatan block by 43 degrees counterclockwise away from the Texas-Louisiana margin around a pole located in northern Florida at 29.74 N°, 80.36° W. Instead of an NW-SE movement of the Yucatan block, Pindell (1985) translated the Yucatan along several proposed transform faults that offset the Florida Strait Block in the eastern GOM to achieve the fit. 3) Dunbar and Sawyer (1987) first integrated the amount of rotation accomplished through crustal extension in a more north-south direction and seafloor spreading and calculated the Euler

pole of the opening at 25°N, 79°W. 4) Klitgord and Schouten (1986) suggested the GOM basin opened in the same direction and about the same Euler pole as the central Atlantic basin at 66.95°N, 12.02°W. Their reconstruction of the GOM assumed the transform faults from the Central Atlantic Ocean extending into the GOM.

In summary, the location of these various poles from previous workers varies for two reasons: 1) the location of the COB varies between these models, and 2) the early stage opening direction varies between the models. As discussed in section 3.4.1, the COB used in this study is from crustal thickness that is based on the GUMBO refraction experiment (Van Avendonk et al., 2015; Eddy et al., 2018). The northwestward translation of the Yucatan is inferred from the thinned continental crust that is observed from the crustal thickness map in Figure 3.4B.

3.6 Conclusions

This chapter has utilized the 3D gravity inversion method to calculate the crustal thickness for the Greater GOM region. This chapter has estimated the extent of stretched continental crust and calculated the pre-rift location along the conjugate margins of the GOM. This chapter performed a full-fit plate reconstruction by using palinspastic restoration. The Euler pole was derived from fitting the RCOB locations and compared this reconstruction to those from previous workers.

Based on the crustal thickness distribution result from 3D gravity inversion, the crustal province was divided into four domains: 1) **full-thickness continental crust** with crustal thickness greater than 36 km and it is beyond the Marathon-Ouachita fold belt; 2) **thick transitional continental crust** varying in thickness from 20-36 km beneath the coastal plains that border the

GOM; 3) **thin transitional continental crust** from 10-20 km near the coast of the GOM, and 4) **oceanic crust** in the central GOM that is less than 10 km in thickness.

The restoration and the full-fit reconstruction support the presence of rift-related, magmatic underplating in the northeastern GOM. The initial NW-SE continental rift started at ~200 Ma resulted in the thinning of the crust by the formation of an extensive graben system that continued until the Late Jurassic (160 Ma) when the oceanic crust began to form in the center of the basin.

3.7 Bibliography

Antoine, J., Ewing, J., 1963. Seismic refraction measurements on the margins of the Gulf of Mexico. J. Geophys. Res. 68, 1975–1995.

Antoine, J.W., Harding, J.L., 1965. Structure beneath continental shelf, northeastern Gulf of Mexico. Am. Assoc. Pet. Geol. Bull. 49, 157–171.

Bai, Y., Wu, S., Liu, Z., Müller, R.D., Williams, S.E., Zahirovic, S., Dong, D., 2015. Full-fit reconstruction of the South China Sea conjugate margins. Tectonophysics 661, 121–135.

Bajgain, S.K., 2011. Gravity and magnetic modeling of basement beneath Alabama Gulf Coastal Plain. Unpublished MS thesis, Auburn University. 101 p.

Bayley, R.W., Muehlberger, W.R., 1968. Basement rock map of the United States: exclusive of Alaska and Hawaii.

Bird, D.E., Burke, K., Hall, S.A., Casey, J.F., 2005. Gulf of Mexico tectonic history: Hotspot tracks, crustal boundaries, and early salt distribution. Am. Assoc. Pet. Geol. Bull. 89, 311–328.

Bird, D.E., Hall, S.A., Burke, K., Casey, J.F., Sawyer, D.S., 2007. Early Central Atlantic Ocean seafloor spreading history. Geosphere, v3,282-298.

Blakely R., 1995. Potential theory in gravity and magnetic applications. Cambridge University Press.

Braile, L.W., 1989. Crustal structure of the continental interior, in Geophysical framework of the continental United States, L.C. Pakiser and W.D. Mooney, (Editors), Geol. Soc. Am. Memoir 172, 285-315.

Christensen, N. I., Mooney, W. D., 1995. Seismic velocity structure and composition of the continental crust: A global view, Journal of Geophysical Research, v. 100, p. 9761-9788.

Christeson, G.L., van Avendonk, H.J.A., Norton, I.O., Snedden, J.W., Eddy, D.R., Karner, G.D., Johnson, C.A., 2014. Deep crustal structure in the eastern Gulf of Mexico. J. Geophys. Res. Solid Earth 119, 6782–6801.

Chulick, G.S., Mooney, W.D., 2002. Seismic structure of the crust and uppermost mantle of North America and adjacent oceanic basins: A synthesis, Bulletin of the Seismological Society of America, Vols. 92, No. 6, 2478-2492.

Cordell, L., 1973. Gravity analysis using an exponential density-depth function-San Jacinto graben, California: Geophysics v. 38, no. 4, 684-690.

Cram, Irah, 1961. A Crustal structure refraction survey in South Texas. Geophysics XXVI, 560–573.

Del Castillo G, L., 1974. Marine geophysics along the Gulf of Mexico and the Yucatan Peninsula coastal area in Mexico. Phys. Earth Planet. Inter. 9, 227–247.

Dooley, T., Jackson, M., Hudec, M., 2013. Coeval extension and shortening above and below salt canopies on an uplifted, continental margin: Application to the northern Gulf of Mexico.

Dunbar, J.A., Sawyer, D.S., 1987. Implications of continental crust extension for plate reconstruction: An example from the Gulf of Mexico. Tectonics 6, 739–755.

Ebeniro, J.O., Nakamura, Y., Sawyer, D.S., O'Brien Jr., P., 1988. Sedimentary and crustal structure of the northwestern Gulf of Mexico. J. Geophys. Res. 93, 9075–9092.

Ebeniro, J.O., O'Brien, W.P., Shaub, F.J., 1986. Crustal structure of the South Florida Platform, eastern Gulf of Mexico: An ocean-bottom seismograph refraction study. Mar. Geophys. Res. 8, 363–382.

Eddy, D.R., Avendonk, H.J.A. Van, Christeson, G.L., Norton, I.O., Karner, G.D., Johnson, C.A., Snedden, J.W., 2014. Deep crustal structure of the northeastern Gulf of Mexico: Implications for rift evolution and seafloor spreading. Journal of Geophysical Research : Solid Earth 1–21.

Escalona, A., Norton, I., Lawver, L.A., Gahagan, L., 2018. Quantitative plate tectonic reconstructions of the Caribbean region, from Jurassic to present, AAPG Memoir 123, in press.

Ewing, J., Antoine, J., Ewing, M., 1960. Geophysical measurements in the western Caribbean Sea and in the Gulf of Mexico. J. Geophys. Res. 65, 4087–4126.

Frederick, B.C., Blum, M.D., Snedden, J.W., and Fillon, R.H., 2020. Early Mesozoic synrift Eagle Mills Formation and coeval siliciclastic sources, sinks, and sediment routing, northern Gulf of Mexico basin, GSA Bulletin, 1-20.

Hales, A.L., Helsley, C.E., Nation, J.B., 1970. Crustal structure study on Gulf Coast of Texas. Am. Assoc. Pet. Geol. Bull. 54, 2040–2057.

Hatcher, R.D., 2002. Alleghanian (Appalachian) orogeny, a product of zipper tectonics: Rotational transpressive continent-continent collision and closing of ancient oceans along irregular margins. Spec. Pap. Geol. Soc. Am. 364, 199–208.

Heatherington, A. L., Mueller, P. A., 2003. Mesozoic igneous activity in the Suwannee terrane, southeastern USA: Petrogenesis and Gondwanan affinities, Gondwana Res., 6(2), 296–311.

Heffner, D. M., J. H. Knapp, O. M. Akintunde, Knapp, C. C., 2012. Preserved extent of Jurassic flood basalt in the South Georgia Rift: A new interpretation of the J Horizon, Geology, 40(2), 167–170.

Hellinger, S. J., 1981. The uncertainties of finite rotations in plate tectonics, J. Geophys. Res., 86, 9312–9318.

Hudec, M.R., Norton, I.O., Jackson, M.P.A., Peel, F.J., 2013. Jurassic evolution of the Gulf of Mexico salt basin. Am. Assoc. Pet. Geol. Bull. 97, 1683–1710.

Hudec, M.R., Norton, I.O., 2019. Upper Jurassic structure and evolution of the Yucatan and Campeche subbasins, southern Gulf of Mexico, AAPG Bulletin, v.103, No. 5, 1133-1151.

Ibrahim, A.K., Uchupi, E., 1982. Continental oceanic crustal transition in the Gulf Coast Geosyncline, in Watkins, J.S. and Drake, C.L. (eds), *Studies in continental margin geology: AAPG Memoir 34*, 155-165.

Ibrahim, A.K., Latham, J.C.G., Buffler, R.T., 1981. Crustal structure in Gulf of Mexico from OBS refraction and multichannel reflection data. Am. Assoc. Pet. Geol. Bull. 65, 1207–1229.

Kim, S.D., Nagihara, S., Nakamura, Y., 2000. P- and S-wave velocity structures of the Sigsbee Abyssal Plain of the Gulf of Mexico from ocean bottom seismometer data, Gulf Coast Association of Geological Societies Transactions, v.50, 475–484.

Klitgord, K.D., Schouten, H., 1986. Plate kinematics of the central Atlantic, in *The Geology of North America*, GSA Decade of North American Geology, 351–378.

Kneller, E.A., Johnson, C.A., 2011. Plate kinematics of the Gulf of Mexico based on integrated observations from the Central and South Atlantic. Gulf Coast Assoc. Geol. Soc. Trans. 61, 283–299.

Laske, G., Masters, G., Ma, Z., Pasyanos, M. E., 2013. Update on CRUST 1.0: a 1-degree global model of earth's crust: European Geosciences Union, 2658.

Liu, M., Filina, I., Mann, P., 2019. Crustal structure of Mesozoic rifting in the northeastern Gulf of Mexico from the integration of seismic and potential fields data. Interpretation, (July), 1–33.

Marton, G., Buffler, R.T., 1994. Jurassic reconstruction of the Gulf of Mexico Basin. Int. Geol. Rev. 36, 545–586.

Marzen, R.E., Shillington, D.J., Lizarralde, D., Knapp, J.H., Heffner, D.M., Davis, J.K., Harder, S.H., 2020. Limited and localized magmatism in the Central Atlantic Magmatic province. Nature communications.

Matthews, K. J., Maloney, K. T., Zahirovic, S., Williams, S. E., Seton, M., Müller, R. D., 2016. Global plate boundary evolution and kinematics since the Late Paleozoic: Global and Planetary Change.

McBride, J. H., 1991. Constraints on the structure and tectonic development of the early Mesozoic South Georgia Rift, southeastern United States; seismic reflection data processing and interpretation, Tectonics, 10(5), 1065–1083.

Minguez, D.E., Hensel, G., Johnson, E.A.E., 2020. A fresh look at Gulf of Mexico Tectonics: Testing rotations and breakup mechanisms from the perspective of seismically constrained potential fields modelling and plate kinematics. Interpretation.

Mooney, W.D., Laske, G., Masters, T.G., 1998. CRUST 5.1: A global crustal model at 5° × 5°. J. Geophys. Res. 103, 727–747.

Nakamura, Y., Sawyer, D.S., Shaub, F.J., 1988. Deep crustal structure of the northwestern Gulf of Mexico. Gulf Coast Association of Geological Societies Transactions Volume XXXVIII.

Nance, R.D., Gutiérrez-Alonso, G., Keppie, J.D., Linnemann, U., Murphy, J.B., Quesada, C., Strachan, R.A., Woodcock, N.H., 2012. A brief history of the Rheic Ocean. Geosci. Front. 3, 125–135.

Netto, A., Dunbar, J., 2019. 3-D constrained inversion of gravimetric data to map the tectonic terranes of southeastern Laurentia using simulated annealing. Earth Planet. Sci. Lett. 513, 12–19.

Nguyen, L.C., Mann, P., 2016. Gravity and magnetic constraints on the Jurassic opening of the oceanic Gulf of Mexico and the location and tectonic history of the Western Main transform fault along the eastern continental margin of Mexico. *Interpretation* 4, SC23–SC33.

Parker R., 1973. The rapid calculation of potential anomalies. Geophys J Int 31(4):447–455

Pavlis, N.K., Holmes, S.A., Kenyon, S.C., Factor, J.K., 2012. The development and evaluation of the Earth Gravitational Model 2008 (EGM2008). Journal of Geophysical Research, Solid Earth, 117, 1-38.

Pindell, J., Kennan, L., Stanek, K.P., Maresch, M.V., and Draper, G., 2006. Foundations of Gulf of Mexico and Caribbean evolution: eight controversies resolved. Geologica Acta, Vol. 4, 303-341.

Pindell, J., Miranda C, E., Cerón, A., Hernandez, L., 2016. Aeromagnetic map constrains Jurassic-Early Cretaceous synrift, break up, and rotational seafloor spreading history in the Gulf

of Mexico, in Lowery, C.M., Snedden, J.W., Rosen, N.C. (Eds.), *Mesozoic of the Gulf Rim and Beyond: New Progress in Science and Exploration of the Gulf of Mexico Basin*. SEPM Society for Sedimentary Geology, 123–153.

Pindell, J.L., 1985. Alleghenian reconstruction and subsequent evolution of the Gulf of Mexico, Bahamas, and proto-Caribbean. Tectonics 4, 1–39.

Rowan, M.G., 2014. Passive-margin salt basins: hyperextension, evaporite deposition, and salt tectonics. Basin Res. 26, 154–182.

Salvador, A., 1987. Late Triassic-Jurassic paleogeography and origin of Gulf of Mexico basin. Am. Assoc. Pet. Geol. Bull. 71, 419–451.

Sandwell, D.T., Muller, R.D., Smith, W.H.F., Garcia, E., Francis, R., 2014. New global marine gravity model from CryoSat-2 and Jason-1 reveals buried tectonic structure. Science. 346, 65–67.

Sawyer, D.S., Buffler, R.T., Pilger, R., 1991. Crust and mantle of the Gulf of Mexico basin, in Salvador, A. (Ed.), The Gulf of Mexico Basin. Geological Society of America, Boulder, Colorado, 53–72.

Singleton, R.F., 2016. Gravity and magnetic modeling of basement beneath the Appalachian Plateau, Valley and Ridge, and Piedmont provinces, Alabama. Unpublished MS thesis, Auburn University. 83 p.

Steier, A., Mann, P., 2019. Late Mesozoic gravity sliding and Oxfordian hydrocarbon reservoir potential of the northern Yucatan margin. Mar. Pet. Geol. 103, 681–701.

Straume, E. O., Gaina, C., Medvedev, S., Hochmuth, K. & Gohl, K., 2019. GlobSed: updated total sediment thickness in the world's oceans: Geochemistry, Geophysics, Geosystems, v. 20, 1756-1772.

Vink, G.E., 1982. Continental rifting and the implications for plate tectonic reconstructions, Journal of Geophysical Research, v. 87, No.B13, 10,677-10,688.

White, R. S., McKenzie, D., O'Nions, R. K., 1992. Oceanic crustal thickness from seismic measurements and rare earth element inversions, Journal of Geophysical Research, v. 97, p. 19683-19715.

Williams, S.E., Whittaker, J.M., Müller, R.D., 2011. Full-fit palinspastic reconstruction of the conjugate Australian-Antarctic margins. Tectonics 30, 1–21.

CHAPTER 4: POTENTIAL FIELDS AND SEISMIC STRATIGRAPHY OF THE MARGINAL RIFT SYSTEM ADJACENT TO LATE JURASSIC OCEANIC CRUST OF THE DEEP-WATER GULF OF MEXICO BASIN

4.1 Introduction

4.1.1. Previous work on the Mesozoic opening of the GOM

Previous workers in the Gulf of Mexico (GOM) have concluded from basin-wide compilations of refraction-based, crustal thickness data (Nguyen and Mann, 2016), mapping and modeling of marine satellite gravity data (Sandwell et al., 2014; Lin et al., 2019), and regional seismic stratigraphic interpretations (Marton and Buffler, 1994; Snedden et al., 2014) that the Mesozoic GOM basin formed during two distinct phases of Mesozoic rifting and oceanic crust formation (Figure 4.1).

Figure 4.1 a) Map of the Gulf of Mexico (GOM) showing its Jurassic marginal rift system (outlined in black) adjacent to late Jurassic oceanic crust in the central GOM with the continent-ocean boundary from Sandwell et al. (2014) shown as a thicker yellow line, oceanic spreading ridges and fracture zones from Lin et al. (2019) shown as thinner, yellow lines, and West Main Transform fault from Nguyen and Mann (2016) shown as a thinner, yellow dash line. Triassic-Early Jurassic Phase 1 normal faults and rifts are interpreted from potential fields data and are shown as the red lines and are crosscut by younger, normal faults of the GOM marginal rift system shown by the black lines. Pink areas are the Louann salt in the northern (US) GOM and the Campeche salt in the southern (Mexico) GOM with the thin, white line showing the updip limit of Jurassic salt from Rowan (2014). The area of the Mexican Ridges (outlined in blue) lacks salt deposition because it is underlain by the oceanic crust to the east and continental crust truncated to the West Main Transform fault to the west. b) Free-air gravity map (Sandwell et al., 2014) with previous refraction stations as compiled from Nguyen and Mann (2016) shown as white dots. Numbers in parentheses next to the refraction station are the refraction-based depths in kilometers to the top of the crystalline basement. The yellow line is the continent-ocean boundary (COB) as mapped by Sandwell et al. (2014) using satellite gravity. Orange polygon is the location of the southern seaward dipping reflectors (SDRs) from Liu et al. (2019).

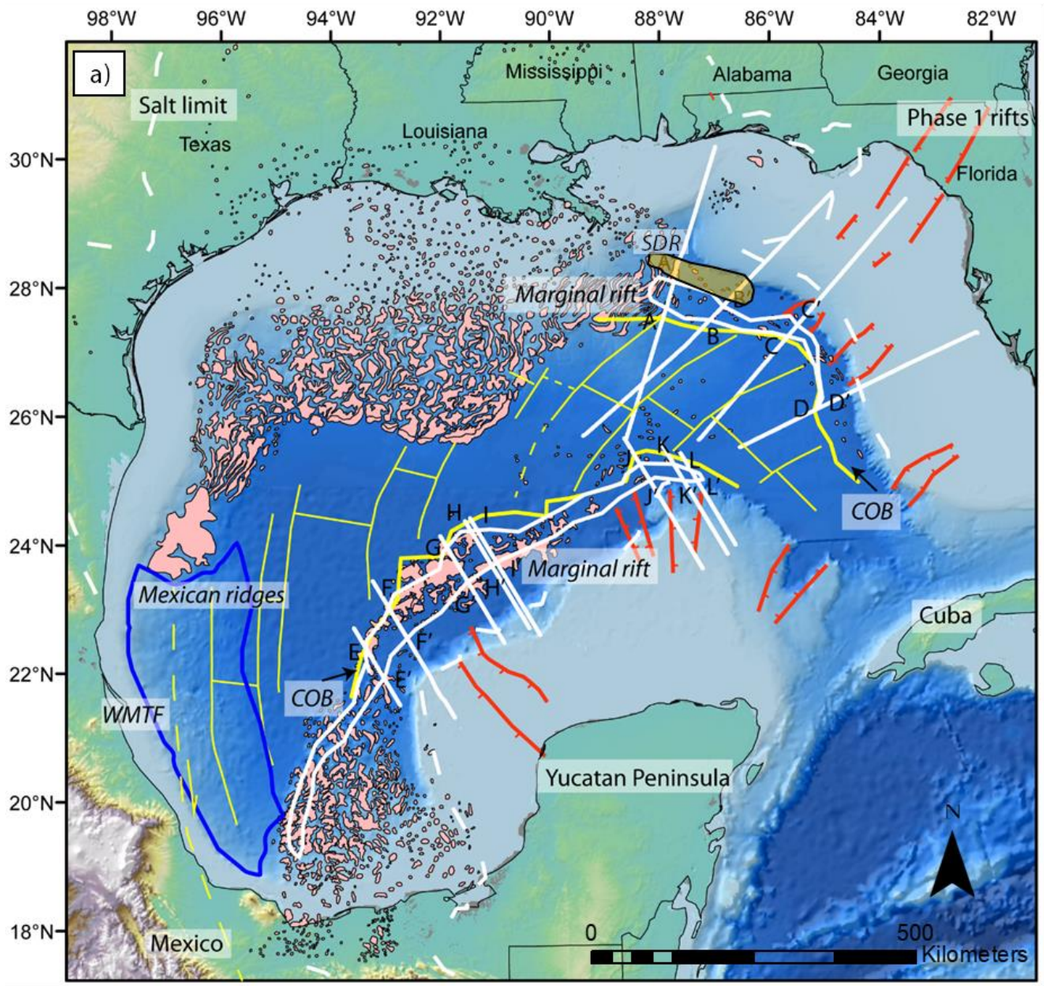
a)
Salt limit
Texas
Louisiana
Mississippi
Alabama
Georgia
Florida
Phase 1 rifts
SDR
Marginal rift
COB
Mexican ridges
WMTF
Cuba
Yucatan Peninsula
Mexico
98°W
96°W
94°W
92°W
90°W
88°W
86°W
84°W
82°W
30°N
28°N
26°N
24°N
22°N
20°N
18°N
0
500
Kilometers
N

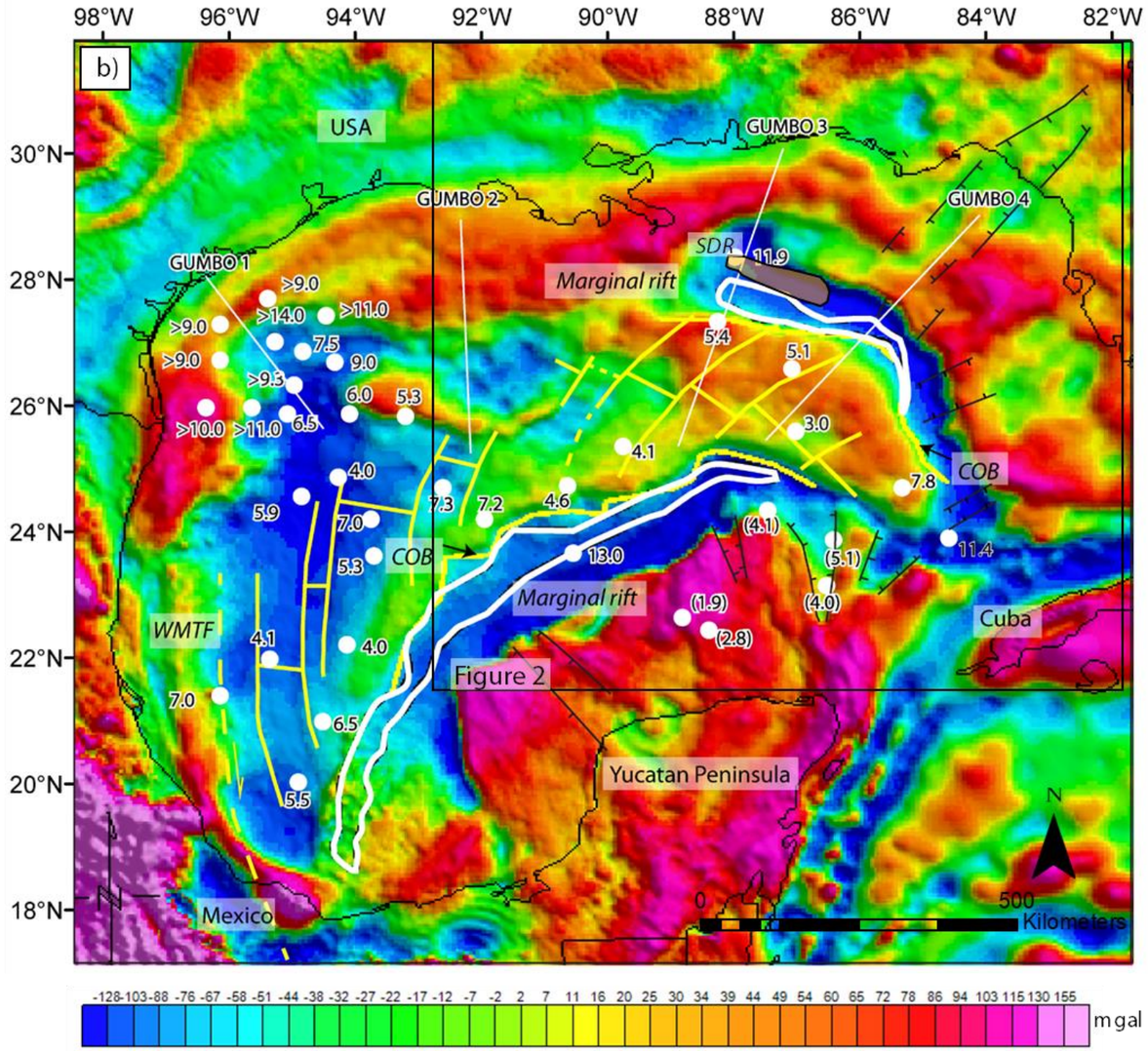
b)
USA
GUMBO 1
GUMBO 2
GUMBO 3
GUMBO 4
SDR
Marginal rift
COB
WMTF
Cuba
Yucatan Peninsula
Mexico
Figure 2
>9.0
>14.0
>11.0
7.5
9.0
>9.3
6.0
5.3
>10.0
>11.0
6.5
4.0
5.9
7.0
5.3
4.1
4.0
7.0
6.5
5.5
11.9
5.4
5.1
3.0
4.1
7.8
7.3
7.2
4.6
13.0
11.4
(4.1)
(5.1)
(1.9)
(4.0)
(2.8)
98°W
96°W
94°W
92°W
90°W
88°W
86°W
84°W
82°W
30°N
28°N
26°N
24°N
22°N
20°N
18°N
0
500
Kilometers
N
-128 -103 -88 -76 -67 -58 -51 -44 -38 -32 -27 -22 -17 -12 -7 -2 2 7 11 16 20 25 30 34 39 44 49 54 60 65 72 78 86 94 103 115 130 155
mgal

The first GOM opening phase (Phase 1) included late Triassic-northwest-southeast extension during the breakup of the supercontinent Pangea but this early opening phase did not lead to oceanic crust formation in the central GOM. Phase 1 rifting is characterized by northeast-trending rifts that are deeply buried and best known from studies of potential fields and deep drilling in the subsurface of the Florida Peninsula, Yucatan Platform, and Bahamas Platform (Erlich and Pindell, 2020) (Figure 4.1). These Phase 1 rifts are less known from the northern GOM and southeastern USA, where the rifts are buried by 10-15 km of sedimentary rocks and salt deposits (Eddy et al., 2014; Frederick et al., 2020). The gravity signal over some of these deeply-buried rifts includes both elongate gravity anomaly highs and lows. The magnetic signal over these Phase 1 rifts displays strong negative magnetic lows, and therefore it will require either deeply penetrative rifts up to tens of kms in thickness or intrusions within the rift (Smith and Lord, 1997).

Frederick et al. (2020) noted that there is little direct evidence for rift control on the Triassic Eagle Mills Formation in the northern GOM and that Triassic accommodation space was likely inherited from late Paleozoic orogenic events. These orogenic-related accommodation spaces were simply infilled by coarse-grained, Triassic continental sedimentation. In the previous Chapter 3, I noted the large area of thinned continental crust (10-36 km) that extends from the offshore northern GOM area to the Appalachian-Ouachita-Marathon Mountains and that can be reconstructed by a northwest-southeast-oriented, Phase 1 rift event to its pre-rift, orogenic thickness (36 km) (Figure 4.1). This reconstruction indicates that some of the large area of the northern GOM may be in fact be underlain by rifts that have not yet been identified.

In other areas of thinner, sedimentary cover in the southern and eastern GOM, rifts with northeast trends were identified that include a large rift along the northern margin of the Yucatan

Peninsula (Salvador, 1987) and several rifts in the subsurface of the Florida Peninsula and Bahamas Platform (Erlich and Pindell, 2021) (Figure 4.1). These rifts of inferred Late Triassic-Early Jurassic age appear to have formed coevally with better studied and dated rifts of this age that are exposed along the eastern margin of North America and on the Central Atlantic conjugate margins in northwest Africa (Olson, 1997; Withjack et al., 2013; Boote and Knapp, 2016). Klitgord and Schouten (1986) proposed that the GOM Phase 1 rifts formed about the same pole of rotation between North America and northwest Africa as these Central Atlantic rifts (cf. Chapter 4 for a discussion).

Triassic-early Jurassic phase 1 northwest-to-southeast rifting was followed by the deposition of a single, Louann-Campeche salt basin within the unfaulted sag basins that overlying these Phase 1 rifts. Although now separated into the US (Louann) and Mexican (Campeche) salt basins and with the salt horizons remobilized locally by both gravitational and sedimentary loading effects, this Louann-Campeche salt horizon forms a widespread, relatively short-lived (~11 Ma), and distinctive stratigraphic marker across a large area of the GOM. Estimates by previous workers for the age or Phase 1 rifting using various methods to range in age from Bajocian (170 Ma) to Oxfordian (159 Ma) (Marton and Buffler, 1994; Pulham et al., 2019; Pindell et al., 2021) (Figure 4.2).

Figure 4.2. Chronostratigraphic chart summarizing the lithology of the Yucatan platform and northeastern GOM. The Yucatan and northeastern GOM conjugate margins share similar stratigraphy during Phase 1 rifting (late Triassic-early Jurassic) and Phase 2 rifting (late Jurassic). By the early Cretaceous the two conjugate margins were separated by late Jurassic oceanic crust of the central GOM and the two rifted margins show different stratigraphic histories. The stratigraphic information used to create the chart was compiled from Lin et al. (2018), Hudec and Norton (2019), Steier and Mann (2019), and Kenning and Mann (2020).

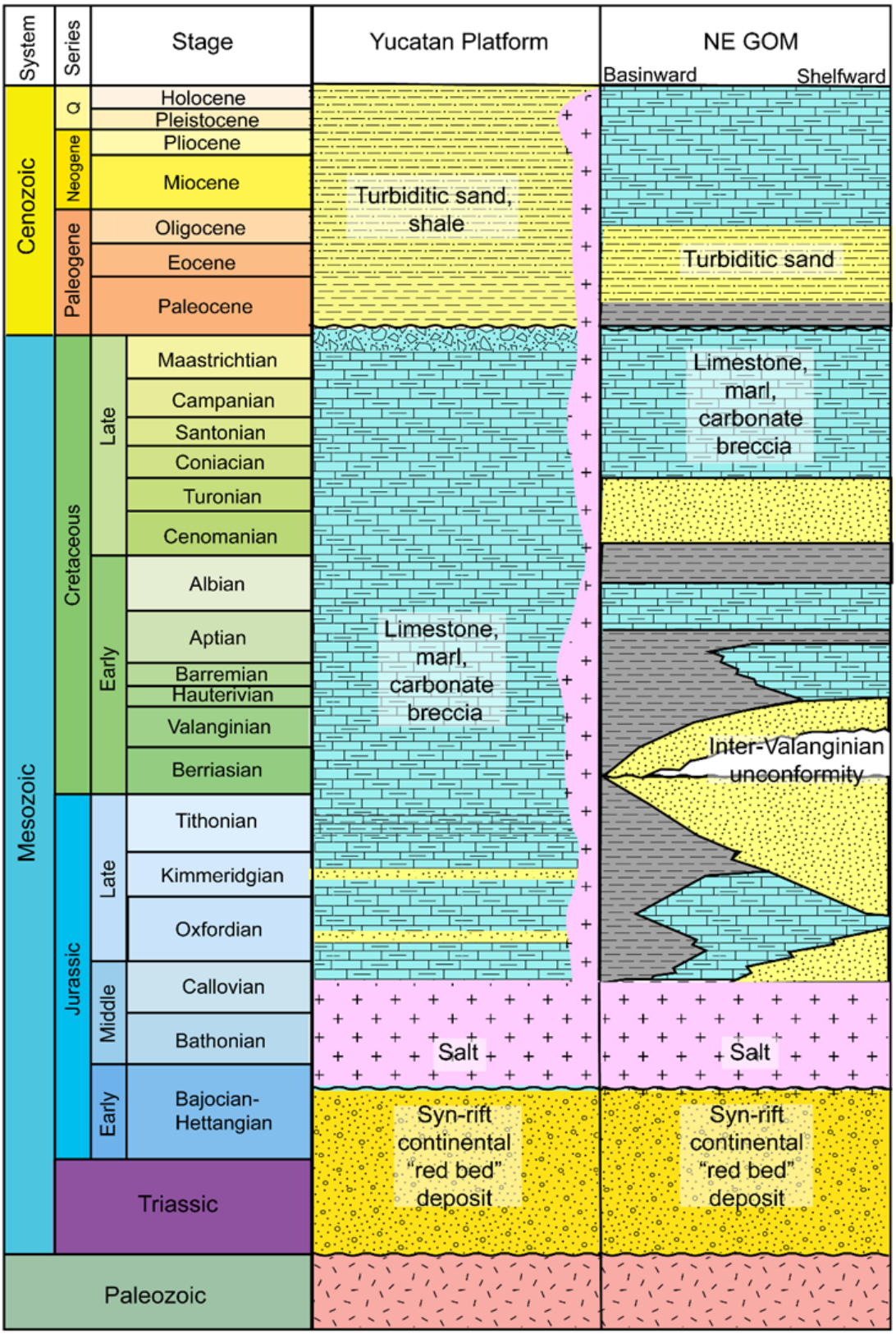
System
Series
Stage
Yucatan Platform
NE GOM
Basinward
Shelfward
Cenozoic
Q
Holocene
Pleistocene
Neogene
Pliocene
Miocene
Paleogene
Oligocene
Eocene
Paleocene
Turbiditic sand, shale
Turbiditic sand
Mesozoic
Cretaceous
Late
Maastrichtian
Campanian
Santonian
Coniacian
Turonian
Cenomanian
Limestone, marl, carbonate breccia
Early
Albian
Aptian
Barremian
Hauterivian
Valanginian
Berriasian
Limestone, marl, carbonate breccia
Inter-Valanginian unconformity
Jurassic
Late
Tithonian
Kimmeridgian
Oxfordian
Middle
Callovian
Bathonian
Salt
Salt
Early
Bajocian-Hettangian
Syn-rift continental "red bed" deposit
Syn-rift continental "red bed" deposit
Triassic
Paleozoic

This two-phase rift history and stratigraphic timing have been incorporated into recent tectonic models for the early opening of the GOM (Eddy et al., 2014; Nguyen and Mann, 2016; Erlich and Pindell, 2020) and are consistent with the regional variations based on 3D gravity inversion and reconstructions of the areas of thinned crustal thickness as described in Chapter 3 of this dissertation (Figure 4.1). A corollary of this two-phase rift model is that the older, northeast-trending Phase 1 rifts and their less faulted, overlying and salt-filled basin were crosscut by the second phase of more north-south rifting and late Jurassic-early Cretaceous seafloor spreading that accompanied a ~40 counterclockwise rotation of the Yucatan block (Marton and Buffler, 1994; Nguyen and Mann, 2016).

Previous workers have identified potential zones of these younger Phase 2 rifts in basement lows or "marginal rifts" or "outer marginal troughs" (Pindell et al., 2014) that are immediately adjacent to the area of late Jurassic oceanic crust that underlies the deep, central GOM (Hudec et al., 2013; Van Avendonk et al., 2015; Marton and Buffler, 2016; Liu et al., 2019; Rowan, 2020; Kenning and Mann, 2021) (Figure 4.3a, b). As there are no direct age controls on these Phase 2 rifts, Pindell et al. (2016) inferred that the youngest oceanic crust of the central GOM is Tithonian-Berriasian in age and that the oldest oceanic crust adjacent to the exhumed mantle and continental margin is Oxfordian-Tithonian in age (Figure 4.3b).

Figure 4.3. Previously proposed model adjacent to the COB. a) Model by Hudec et al. (2013) showing the location of the continent-ocean boundary in the northern GOM as a "step-up fault" that consists of a sloped inner (northern) ramp and an outer (southern) ramp with 1-4 km of total vertical, "step-up" relief between the two ramps as indicated at the three locations on the map that were studied by Hudec et al. (2013). The dashed blue line is the proposed location of the extinct Jurassic spreading ridge of Hudec et al. (2013). New proposed COB from Hudec (personal communication, 2021) as indicated by the dotted blue line. Salvador (1987) proposed a large, late Triassic-early Jurassic rift in the location shown as a blue rift in the northern Yucatan margin. Storey (2020) mapped the extent of two, contiguous Apalachicola rifts in the northeastern GOM along with the Elbow rift to the southeast. b) Model by Pindell et al. (2016) for exhumed mantle shown in pink and fringing the oceanic crust in the central GOM with their proposed COB shown as the green. Green line is COB from Pindell et al. (2016). Orange polygons in the northern GOM and Campeche are the magnetic anomaly highs from Pindell et al. (2016).

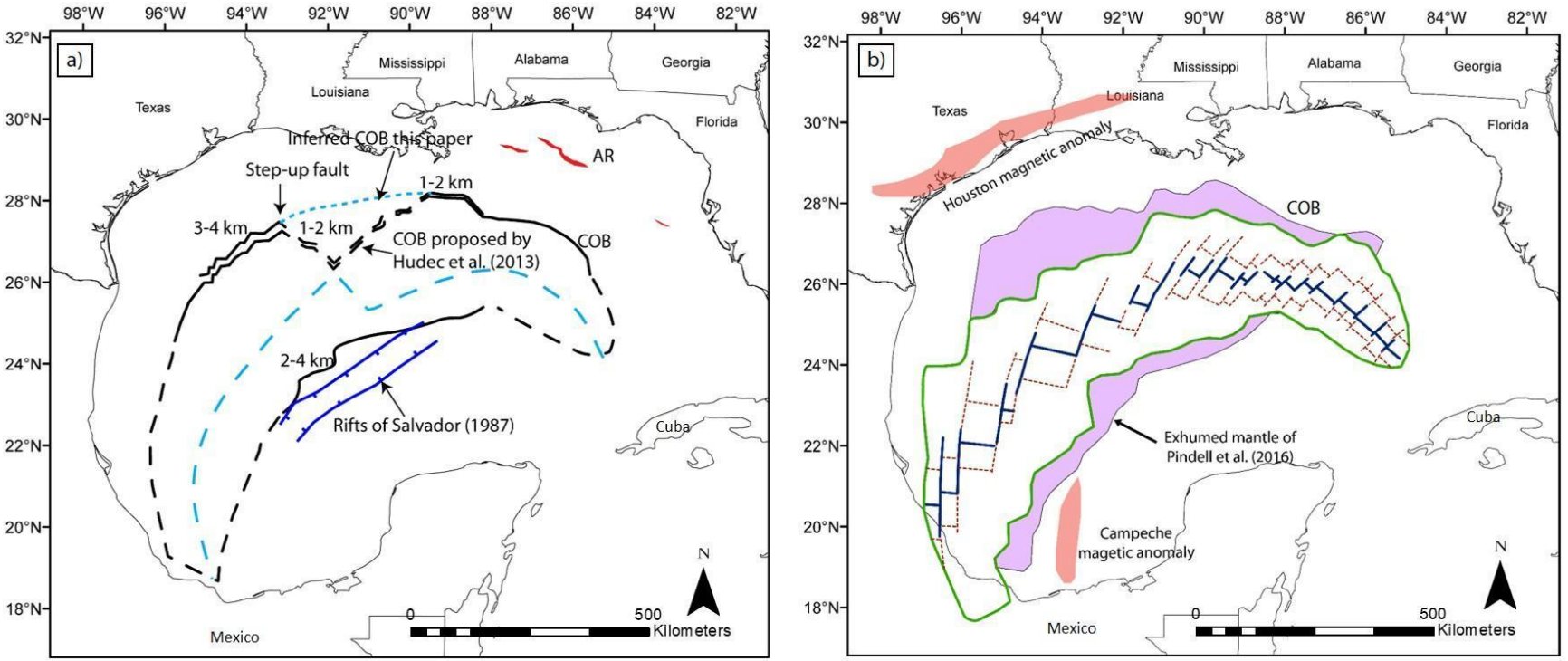
a)
Texas
Louisiana
Mississippi
Alabama
Georgia
Florida
Cuba
Mexico
Inferred COB this paper
Step-up fault
AR
1-2 km
3-4 km
1-2 km
COB proposed by
Hudec et al. (2013)
COB
2-4 km
Rifts of Salvador (1987)
98°W
96°W
94°W
92°W
90°W
88°W
86°W
84°W
82°W
32°N
30°N
28°N
26°N
24°N
22°N
20°N
18°N
N
0
500
Kilometers
b)
Texas
Louisiana
Mississippi
Alabama
Georgia
Florida
Cuba
Mexico
Houston magnetic anomaly
COB
Exhumed mantle of
Pindell et al. (2016)
Campeche
magetic anomaly
98°W
96°W
94°W
92°W
90°W
88°W
86°W
84°W
82°W
32°N
30°N
28°N
26°N
24°N
22°N
20°N
18°N
N
0
500
Kilometers

A key element of the marginal rift concept is that an outer basement high exists seaward of the rift to confine continental or marine sediments along this seaward edge of the rift; this same outer high would form the landward edge of the late Jurassic oceanic crust. In the western GOM, Hudec et al. (2013) observed a basement "step-up" feature or "inner ramp" and outer basement high and the continent-ocean boundary (COB) with up to 4 km topographic relief on the basement (Figure 4.3a). The simplified extinct spreading center and fracture zones were proposed prior to the improved spreading ridge location based on the Sandwell et al. (2014) marine gravity data shown in Figure 4.1b.

Hudec et al. (2013) proposed the triangular area known as the Walker Ridge to be a continental salient in the COB (Figure 4.3b). More recently, Hudec (personal communication, 2021) has stated that he no longer supports the Walker Ridge as a continental salient and instead proposes that the COB is located north of the Walker Ridge. Although the nomenclature for these features differs, the ramp structures proposed by Hudec et al. (2013) agree with my interpretation of the marginal rift and its outer high adjacent to the COB.

Marton and Buffler (2016) interpreted a seismic profile located in offshore Florida with a distinct marginal rift present along the profile and Gomez et al. (2018) also identified a prominent rift along the offshore Yucatan margin. The magnetic map in Figure 4.4 and discussed in detail by Lin (2018) supports the idea that older, north-east-trending, Phase 1 rifts were cross-cut by younger, more east-west-oriented rifts formed during Phase 2 GOM opening. This Phase 2 marginal rift displays an elongate magnetic low consistent with an elongate, sediment-filled rift basin. The truncated Phase 1 rifts on the Yucatan Peninsula exhibit a 40º counterclockwise rotation relative to the truncated rifts in Florida (Lin, 2018; Figure 4.4).

Figure 4.4. a) Total magnetic intensity map modified from Lin (2018) showing northeast-trending Phase 1 rifts that interpreted from gravity and magnetic data and more east-west marginal rift system as white lines and strike-slip faults as black dashed lines from Lin (2018). Note that Phase 1 rifts trend at a high angle and are crosscut by the younger marginal rift system formed as the Yucatan block rotated counterclockwise relative to Florida and oceanic crust formed in the central GOM. Key to abbreviations for tectonic features: AE = Apalachicola Embayment; MGA = Middle Ground Arch; NTE = North Tampa Embayment; STE = South Tampa Embayment; SrA = Sarasota Arch; SFB = South Florida Basin; SB = Suwanee Basin; CE = Celestun Embayment; RLA = Rio Lagartos Arch; NRLB = North Rio Lagartos Basin; SRLB = South Rio Lagartos Basin; CA = Chiquila Arch; CB = Chiquila Basin. b) Oxfordian (160 Ma) reconstruction of the GOM after removing the oceanic crust through a clockwise rotation of the Yucatan block. Phase 1 rifts show a good fit between the Yucatan and Florida conjugate margins except for minor strike-slip displacements on the northwest-striking faults in the Florida area that are shown as dashed black lines.

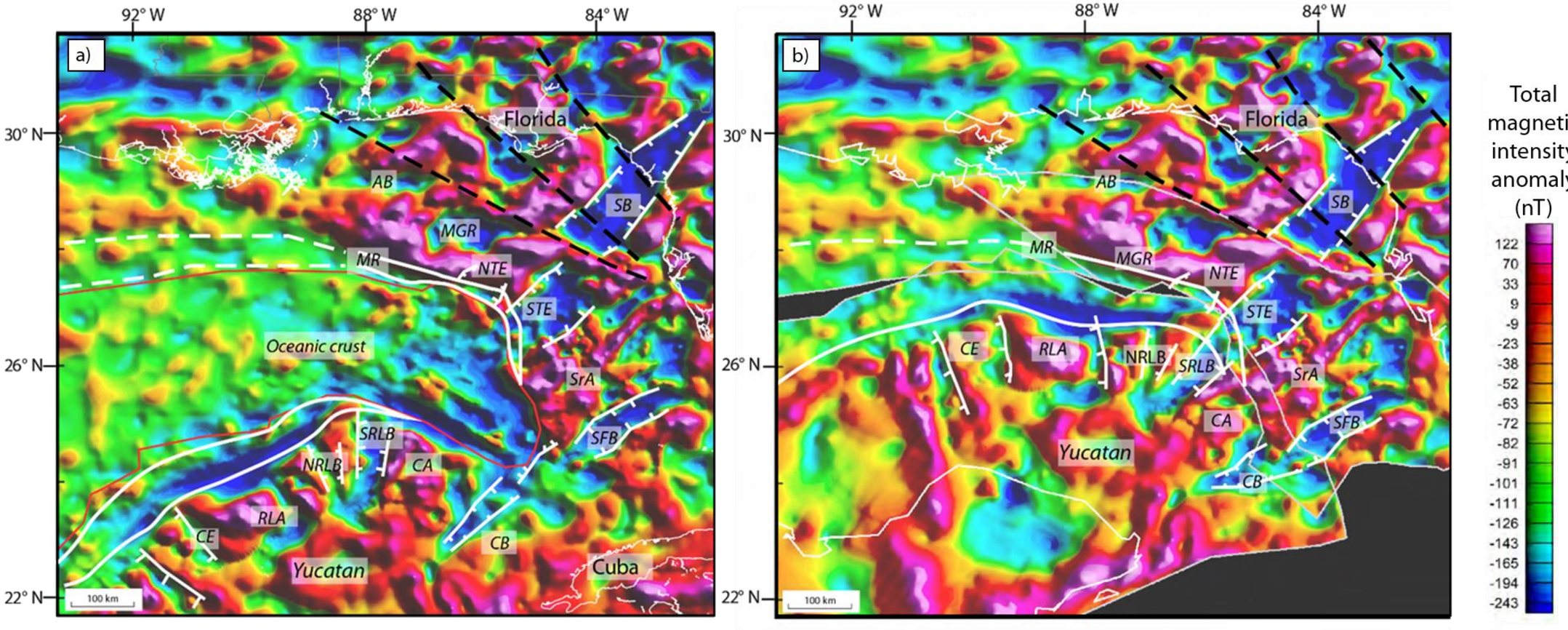
a)
b)
92° W
88° W
84° W
30° N
26° N
22° N
Florida
AB
SB
MGR
MR
NTE
STE
SrA
SFB
Oceanic crust
SRLB
NRLB
CA
RLA
CE
CB
Yucatan
Cuba
100 km
Total magnetic intensity anomaly (nT)
122
70
33
9
-9
-23
-38
-52
-63
-72
-82
-91
-101
-111
-126
-143
-165
-194
-243

4.1.2. Objectives and significance of this chapter

While most previous workers agree on the existence of individual marginal rifts in specific areas around the oceanic crust of the GOM, there has been no previous systematic effort to show that this marginal rift system forms a continuous and coeval rift system that coincides in age with the Middle to Late Jurassic Phase 2 of GOM opening as proposed in the two-phase GOM opening model summarized above (Figure 4.3a).

In this chapter, I integrate gravity and magnetic data with 12 regional and deep-penetrating seismic reflection profiles from the margins of the US and Mexican GOM to show that the GOM marginal rift system does, in fact, form a continuous, clastic-sediment-filled rift system over hundreds of km along both the northern US GOM and the northern margin of the Yucatan Peninsula in the Mexican GOM (Figure 4.3a). I use the seismic data itself combined with gravity modeling to show that the marginal rift system is: 1) variable in its width and sedimentary thickness; 2) uniformly expressed as an elongate gravity and magnetic low; 3) bounded by low-angle normal faults (LANFs); and 4) overlies thinned, continental crust interpreted from gravity modeling and from seismic refraction and reflection data.

In addition to the description of the structural and stratigraphic characteristics and variability of the marginal rift system, I use 2D gravity modeling to test three different models for the crustal structure and tectonic origin of the marginal rift. In chapter 3, I described a regional crustal thickness map from 3D gravity inversion and proposed that the circum-GOM marginal rift system formed during Phase 2 rifting above “necked” or thinned continental crust (Peron-Pinvindic et al., 2019) and immediately prior to the formation of a late Jurassic spreading ridge. Supporting evidence for this crustal structure and rift history includes GUMBO refraction profile

1 that crosses the COB in the northwestern GOM and shows a decrease in the P wave velocity from 6 to 5 km/s and was interpreted by Van Avendonk et al. (2015) as middle Jurassic rift sedimentary fill that extends across the 30 km width of the rift.

Pindell et al. (2014), Curry et al. (2018), and Minguez et al. (2020) proposed an alternative model for the formation of the marginal rift zone as a zone of serpentinized, sub-continental mantle that was exhumed in the late Jurassic (167-159 Ma) as the footwall of a low-angle and landward-dipping detachment fault (Figure 4.5b). Pindell et al. (2014) proposed that the elongate, basement low was a mantle collapse feature that was partially filled with sediments, but was not a rift in the normal sense of continental crust of the same composition being extended and infilled with sediments (Figure 4.5b). Minguez et al. (2020) modeled the exhumed mantle in the EGOM with potential fields and noted that the exhumed mantle area formed an elongate, gravity and magnetic anomaly high that was consistent with the underlying material being serpentinized mantle. I concluded in Chapter 3 that the marginal rift is expressed as an elongate, gravity and magnetic low (Figure 4.1b).

Figure 4.5. Summary of three contrasting crustal models proposed for the crustal structure of the continent-ocean transition that surrounds the late Jurassic oceanic crust of the central GOM. a) My model based on my seismic stratigraphic and gravity study of the circum-GOM marginal rift system proposes a semi-continuous, sediment-filled, circum-GOM rift system that overlies a necked zone of continental crust that was stretched immediately prior to the formation of late Jurassic oceanic crust. The circum-GOM marginal rift is bounded on both sides by uplifted blocks of continental crust. b) Exhumed mantle model for the circum-GOM rifted margins as proposed by Pindell et al. (2014), Curry et al. (2018), and Minguez et al. (2020). In this model, the mantle is exhumed to the surface along a deeply penetrating, landward-dipping detachment fault. c) Exhumed lower continental crust model proposed by Filina and Hartford (2021) for the circum-GOM area in which the lower continental crust is exhumed to the surface along a landward-dipping detachment fault. In my model in (a), I propose that this landward-dipping surface represents the Moho at the base of a necked zone of continental crust. The inverted triangle indicates the location of the COB.

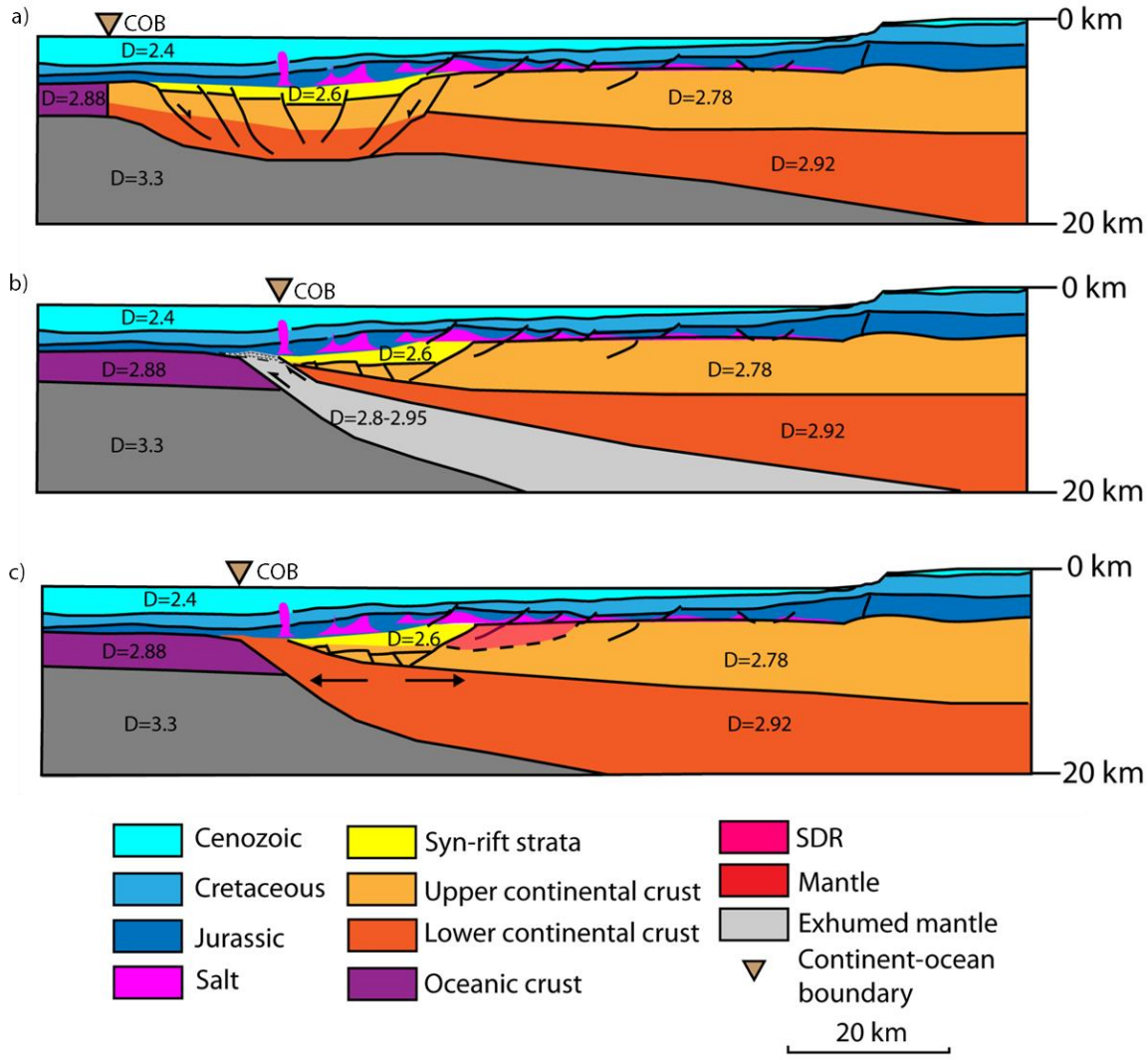
a)
COB
D=2.4
D=2.88
D=2.6
D=2.78
D=3.3
D=2.92
0 km
20 km
b)
COB
D=2.4
D=2.6
D=2.88
D=2.78
D=2.8-2.95
D=3.3
D=2.92
0 km
20 km
c)
COB
D=2.4
D=2.6
D=2.88
D=2.78
D=3.3
D=2.92
0 km
20 km
Cenozoic
Cretaceous
Jurassic
Salt
Syn-rift strata
Upper continental crust
Lower continental crust
Oceanic crust
SDR
Mantle
Exhumed mantle
Continent-ocean boundary
20 km

Filina and Hartford (2021) proposed a third crustal model and tectonic origin for the marginal rift area of the Yucatan margin that consisted of the lower continental crust being exhumed along a low-angle, landward-dipping detachment fault (Figure 4.5c). They also mapped a 430 km long and 50 km wide belt of seaward-dipping reflectors (SDRs) adjacent to the marginal rift that previous workers and myself in Chapter 3 of this dissertation had interpreted as a sedimentary infill (Hudec and Norton, 2019). In this chapter, I describe in detail the main components of the GOM marginal rift system and then address these widely differing tectonic models for its crustal structure and tectonic origin.

4.2 Dataset and methodology

4.2.1 Seismic datasets used in this study

This study uses twelve (12) profiles from two 2D seismic reflection grids of pre-stack depth-migrated (PSDM) data located in offshore Florida and the northern Yucatan margin. Four seismic profiles from the DeepEast survey are located in the NE GOM and perpendicular to the shelf. The DeepEast survey was acquired by TGS in 2007 with a shot interval of 37.5 m and a two-way time record length of 13-14 seconds.

Eight (8) seismic profiles from the Yucatan Regional seismic grid are located in north of the Yucatan platform with most lines running perpendicular to the margin. This dataset was acquired by Spectrum in 2015 with a 15-second record length and were pre-stack depth migrated. Age interpretations of top Jurassic and top Cretaceous were correlated from the northeastern GOM based on Liu et al. (2019) and Lin et al. (2019). Age interpretations of the Cenozoic section are from Kenning and Mann (2021).

4.2.2 Gravity and magnetic datasets used in this study

Free-air gravity data from Sandwell et al. (2014) were used to develop integrated, 2D gravity models. The reported accuracy of this global dataset is approximately 2 mgal (Sandwell et al., 2014).

The magnetic data shown in Figure 4.4 is modified from Lin et al. (2019), who compiled the magnetic data from shipboard data collected during the Deep East and Yucatan Regional seismic surveys and from the compilation by Finn et al. (2001) that was completed for the The Decade of North American Geology (DNAG) study. Magnetic data from these same sources were used to better constrain the locations of the marginal rifts adjacent to the area of the late Jurassic oceanic crust.

4.2.3 Two-dimensional forward gravity models

All gravity modeling was performed using Seequent's GM-SYS with the calculations of gravity response based on the method of Talwani et al. (1959) that approximates a two-dimensional body with a polygon. Using this method, the vertical and horizontal components of the gravitational attraction related to this polygon can be calculated at any given point. This method assumes an xz system of coordinates, with z being positive downwards, Θ being the angle between the positive x-axis to the positive z-axis. Given these parameters, the vertical component of gravitational attraction V and the horizontal H can be expressed as

$$V = 2G_{\rho} \sum_{i=1}^{n} Zi$$

and

$$H = 2G_{\rho} \sum_{i=1}^{n} Xi$$

GM-SYS profile modeling uses a 2D, flat Earth model for the gravity calculation with each structural unit or block extending to infinity in the direction perpendicular to the profile. In this section, I describe two, integrated, 2D subsurface models along two regional seismic profiles that were acquired at right angles to the northern Yucatan margin (Figure 4.6).

The models extend from the shelf to the edge of oceanic crust in the central, deep-water area of the GOM and are constrained by seismic reflection profiles for the underlying subsurface block geometries. One nearby seismic refraction station from Ibrahim et al. (1981) constrains the depth to basement. The gravity response was calculated based on the density value of each layer and compared with the observed gravity data extracted along the modeled profile. The subsurface layers were then adjusted to fit the constraints from the seismic reflection lines and refraction data.

4.2.4 Method used for structural restoring the Yucatan rifted margin

To better demonstrate the structural evolution of the study area, one, dip-directed cross-section perpendicular to the Yucatan platform and modified from Kenning and Mann (2020) was sequentially restored using Midland Valley MOVE software. The top horizon of each stratigraphic unit was backstripped, each sedimentary interval was decompacted using the method of Sclater and Christie (1980), and movements along major faults were restored.

Sedimentary properties, such as lithology and porosity, were assigned based on the stratigraphic column shown in Figure 4.2 that was compiled from Lin et al. (2018), Hudec and Norton (2019), Steier and Mann (2019), and Kenning and Mann (2020). After the rock type is assigned, the porosity values are calculated based on default porosity for each rock type and a depth coefficient that defines the rate at which porosity exponentially decreases with depth for a defined rock type as described by Sclater and Christie (1980). The geometries of salt bodies were

allowed to be modified passively through time by the surrounding sediments during the structural restoration in order to account for salt movement in and out of the plane of the section.

4.3 Results of this study

4.3.1 2-dimensional gravity modeling of the marginal rift

2-D gravity model 1. The seismic profile used to constrain model 1 covers the necking, distal, outer, and oceanic domains (Figure 4.6a) using the rifted, continental margin terminology as proposed by Peron-Pinvidic et al. (2013) based on their modeling and observational studies of other South and Central Atlantic rifted margins. 2D gravity model 1 is a 278-km-long, northwest to southeast-trending, regional cross-section across the western Yucatan rifted margin (Figure 4.6c).

Figure 4.6 a) Interpreted seismic profile along the section F-F' on the western Yucatan margin illustrating the crustal domains and structures and used to constrain a 2D gravity model along this same line. b) Interpreted seismic profile along the section K-K' on the eastern Yucatan platform, illustrating the crustal domains and structure. Note the decrease in width and depth of the marginal rift from the western line F-F' shown in (a) and the eastern line K-K' shown in (b). The eastward decrease in width of the marginal rift is also shown on the maps in Figures 4.1a and 1b and is linked to the eastern area being the narrower rift tip of the GOM rift system. Sedimentary nature and age information for the rift fill of the western Yucatan margin is compiled from Kenning and Mann (2020) based on their study of the Yucatan margin. c) 2D gravity model 1 across the western Yucatan Platform along the seismic reflection line shown in Figure 4.6a. Black dots are the observed free-air gravity data and the black line is the calculated gravity response from the 2D gravity model. The observed and calculated signals are tied across the oceanic domain. d) 2D gravity model 2 across the eastern Yucatan margin and along the seismic reflection line shown in Figure 4.6b. One nearby seismic refraction station from Ibrahim et al. (1981) was projected onto this profile and was used for constraining the depth to the top basement. e) Location map showing the location of the two seismic profiles.

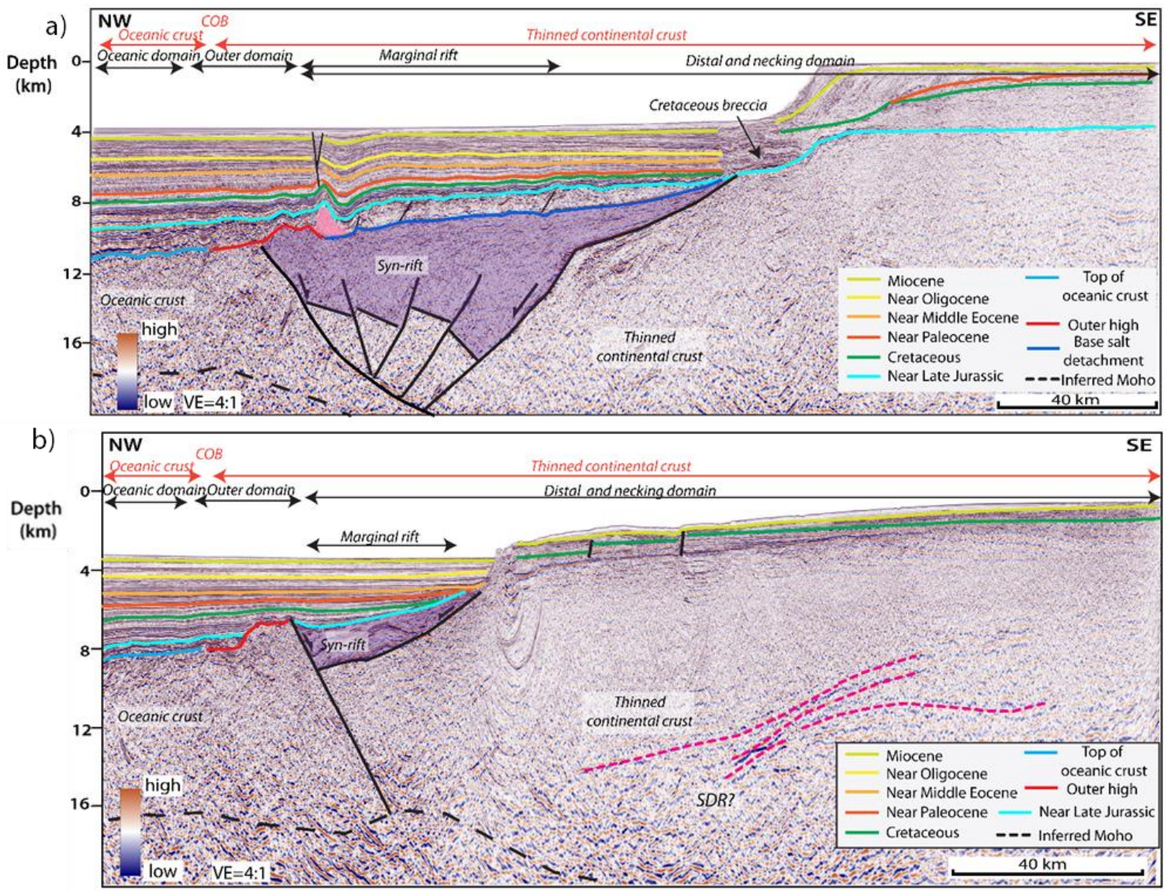
a)
NW
SE
COB
Oceanic crust
Thinned continental crust
Oceanic domain
Outer domain
Marginal rift
Distal and necking domain
Cretaceous breccia
Depth (km)
Syn-rift
Oceanic crust
high
low
VE=4:1
Thinned continental crust
Miocene
Near Oligocene
Near Middle Eocene
Near Paleocene
Cretaceous
Near Late Jurassic
Top of oceanic crust
Outer high
Base salt detachment
Inferred Moho
40 km
b)
NW
SE
COB
Oceanic crust
Thinned continental crust
Oceanic domain
Outer domain
Distal and necking domain
Marginal rift
Depth (km)
Syn-rift
Oceanic crust
Thinned continental crust
SDR?
high
low
VE=4:1
Miocene
Near Oligocene
Near Middle Eocene
Near Paleocene
Cretaceous
Top of oceanic crust
Outer high
Near Late Jurassic
Inferred Moho
40 km
e)
Fig. 4.6b
Fig. 4.6a
94°W
92°W
90°W
88°W
86°W
26°N
24°N
22°N
20°N
18°N
c)
50.00
0.00
-50.00
=Observed, _ =Calculated
Upper oceanic crust D=2.8
Water D=1.03
Sediments D=2.4
Marginal rift D=2.6
Upper continental crust D=2.78
Lower oceanic crust D=2.95
Lower continental crust D=2.92
Depth (km)
60 km
Mantle D=3.3
VE=2:1
d)
60.00
0.00
-60.00
-120.00
=Observed, _ =Calculated
Upper oceanic crust D=2.8
Water D=1.03
Sediments D=2.4
Marginal rift D=2.6
Upper continental crust D=2.78
Depth (km)
Lower oceanic crust D=2.95
Lower continental crust D=2.92
50 km
Mantle D=3.3
VE=2:1

Gravity model 1 consists of eight subsurface blocks and shows good agreement between the calculated and measured gravity anomalies. The density inputs of the upper continental crust, lower continental crust, oceanic layer 2, oceanic layer 3, and upper mantle used for these models were assigned 2.78 g/cc, 2.92 g/cc, 2.8 g/cc, 2.95 g/cc, and 3.3 g/cc, respectively (Figure 4.6a). The density of the upper continental crust is constrained by density measurements from DSDP well 538A (Buffler et al., 1984). The density of the lower continental crust is assumed to be 2.92 g/cc following Carlson and Herrick (1990). The oceanic crust density and mantle density values used are consistent with the previous model by Filina and Hartford (2021). These density values are also consistent with previously published 2D gravity models on the conjugate margin in offshore Florida from Liu et al. (2019). Since there is no density information for the 8-km-thick sedimentary section, the density of sediments above the crystalline basement was modeled as 2.4 g/cc, which is the average value used for previous models for the conjugate margin of offshore Florida by Liu et al. (2019).

The model shows the presence of the marginal rift located 38 km to 108 km along the profile as shown in Figure 4.6a. The rift has an average width of 70 km and an average thickness of 8 km. This segment of marginal rift system corresponds to an elongate gravity anomaly low and is modeled with a density of 2.6 g/cc, which is a lower value compared to the surrounding crustal material and suggests a volcaniclastic composition of the sedimentary fill. The thinned continental crustal thickness varies from 8 km to 30 km along the profile (Figure 4.6c).

2D gravity model 2. Model 2 is perpendicular to the eastern Yucatan rifted margin and includes the necking, distal, outer, and oceanic domains in the rifted, continental margin terminology of Peron-Pinvidic et al. (2013) (Figure 4.6e). Model 2 is a 220-km-long, northwest-

southeast-oriented regional cross-section on the eastern Yucatan platform (Figure 4.6d). This model consists of eight subsurface blocks that show good agreement between the calculated gravity measured gravity anomaly. The density values used for model 2 are consistent the values used for gravity model 1 as shown in Figure 4.6d.

This segment of the marginal rift is located between 40 km and 70 km along the modeled transect and exhibits a width of 30 km and a sedimentary thickness of 2 km. The 4.1 km depth of the basement was constrained from a nearby seismic refraction station by Ibrahim et al. (1981).

4.3.2 Marginal rift system of the GOM formed along low-angle normal faults

On non-volcanic rifted margins, the marginal rift commonly overlies the necking domain, where the crustal thickness can abruptly thin from 30 km to less than 10 km along generally low-angle normal faults with dips less than 30º that bound full- and half-grabens (Peron-Pinvindic and Mantaschal, 2009). Morley (2014) defines a LANF as a normal fault with a dip range of <35° at the time of rift initiation. In this section, I describe marginal rifts bounded by low-angle normal faults (LANFs) along the conjugate margins of the northeastern GOM and the Yucatan GOM.

The age interpretations of both rifted margins are provided in the same published papers as those listed above for the Yucatan margin. I compare the differing beta factors of these two conjugate margins that vary from 2-6 based on the 3D crustal model described in Chapter 3 of this dissertation.

Description of the marginal rift zone of the northeastern GOM. Transect A-A' is a regional dip line that is oriented northeast-southwest across the northeastern GOM (Figure 4.7a and 4.7b). Post-salt structures are deformed by vertical salt diapirism likely related to sediment loading and gravity sliding along an inclined basal salt detachment. Several Callovian salt rollers were

interpreted along the detachment in the up-dip direction and have been described in greater detail by Steier and Mann (2019).

The sedimentary thickness in the marginal rift locally exceeds 10 km along transect A-A'. Under the basal salt detachment, the marginal rift is located near the seaward limit of thinned continental crust and is 70 km wide, contains an average thickness of 6 km of sedimentary fill, and exhibits an outer basement high of presumed continental crust that is directly adjacent to oldest, late Jurassic oceanic crust in the central GOM (Figure 4.7d).

Figure 4.7 Seismic examples on the NE GOM. a) Uninterpreted seismic reflection line A-A' across the marginal rift in the northeastern GOM. b) Interpreted seismic reflection line A-A'. The purple color shows the inferred sedimentary fill with the marginal rift and the pink color are Jurassic salt deposits that were mainly concentrated in the post-marginal rift sag basin. The true dip angles of the landward-dipping and low-angle normal fault range from 10°-20°. c) Uninterpreted seismic example of the marginal rift along B-B' in the northeastern GOM. d) Interpreted seismic reflection line B-B'. An outer basement high is present and is inferred to be continental crust based on the 2D gravity model. e) Location map showing the location of the two seismic profiles. f) Previously published 2D gravity model along the full-length profile of the A-A' from Liu et al. (2019) and modeled the density of the sedimentary fill of the marginal rift as 2.6 g/cc. g) Previously published 2D gravity model along the full-length profile of the B-B' from Liu et al. (2019).

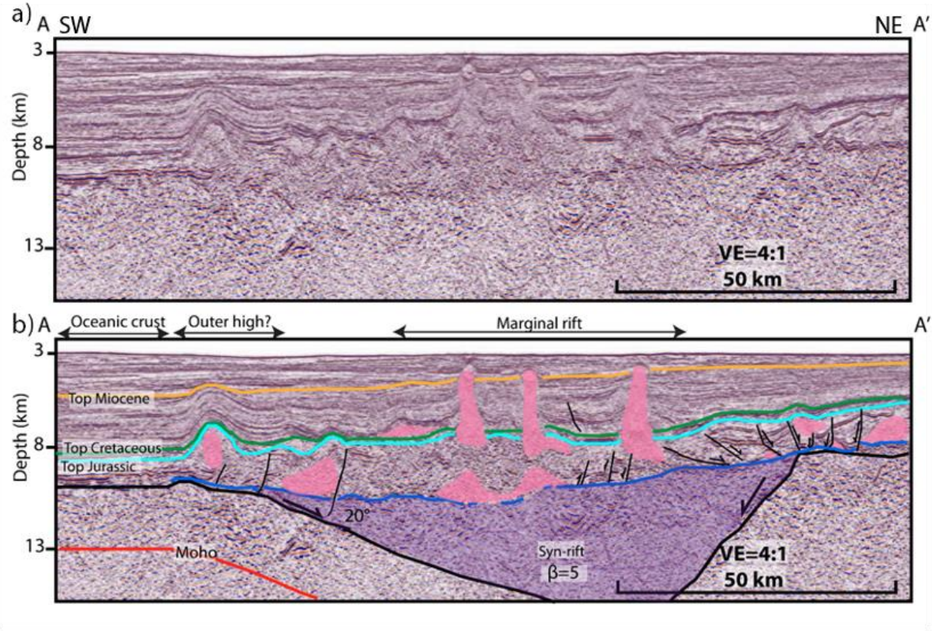
a)
A
SW
NE
A′
Depth (km)
3
8
13
VE=4:1
50 km
b)
A
Oceanic crust
Outer high?
Marginal rift
A′
Top Miocene
Top Cretaceous
Top Jurassic
20°
Moho
Syn-rift
β=5
VE=4:1
50 km

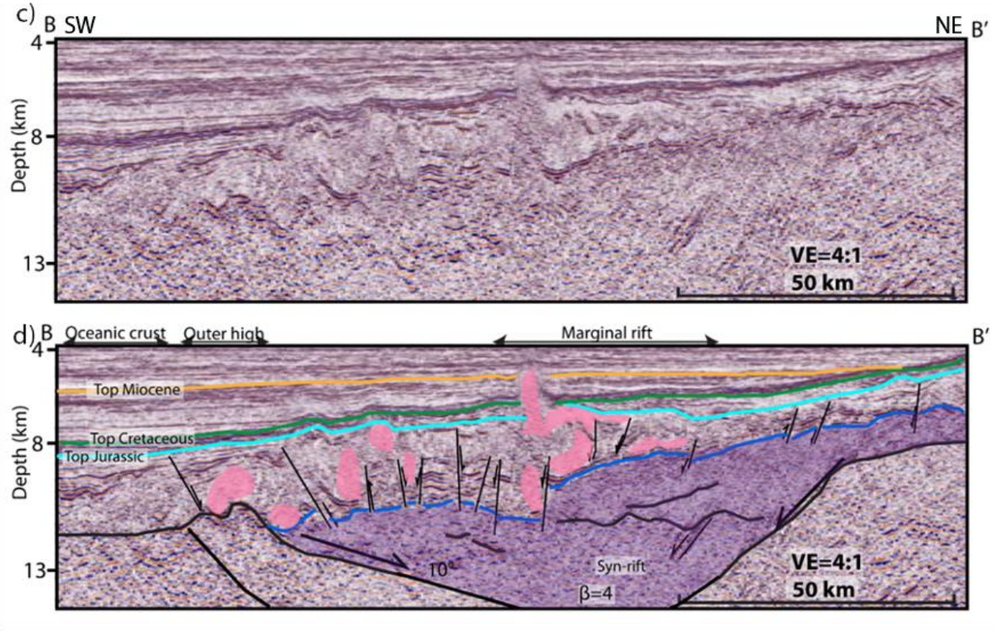
c)
B
SW
NE
B′
Depth (km)
4
8
13
VE=4:1
50 km
d)
B
Oceanic crust
Outer high
Marginal rift
B′
Top Miocene
Top Cretaceous
Top Jurassic
10°
Syn-rift
β=4
VE=4:1
50 km

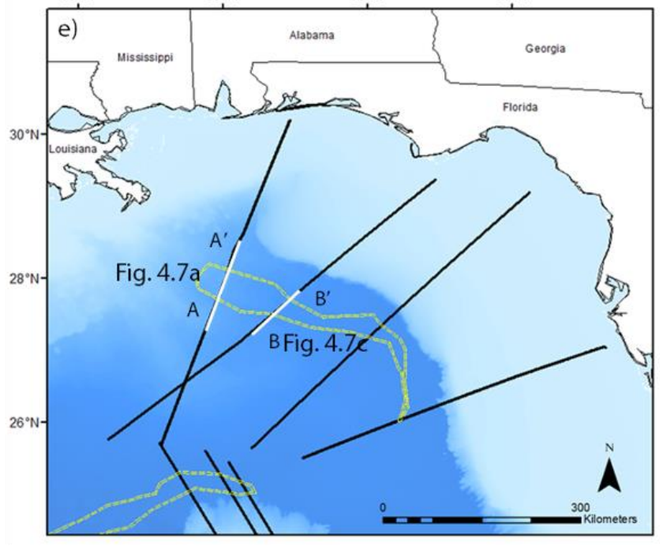
90°W
88°W
86°W
84°W
e)
Mississippi
Alabama
Georgia
Florida
Louisiana
30°N
28°N
26°N
A′
Fig. 4.7a
A
B′
B
Fig. 4.7c
N
0
300
Kilometers

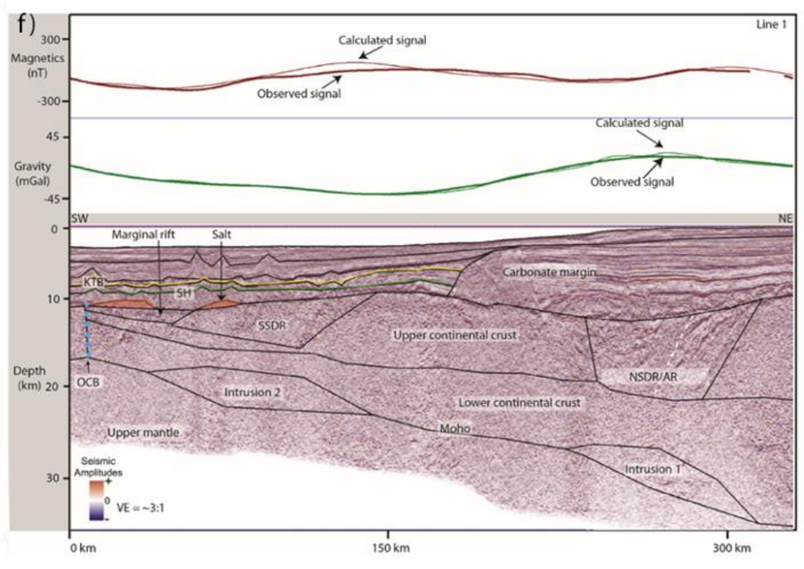
f)
Line 1
Magnetics (nT)
300
-300
Calculated signal
Observed signal
Gravity (mGal)
45
-45
Calculated signal
Observed signal
SW
NE
Depth (km)
0
10
20
30
Marginal rift
Salt
KTB
SH
Carbonate margin
SSDR
Upper continental crust
NSDR/AR
OCB
Intrusion 2
Lower continental crust
Upper mantle
Moho
Intrusion 1
Seismic Amplitudes
VE = ~3:1
0 km
150 km
300 km

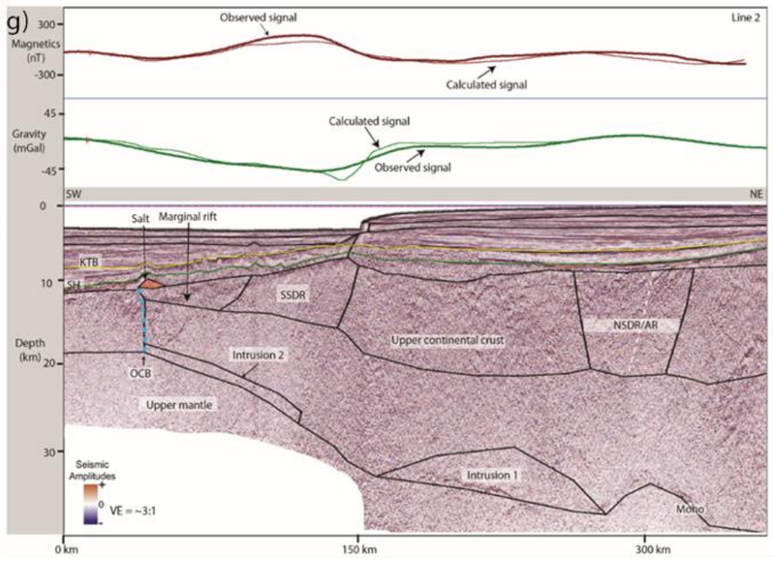
g)
Line 2
Magnetics (nT)
300
-300
Observed signal
Calculated signal
Gravity (mGal)
45
-45
Calculated signal
Observed signal
SW
NE
Depth (km)
0
10
20
30
Salt
Marginal rift
KTB
SH
SSDR
Upper continental crust
NSDR/AR
Intrusion 2
OCB
Upper mantle
Intrusion 1
Moho
Seismic Amplitudes
VE = ~3:1
0 km
150 km
300 km

On the Yucatan margin, large, vertical salt diapirs are confined within the fault-bounded interior of the underlying marginal rift (Kenning and Mann, 2021). Faulting within the marginal rift includes both landward-dipping and basinward-dipping normal faults as seen along A-A' and B-B' (Figure 4.7b, d). Sediments are elevated on the outer basement high that separates the continental and oceanic crust. The landward-dipping fault of the marginal rift has a dip angle of 20° and is classified as a low-angle normal fault (LANF) (Morley, 2014).

Transect B-B' is a regional dip line that is oriented northeast-southwest (Figure 4.7c, d). This line shows less vertical salt diapirism and slide structures along the inclined basal salt detachment within the Mesozoic as seen on transect A-A'. This marginal rift is 60 km wide with a thickness of 5 km and with most of its seismic reflectors dipping landward. The landward dipping normal fault has a dip of 10°. No SDRs or other evidence for magmatism is observed in this area. In contrast to this southern GOM margin, in Chapter 2 I described an SDR outside of the marginal rift with an inferred pre-rift age of late Triassic (Figure 2.5) This pre-rift SDR is less than 10 km in thickness and localized and does not appear to have any equivalent SDR on the southern GOM rifted margin on the Yucatan Peninsula.

In the northeastern GOM, the dip-oriented transect C-C' (Figure 4.8a and 4.8b) shows a much smaller marginal rift with a width of 30 km and thickness of 3 km. Although the base of salt is not well imaged on the seismic data, strata deformed by remobilized salt are observed near the shelf area above the marginal rift. The main landward-dipping LANF dips at an angle of 15°.

Figure 4.8. a) Uninterpreted seismic reflection line C-C' across the marginal rift in the northeastern GOM. b) Interpreted seismic reflection line C-C'. The purple color shows the inferred sedimentary fill with the marginal rift and the pink color are Jurassic salt deposits that were mainly concentrated in the less faulted sag basin that overlies the marginal rift. The true dip angles of both normal faults are 15°. c) Uninterpreted seismic example of the marginal rift along D-D' in the northeastern GOM. d) Interpreted seismic reflection line D-D'. e) Location map showing the location of the two seismic profiles.

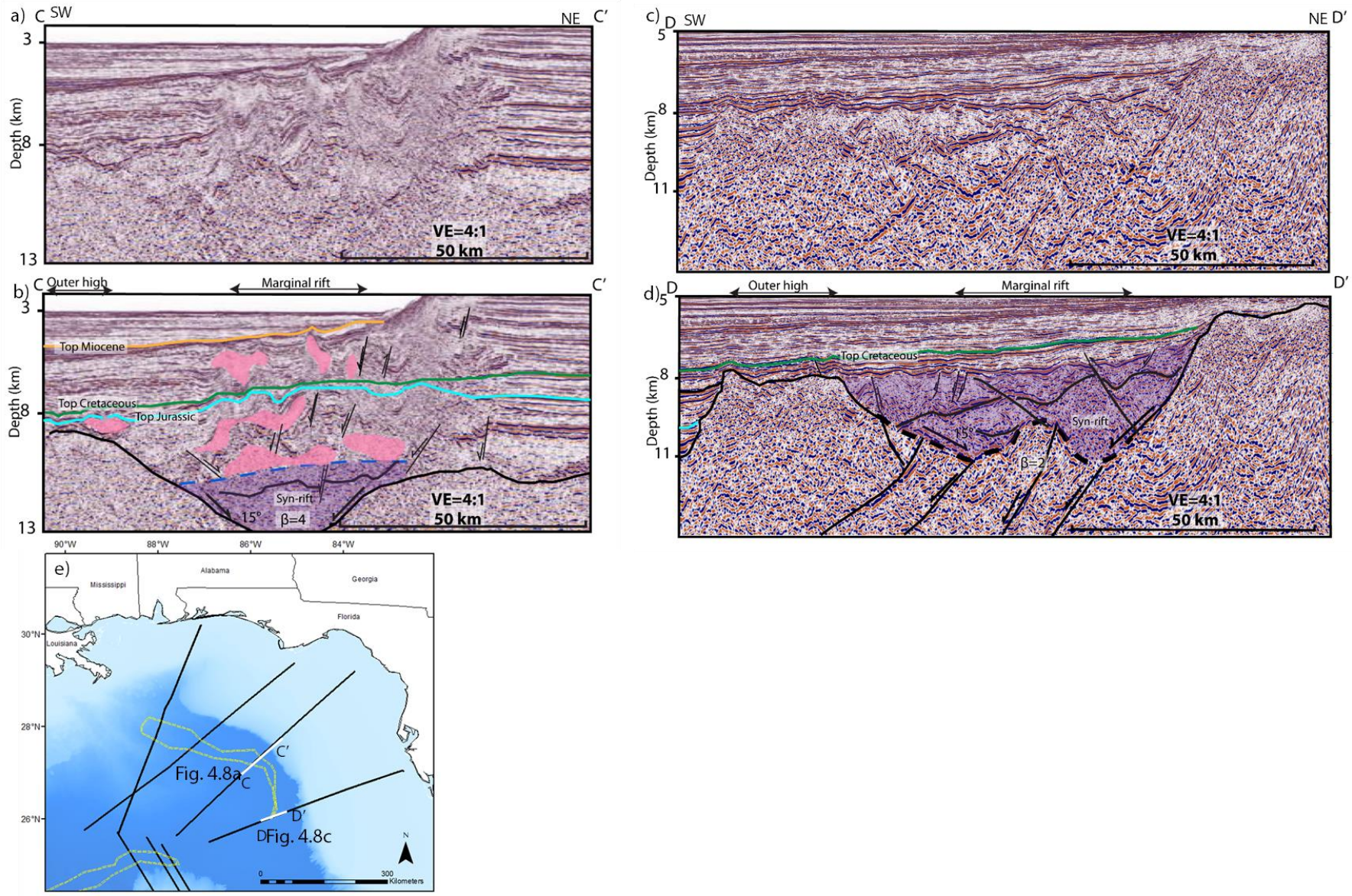
a) C SW
NE C′
3
8
13
Depth (km)
VE=4:1
50 km
b) C Outer high
Marginal rift
C′
Top Miocene
Top Cretaceous
Top Jurassic
Syn-rift
15°
β=4
c) D SW
NE D′
5
11
d) D
Outer high
Marginal rift
D′
β=2
90°W
88°W
86°W
84°W
e)
Mississippi
Alabama
Georgia
Florida
Louisiana
30°N
28°N
26°N
Fig. 4.8a
Fig. 4.8c
N
0
300
Kilometers

In the eastern part of the northeastern GOM, there is no clear salt bodies observed on transect D-D' (Figure 4.8c and 4.8d). A prominent outer basement high bounds the marginal rift in the basinward direction. Sub-horizontal and high-amplitude seismic reflectors are interpreted as sedimentary strata that infill the marginal rift (Figure 8d). The marginal rift has a much smaller width of 25 km and a sedimentary thickness of 3 km than other marginal rifts of the north-central GOM. The dip angle of the main landward LANF is 15°.

Description of the marginal rift zone of the northeastern Yucatan margin. Transect E-E' (Figure 4.9a and 4.9b) is located on the westernmost margin of the northern Yucatan Peninsula (Figure 4.9e). The marginal rift has a width of 50 km and a sedimentary thickness of 6 km. The landward-dipping LANF exhibits a fault dip angle of 30°. The upper section of sedimentary fill in marginal rift shows horizontal to sub-horizontal reflectors interpreted as sedimentary infill of the rift. Similar to the northeastern GOM, remobilized salt bodies are present as both salt diapirs and as rollovers produced by gravity sliding along a basal salt detachment (Steier and Mann, 2019). The detachment surface is relatively smooth compared to similar surfaces observed in the northeastern GOM.

Figure 4.9. a) Uninterpreted seismic reflection line E-E' across the marginal rift in the northeastern GOM. b) Interpreted seismic reflection line E-E'. The purple color shows the inferred sedimentary fill with the marginal rift and the pink color are Jurassic salt deposits that were mainly concentrated in the less faulted sag basin that overlies the marginal rift. The dip angles of both normal faults are 30° and 25°. The beta factor measured by the ratio of initial crustal thickness/thinned crustal thickness is high (~5) for line E-E'. c) Uninterpreted seismic example of the marginal rift along F-F' in the northeastern GOM. d) Interpreted seismic reflection line F-F'. e) Location map showing the location of the two seismic profiles.

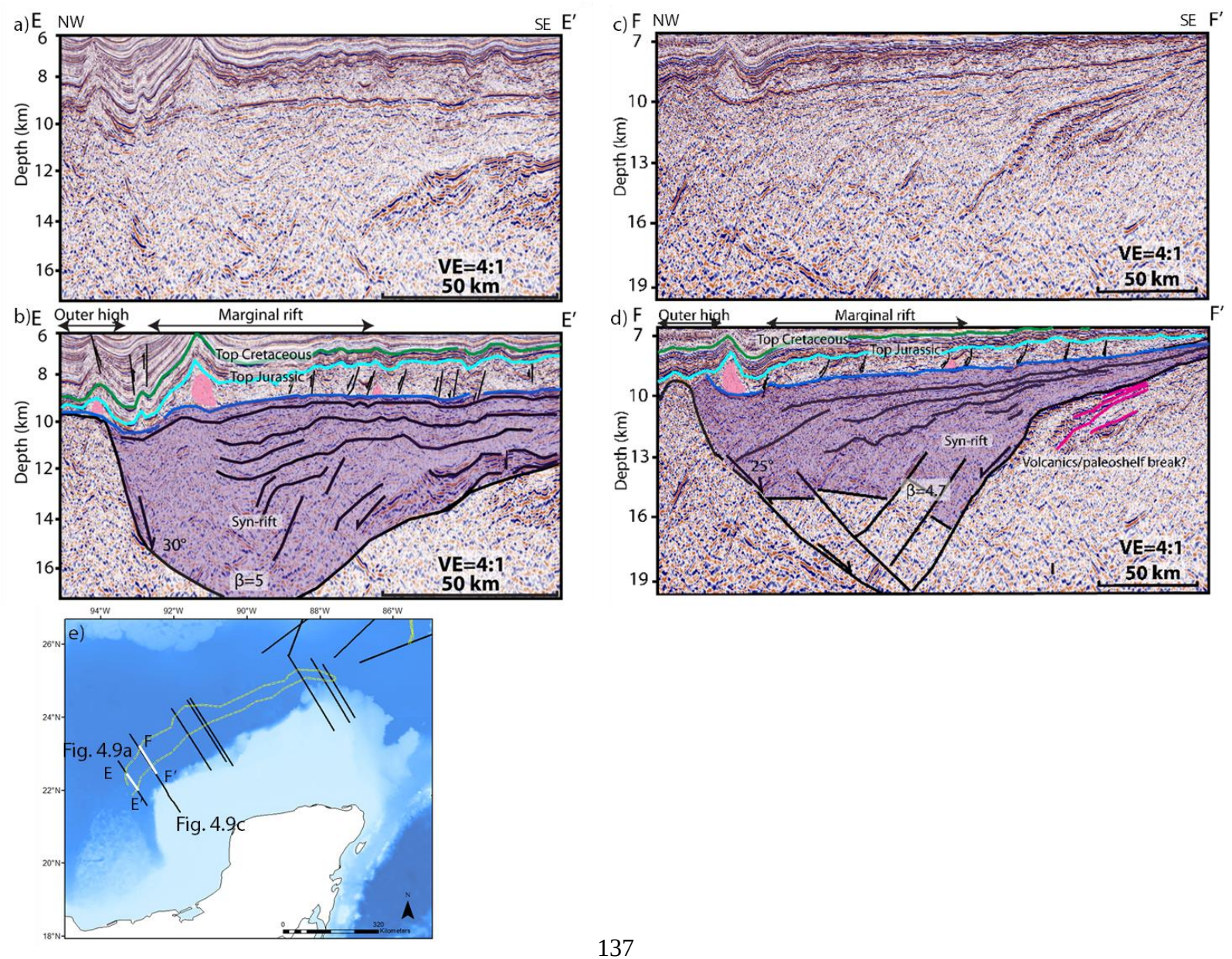
a) E
NW
SE
E′
Depth (km)
VE=4:1
50 km
b) E
Outer high
Marginal rift
E′
Top Cretaceous
Top Jurassic
Syn-rift
30°
β=5
VE=4:1
50 km
c) F
NW
SE
F′
VE=4:1
50 km
d) F
Outer high
Marginal rift
F′
Top Cretaceous
Top Jurassic
Syn-rift
25°
β=4.7
Volcanics/paleoshelf break?
VE=4:1
50 km
e)
94°W
92°W
90°W
88°W
86°W
26°N
24°N
22°N
20°N
18°N
Fig. 4.9a
F
E
F′
E′
Fig. 4.9c
N
0
320
Kilometers

Transect F-F' is a regional dip line showing a marginal rift with a width of 100 km and a sedimentary thickness of 5 km (Figure 4.9c and 4.9d). The dip angle of the landward-dipping normal fault dip is 25°. High-amplitude seismic reflectors dipping in the landward direction within the marginal rift are interpreted either as isolated volcanic flows or as a paleo-shelf break developed in sedimentary rocks.

Transect G-G' is a regional dip line showing prominent salt diapirs that are up to 7 km in width. The salt bodies deform the Mesozoic section and form a mini-basin (Figure 4.10b). Strata in the landward direction are clearly offset by normal faults associated with crustal necking in the underlying, pre-salt section. The marginal rift has a width of 25 km and a sedimentary thickness of 4 km. A landward-dipping LANF exhibits a fault dip angle of 20°.

Figure 4.10. a) Uninterpreted seismic reflection line G-G' across the marginal rift across the western Yucatan margin. b) Interpreted seismic reflection line G-G'. The purple color shows the inferred sedimentary fill with the marginal rift and the pink color are Jurassic salt deposits that were mainly concentrated in less faulted sag basin that overlies the marginal rift. The dip angles of both normal faults are 20° and 10°. c) Uninterpreted seismic example of the marginal rift along H-H' on the western Yucatan margin. d) Interpreted seismic reflection line H-H'. e) Location map showing the location of the two seismic profiles.

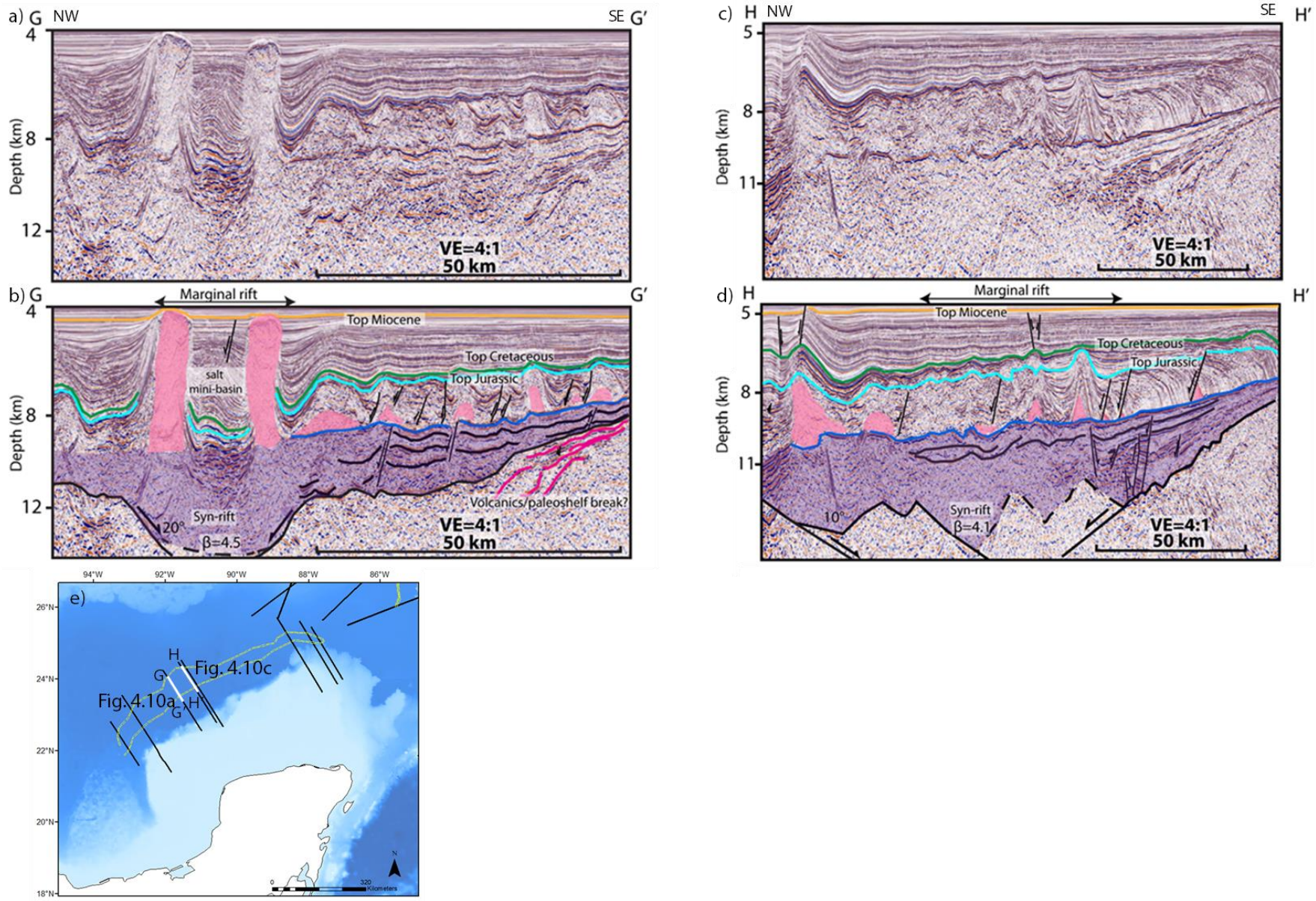
a) G
NW
SE G′
Depth (km)
4
8
12
VE=4:1
50 km
b) G
G′
Marginal rift
Top Miocene
Top Cretaceous
Top Jurassic
salt
mini-basin
Volcanics/paleoshelf break?
Syn-rift
20°
β=4.5
c) H
NW
SE
H′
5
11
d) H
H′
10°
β=4.1
e)
94°W
92°W
90°W
88°W
86°W
26°N
24°N
22°N
20°N
18°N
Fig. 4.10c
Fig. 4.10a
320
Kilometers

Transect H-H' is a regional dip line that shows that the marginal rift has a width of 50 km and a sedimentary thickness of 3 km (Figure 4.10c, d). Similar to transect G-G', the pre-salt section is offset by landward-dipping normal faults that formed during crustal thinning. The landward-dipping LANF dip angle is 10°.

Transect I-I' is a regional dip line that shows a decrease in salt volume (Figure 4.11a, b). The marginal rift is 50 km long with a 5 km thick sedimentary section with discontinuous parallel to semi-parallel reflections present beneath the basal salt detachment. The landward dipping LANF dips 16° to the southeast.

Figure 4.11. a) Uninterpreted seismic reflection line I-I' across the marginal rift across the western Yucatan margin. b) Interpreted seismic reflection line I-I'. The purple color shows the sedimentary fill with the marginal rift and the pink color are Jurassic salt deposits that were mainly concentrated in the less faulted sag basin that overlies the marginal rift. The dip angles of both normal faults are 16° and 15°. c) Uninterpreted seismic example of the marginal rift along J-J' on the western Yucatan margin. d) Interpreted seismic reflection line J-J'. e) Location map showing the location of the two seismic profiles.

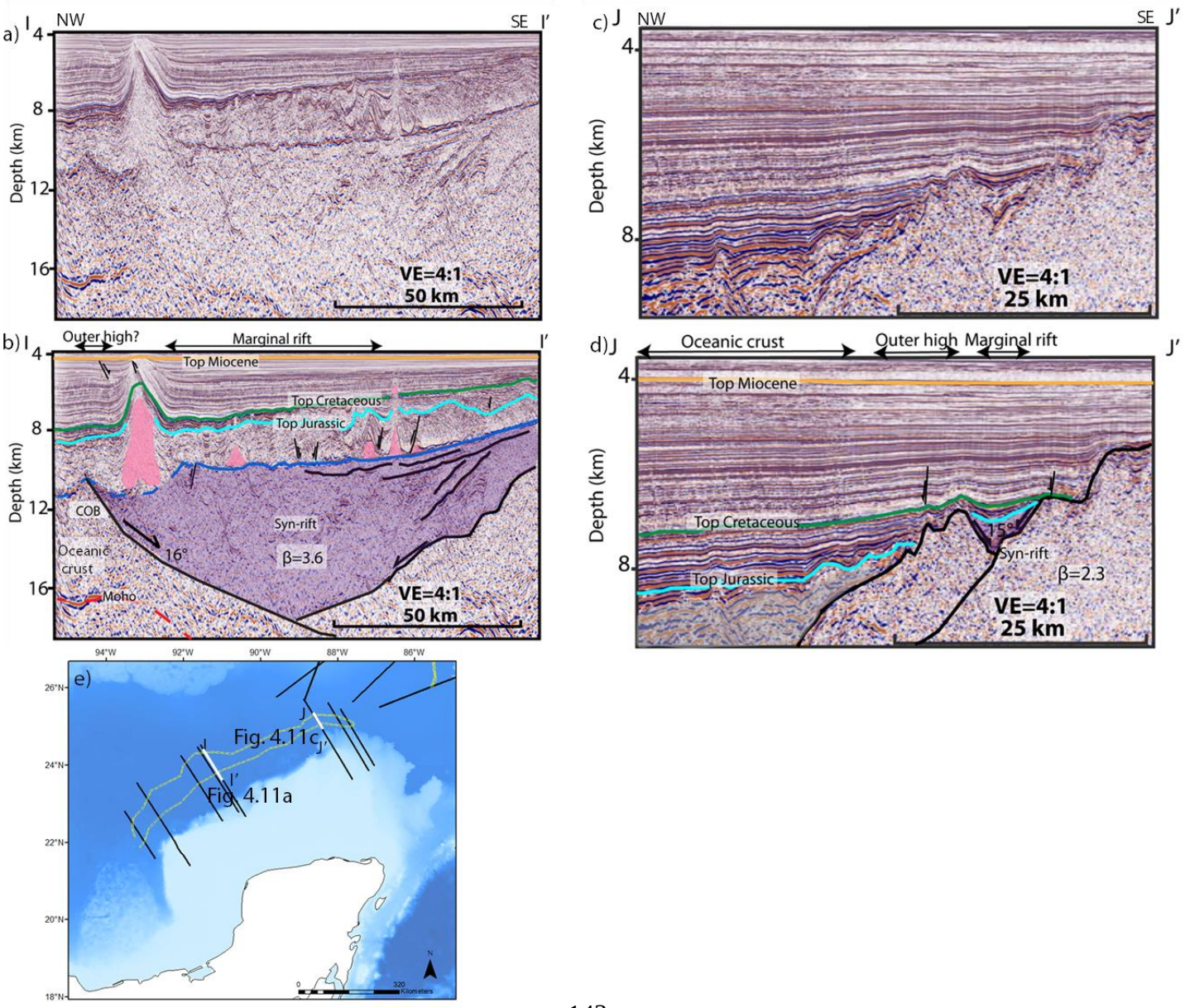
a) I
NW
SE
I′
Depth (km)
4
8
12
16
VE=4:1
50 km
b) I
Outer high?
Marginal rift
I′
Top Miocene
Top Cretaceous
Top Jurassic
COB
Syn-rift
Oceanic crust
16°
β=3.6
Moho
VE=4:1
50 km
c) J
NW
SE
J′
VE=4:1
25 km
d) J
Oceanic crust
Outer high
Marginal rift
J′
Top Miocene
Top Cretaceous
Top Jurassic
15°
Syn-rift
β=2.3
VE=4:1
25 km
e)
94°W
92°W
90°W
88°W
86°W
26°N
24°N
22°N
20°N
18°N
Fig. 4.11c
Fig. 4.11a
0
320
Kilometers

Transect J-J' is a regional dip line that crosses the northern Yucatan margin (Figure 4.11e). The size of the marginal rift is significantly smaller that rift segments to the west and exhibits a width of 8 km and a sedimentary thickness of 1 km. The landward-dipping LANF dips at an angle of 15°.

Transect K-K' shows no evidence of salt within or overlying the marginal rift (Figure 4.12a and b). Clear seismic reflections inferred as sedimentary layering within the marginal rift are observed. The marginal rift has a width of 7 km and thickness up to 5 km.

Figure 4.12. a) Uninterpreted seismic reflection line K-K' across the marginal rift across the eastern Yucatan margin. b) Interpreted seismic reflection line K-K'. The purple color shows the sedimentary fill with the marginal rift and the pink color are Jurassic salt deposits that were mainly concentrated in the less faulted sag basin that overlies the marginal rift. The dip angles of both normal faults are 17° and 14°. c) Uninterpreted seismic example of the marginal rift along L-L' on the eastern Yucatan margin. d) Interpreted seismic reflection line J-J'. e) Location map showing the location of the two seismic profiles.

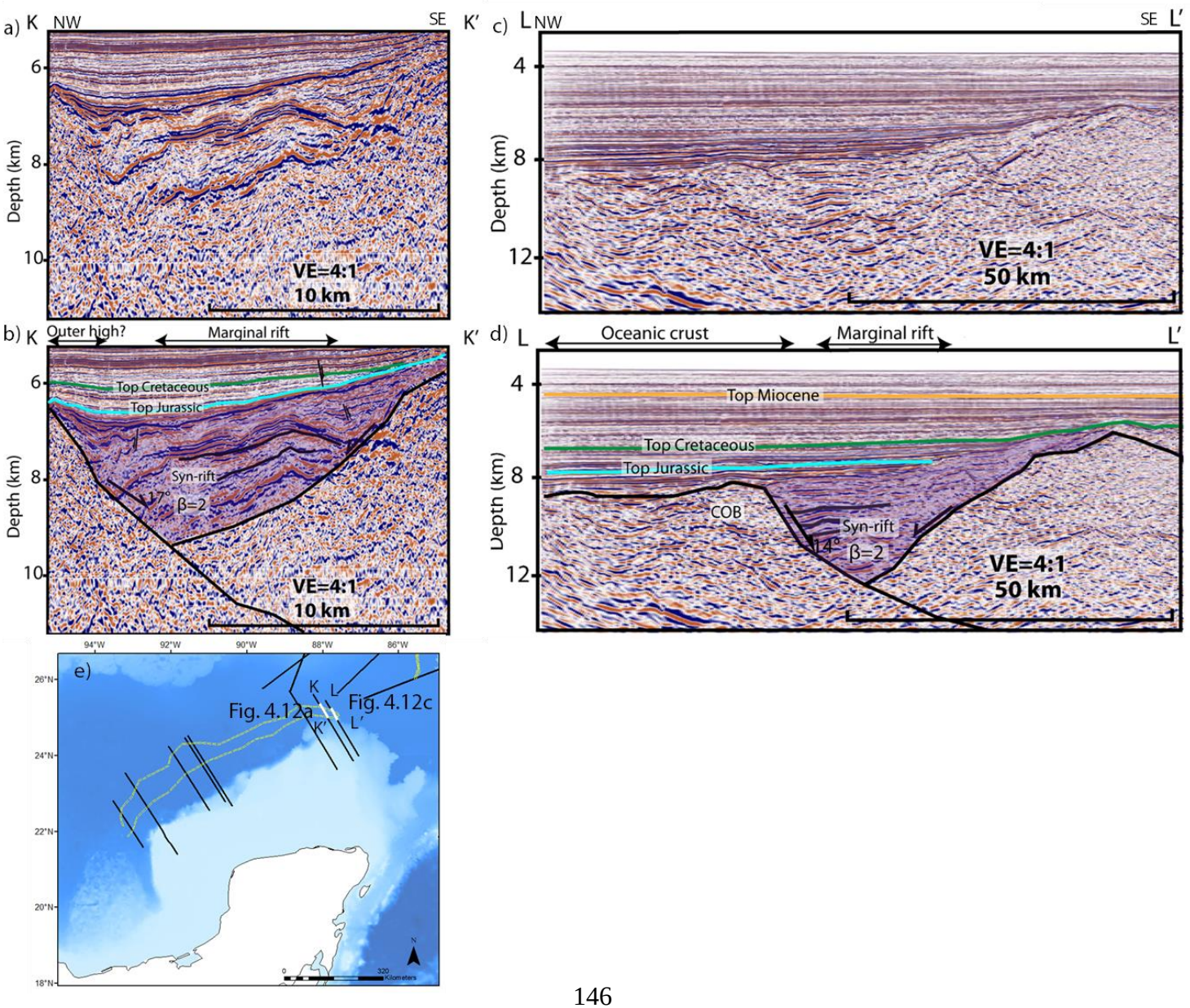
a) K
NW
SE
K′
Depth (km)
6
8
10
VE=4:1
10 km
b) K
Outer high?
Marginal rift
K′
Top Cretaceous
Top Jurassic
Syn-rift
17°
β=2
VE=4:1
10 km
c) L
NW
SE
L′
4
8
12
VE=4:1
50 km
d) L
Oceanic crust
Marginal rift
L′
Top Miocene
Top Cretaceous
Top Jurassic
COB
Syn-rift
14°
β=2
VE=4:1
50 km
e)
94°W
92°W
90°W
88°W
86°W
26°N
24°N
22°N
20°N
18°N
K
L
K′
L′
Fig. 4.12a
Fig. 4.12c
N
0
320
Kilometers

Transect L- L' is a dip line near the edge of the northern Yucatan margin and shows the marginal rift with a width of 12 km and thickness of 3 km. The landward-dipping LANF has a dip angle of 14°. Horizontal discontinuous, post-rift seismic reflectors are interpreted along the profile suggest this area has remained relatively structurally quiescent following the rifting event.

4.3.3. Salt accumulation in a sag basin in the marginal rift area and its age of deposition

A regional dip-oriented profile along G-G' (Figure 4.10a) is located in the northeast Yucatan margin and shows the presence of large salt diapirs and salt rollers in the up-dip direction (Figure 4.13). The age interpretations along this line were compiled from Kenning and Mann (2021). The normal faults deforming the younger Oligocene and Miocene sections are thin-skinned, gravity-controlled faults with minor fault offsets. Salt diapirs extend vertically to the seafloor and are concentrated in a post-rift sag basin that overlies the marginal rift. As there is no apparent salt that extends deeper into the basal part of the rift, I infer that the age of the salt-filled sag basin to be post-rift. As there are no direct age constraints on either the syn-rift or post-rift sag basin, Pindell et al. (2020) has proposed that the age of the salt ranges over a period of 11 Ma from Bajocian (170 Ma) to Oxfordian (159 Ma).

Figure 4.13. Sequential structural restoration using MOVE software for seismic profile along G-G' shown in Figure 4.10 for horizons from the top Triassic (H) to present-day (A). The extension of marginal rift shown in purple and its overlying sag basin provided local accommodation space for mainly post-rift salt deposition. Late Jurassic oceanic crust is shown in blue and thinned continental crust is shown in grey. A. Present-day passive margin period. B. Top Miocene passive margin period. C. Top Oligocene. D. Top Mid-Eocene passive margin period. E. Top Paleocene passive margin period. F. Top Cretaceous passive margin period. G. Top Jurassic post-rift period. H. Top Triassic pre-rift period. See text for discussion.

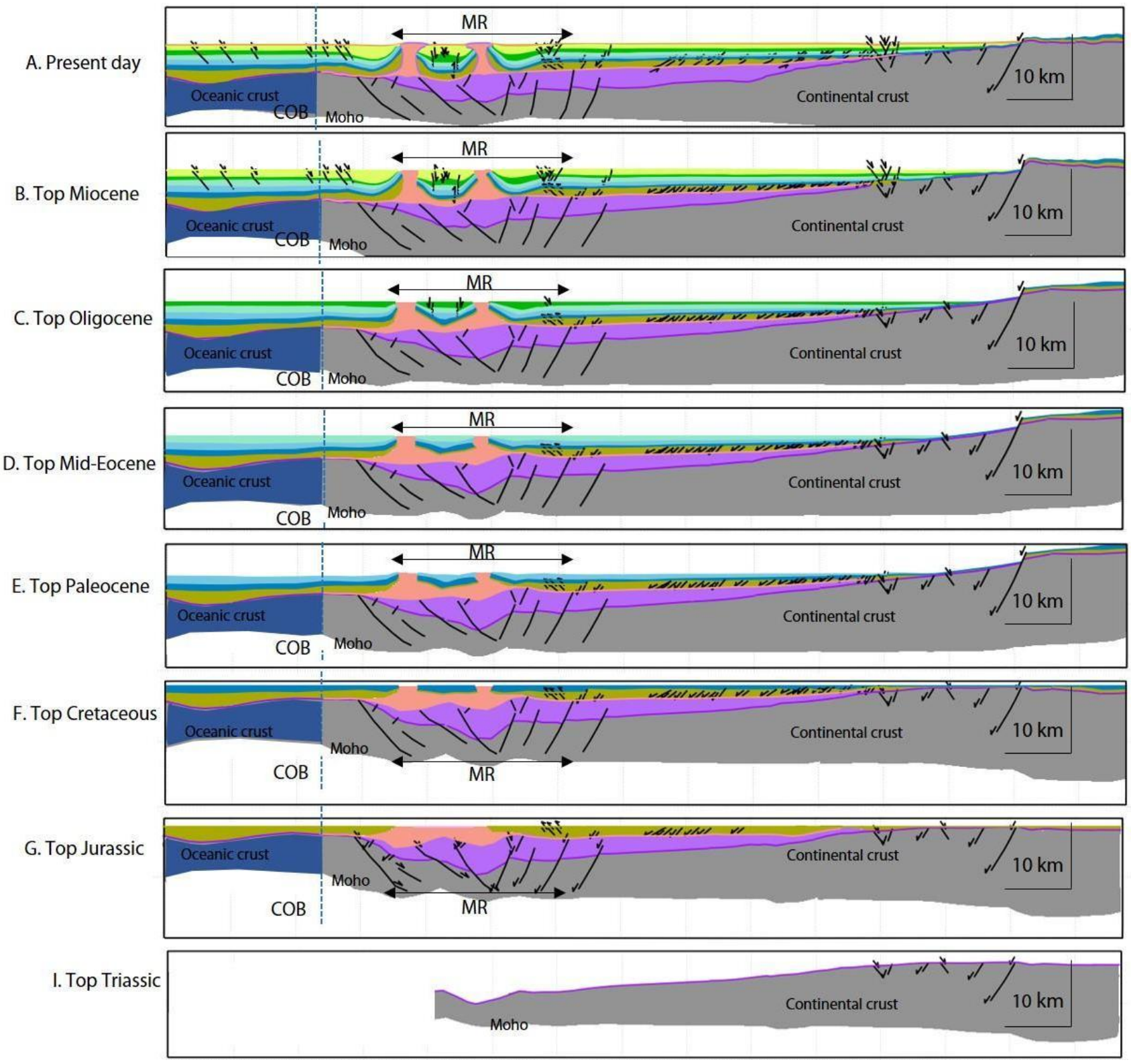
A. Present day
MR
Oceanic crust
COB
Moho
Continental crust
10 km
B. Top Miocene
MR
Oceanic crust
COB
Moho
Continental crust
10 km
C. Top Oligocene
MR
Oceanic crust
COB
Moho
Continental crust
10 km
D. Top Mid-Eocene
MR
Oceanic crust
COB
Moho
Continental crust
10 km
E. Top Paleocene
MR
Oceanic crust
COB
Moho
Continental crust
10 km
F. Top Cretaceous
Oceanic crust
Moho
COB
MR
Continental crust
10 km
G. Top Jurassic
Oceanic crust
Moho
COB
MR
Continental crust
10 km
I. Top Triassic
Moho
Continental crust
10 km

This proposed Bajocian-Oxfordian (170-159 Ma) age for the salt and the inferred age of the oceanic crust beneath the central GOM of Tithonian (150-137 Ma) by (Snedden et al., 2014) would mean would there was a 9 Ma lag between the end of rifting and the initiation of oceanic spreading. This discrepancy may indicate an error in the age estimates for either the age or rifting or the age of oceanic crust or both.

Miocene strata exhibit significant thickness variations near the diapirs above the marginal rift, suggesting that most salt remobilization occurred as the result of sediment loading during the Miocene that is generally attributed to the formation and growth of the Mississippi deep-sea fan during this period (Hudec et al., 2019; Steier and Mann, 2019). Most of the Cenozoic section is relatively undeformed except the distal zone associated with the growth of salt diapirs. Small-offset and thin-skinned normal faults are present throughout the Cenozoic section and dip both landward and basinward.

The development of salt rollers occurs within the Mesozoic section and are associated with substantial wedge geometries within the post-salt Jurassic section and overlying Cretaceous section (Figure 4.13). These growth strata indicate that the down-dip translation and extensional faulting began in the late Jurassic and continued through the Cretaceous as observed for salt rollers in both the northern and southern GOM (Pilcher et al., 2014; Steier and Mann, 2019).

Although uncertainty exists when restoring the salt as salt flows in a three-dimensional direction as diapirs can widen or narrow during extension and contraction, the restoration in Figure 4.13 provides a possible interpretation for the marginal evolution. During the Jurassic, salt was deposited in the topographic lows of the sag basin formed above Phase 1 rifts and salt in the more up-dip locations of the sag basin began sliding into the lower-lying marginal rift area.

There are two previous explanations for the thicker salt layer in the area overlying the marginal rift. Similar to my interpretation presented in this chapter, Rowan (2018) suggested a high-relief salt deposition model where salt deposition occurred in a post-rift sag setting within a restricted and barred basin 2 to 3 km below sea level. A contrasting model by Pindell et al. (2014) proposed that the salt was deposited in a low-relief setting near sea level but then subsided instantaneously up to 3 km during rifting and rapid collapse of the underlying mantle.

4.4 Discussion

4.4.1 Summary of major characteristics of the GOM marginal rift system

In this chapter, I integrated gravity and magnetic data with 12 regional and deep-penetrating, seismic reflection profiles from the margins of the US and Mexican GOM to show that the GOM marginal rift system forms a 378-km-long, continuous zone along the northern US GOM and a 678-km-long, zone along the northern margin of the Yucatan Peninsula in the Mexican GOM (Figure 4.1).

Characteristics of the marginal rift system include: 1) the marginal rifts form an elongate, circum-GOM zone of full-grabens or half-grabens that likely extend westward for hundreds of kms under the Louann salt body in the US GOM; the progressive disappearance of the marginal rifts to the southeast in west-central Florida and eastern Yucatan reflects minimal extension and necking of the continental crust near the GOM pole of rigid phase opening; 2) marginal rifts vary from 25-55 km in width and vary from 1-9 km in sedimentary thickness; 3) marginal rifts overlie necked continental crust that ranges in thickness from 6-10 km as estimated from gravity modeling and from seismic refraction and reflection data; the marginal rifts are bounded by low-angle, normal faults (LANFs) that vary in dip from 10-30°; 4) marginal rifts form elongate and

continuous gravity and magnetic lows; 5) quantitative, plate restorations using oceanic fracture zones realign the eastern endpoints of the MRS on both conjugate margins within an error of 20 km; 6); the age of marginal rifting pre-dates the deposition of the widespread Louann-Campeche salt layer that was deposited in unfaulted sag basins and is inferred from previous work by Pindell et al. (2020) to range in age from Bajocian (170 Ma) to Oxfordian (159 Ma); and 8) the age of central GOM oceanic crust pre-dates the formation of the salt layer and is estimated from Tithonian (150 Ma) to Berriasian (137 Ma) by Snedden et al. (2014) and from Oxfordian (159 Ma) to Berriasian (139 Ma) by Pindell et al. (2016).

4.4.2 Marginal rift analogs in the South China Sea, Brazil, Norway, and Angola

Figure 4.14 provides four, proposed analogs of marginal rifts identified on the rifted margins of the South China Sea, Brazil, Norway. All four of these rifts are proposed as similar structural and crustal analogs to the marginal rifts that I have described from the GOM.

South China Sea. A seismic reflection line from Franke et al. (2011) crosses the Palawan shelf and slope of the eastern rifted margin of the South China Sea basin and shows a marginal rift overlying the necked zone of continental crust adjacent to oceanic crust (Figure 4.14a). An inner and outer rift basins are present and separated by a structural high formed as a horst block of either volcanic material (Schluter et al., 1996) - or alternatively, rifted continental crust with minor magmatic additions as the magnetic data show a small scale, high-frequency pattern that is typical for a continental crust (Franke et al., 2011).

Figure 4.14. Proposed analogs for other marginal rifts outside of the GOM in the South China Sea and Brazil. a) Seismic profile on the non-volcanic, rifted southeastern margin of the South China Sea modified from Franke et al. (2011) that shows a 40-km-wide marginal rift within the necked zone of continental crust bounded by an outer structural high and an inner structural high. Seismic refraction from Franke et al. (2011) confirms that the crustal types of both highs is thinned continental crust. Map of South China Sea with line location in C. b) Seismic profile of the rifted continental margin of Brazil beneath the Espírito Santos basin modified from Mohriak (2019) that shows a 30-km-wide marginal rift bounded by Precambrian crust along its landward edge and an outer high of possible volcanic origin or intruded, continental crust along its outer edge. Map of Brazilian margin with line location in D. c) Line drawing example of the rifted Mid-Norwegian margin from Peron-Pinvidic and Osmundsen (2016). d) Sketched regional seismic transection across the central Kwanza basin from Kukla et al., (2018). e) Location map of seismic profile A-A' in the South China Sea. f) Location map of seismic profile B-B' in Espírito Santos basin of Brazil. g) Location map of the seismic profile C-C' in offshore Norway. h) Location map of schematic transect D-D' in central Kwanza Basin .

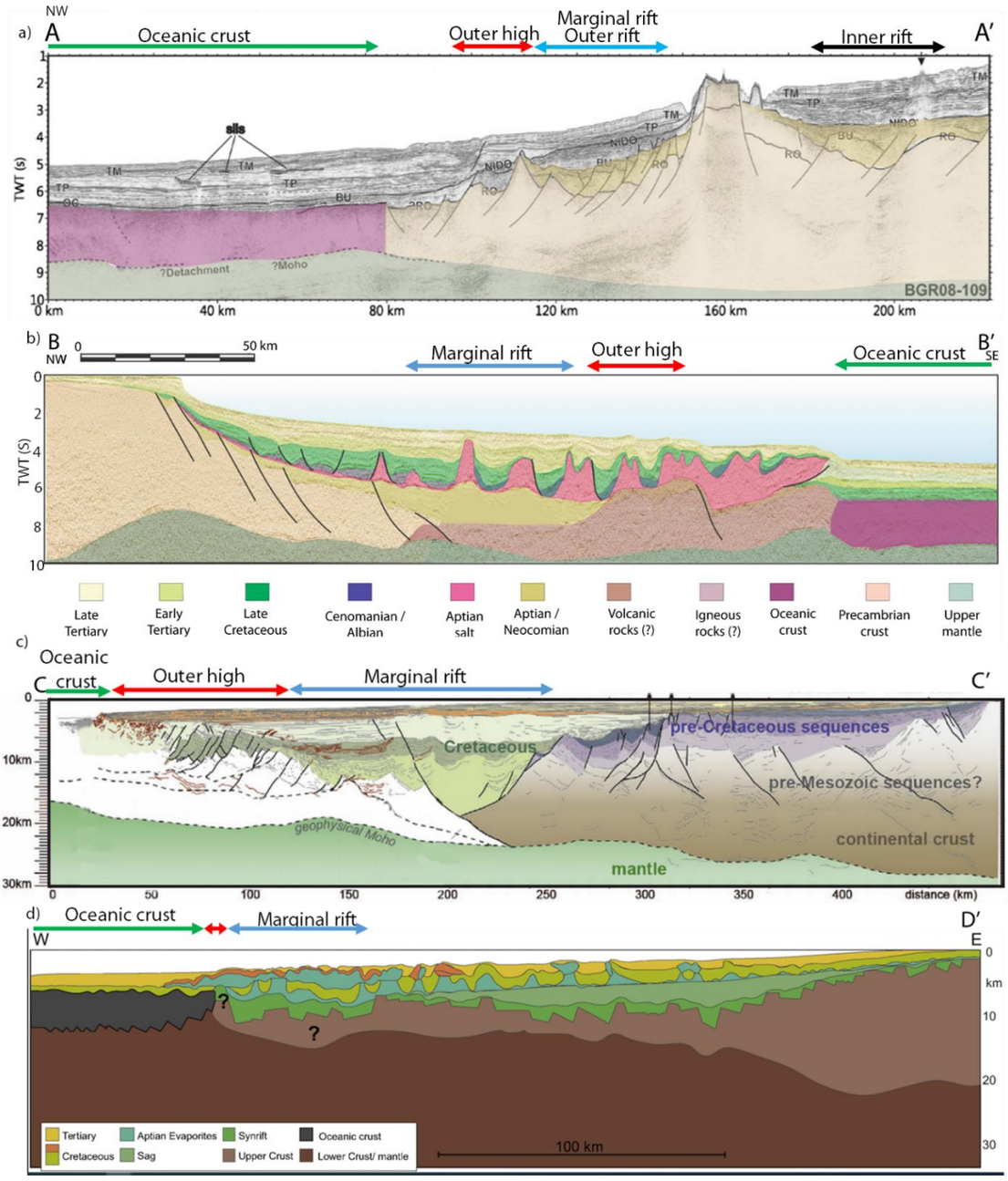
a)
NW
A
Oceanic crust
Outer high
Marginal rift
Outer rift
Inner rift
A′
TWT (s)
sills
TM
TP
BU
RO
NIDO
?Detachment
?Moho
BGR08-109
0 km
40 km
80 km
120 km
160 km
200 km
b)
B
NW
0
50 km
Marginal rift
Outer high
Oceanic crust
B′
SE
TWT (S)
Late Tertiary
Early Tertiary
Late Cretaceous
Cenomanian / Albian
Aptian salt
Aptian / Neocomian
Volcanic rocks (?)
Igneous rocks (?)
Oceanic crust
Precambrian crust
Upper mantle
c)
Oceanic crust
C
Outer high
Marginal rift
C′
pre-Cretaceous sequences
Cretaceous
pre-Mesozoic sequences?
continental crust
geophysical Moho
mantle
10km
20km
30km
0
50
100
150
200
250
300
350
400
distance (km)
d)
Oceanic crust
Marginal rift
D′
W
E
?
?
km
10
20
30
Tertiary
Cretaceous
Aptian Evaporites
Sag
Synrift
Upper Crust
Oceanic crust
Lower Crust/ mantle
100 km

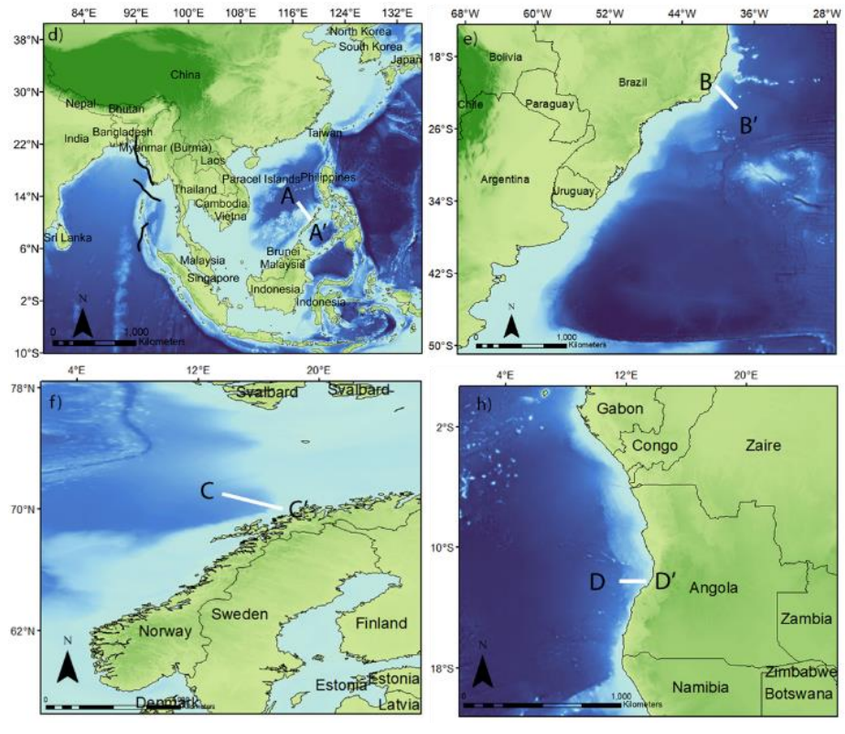
d)
China
North Korea
South Korea
Japan
Nepal
Bhutan
India
Bangladesh
Myanmar (Burma)
Laos
Taiwan
Paracel Islands
Philippines
Thailand
Cambodia
Vietnam
A
A′
Sri Lanka
Malaysia
Singapore
Brunei
Malaysia
Indonesia
Indonesia
e)
Bolivia
Brazil
Chile
Paraguay
B
B′
Argentina
Uruguay
f)
Svalbard
Svalbard
C
C′
Sweden
Norway
Finland
Estonia
Estonia
Latvia
Denmark
h)
Gabon
Congo
Zaire
D
D′
Angola
Zambia
Namibia
Zimbabwe
Botswana

The outer rift basin, similar to the marginal rift, has a width of 50 km and 1 second (TWT) of sedimentary rocks. The 2D gravity model along this profile by Franke et al. (2011) modeled the outer rift basin fill with a density of 2.6 g/cc, consistent with the value for the marginal rift in the GOM. The syn-rift sediments are restricted to a few local basins bounded by large, normal faults.

Brazil. A regional seismic profile (Figure 4.14b) from Mohriak (2019) across the Espirito Santo Basin of the rifted margin of offshore Brazil images the necking of full-thickness, continental crust beneath the platform, across an area of thinned, continental crust to oceanic crust beyond the seaward limit of salt (Figure 4.14d). The Aptian salts slide downslope along an inclined basal salt detachment with salt rollers present in the up-dip direction. Salt mobilization includes salt diapirs in the distal zone with extrusion of salt over the structure high adjacent to oceanic crust.

Angola. The marginal rift in this region bounded by the outer high to the basinward has a width of 40 km and syn-rift sedimentary fill is up to 3s (TWT). The nature of the structural high observed between the marginal rift and the oceanic crust has been proposed as both continental and oceanic in origin (Kukla et al., 2018; Figure 4.14d). Mohriak et al. (2008) analyzed potential field data and suggested this structural high corresponds to the volcanic basement high formed after the rifting phase.

Norway. A thickly sedimented marginal rift is observed in this segment of the Norwegian rifted margin (Figure 4.14c). Peron-Pinvidic and Osmundsen (2016) suggest the outer basement high is underlain by hyperextended crustal material and has acted as a tilted fault block that confines the marginal rift.

4.4.3. Low-angle normal fault (LANF) analogs from areas outside of the GOM

Several examples of large low-angle normal faults (LANF) have been studied in active and ancient rift settings worldwide (Morley, 2014). Syn-rift clastic and volcaniclastic sedimentary units associated with LANFs are generally found to thicken toward the border fault and display a progressive decrease in dip upsection with coarser-grained facies immediately adjacent to the border-fault system (Schlische et al., 2003). One previous explanation for LANFs is that they form as high-angle normal faults and are later rotated by later extensional events into low-angle normal faults (Buck, 1988; Morley, 2009). My interpretation is that the necked zone of continental crust that is extended in the period immediately prior to full continental rupture and the formation of an oceanic spreading ridge (Peron-Pivinidic et al., 2016) would be an ideal setting for LANFs to form. Therefore, these LANFs may require onlay a single phase of extension to form rather than multiple events as proposed by Buck (1988) and Morley (2009).

This chapter measured and documented the low-angle landward normal fault dip angles in the GOM to compare with the LANFs previously studied in onshore Thailand, East Africa Rift, and the Atlantic margin (Figure 4.15). Taking into account the variable length and size of the LANFs, I plotted the dip angles for each fault studied (Figure 4.15f).

The dips of LANFs range from the lowest dips of 10° in the GOM and Orphan Basin in offshore Canada to the highest dips of 45 ° in onshore Thailand (Figure 4.15). The regional dip profile of the Orphan basin is located offshore Canada where the northwest-dipping, low-angle detachments offset the base of Mesozoic strata and fault dip was measured from the original seismic profile from Cawood et al. (2021) (Figure 4.15a). The fault dip varies more significantly along the northwestern end of the fault as compared to the southeastern end of the fault.

Figure 4.15. a) Comparison of the along strike variations in the fault dip angle of low-angle normal faults (LANFs) of the GOM compared to rift systems in other areas of thinned continental crust that are bounded by LANFs in Canada, Thailand, Atlantic margin of the eastern USA, the Apalachicola rift in the northeastern GOM, and the East Africa rift. Location of the seismic profile showing Mesozoic LANFs in the Orphan basin offshore Canada (Sharma et al., 2021). b) Location of the active, western boundary LANF of the Phitsanulok basin in Thailand (Morley, 2009). c) Location of Jurassic LANFs in the Apalachicola Rift (AR) in the northeastern GOM (Storey, 2020) and the circum-GOM marginal rift described in this chapter. d) Location of active LANF bounding the Lokichar basin of East Africa Rift (Morley, 1999). e) Locations of cross-sections of Triassic LANFs along the Atlantic margin of the eastern USA that include the Jedburg, Taylorsville, and Fundy rifts as described by Schlische et al. (2002).

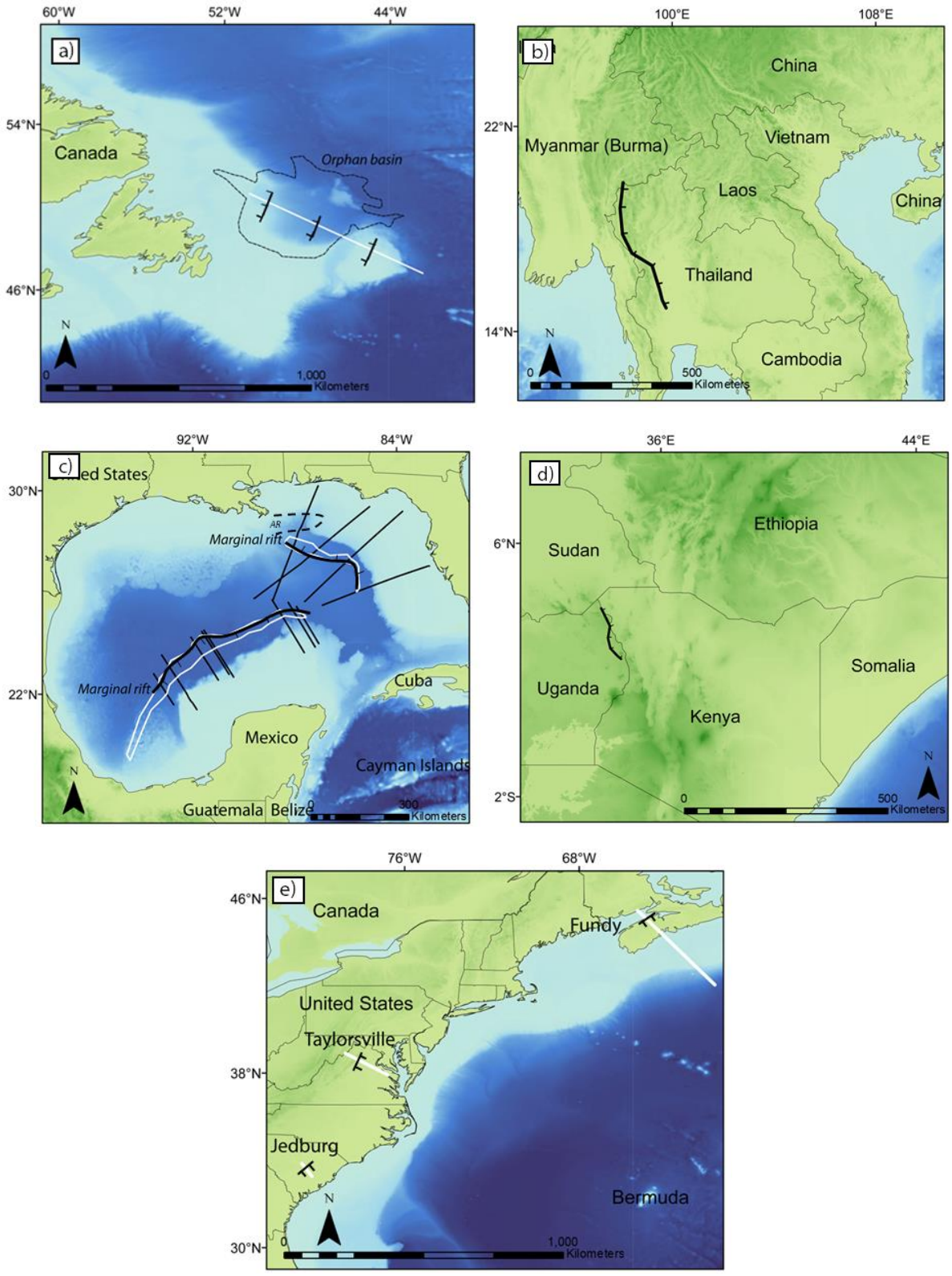
a)
60°W
52°W
44°W
54°N
46°N
Canada
Orphan basin
N
0
1,000
Kilometers
b)
100°E
108°E
22°N
14°N
China
Myanmar (Burma)
Vietnam
Laos
China
Thailand
Cambodia
N
0
500
Kilometers
c)
92°W
84°W
30°N
22°N
ited States
AR
Marginal rift
Marginal rift
Cuba
Mexico
Cayman Islands
Guatemala
Belize
N
300
Kilometers
d)
36°E
44°E
6°N
2°S
Ethiopia
Sudan
Somalia
Uganda
Kenya
N
0
500
Kilometers
e)
76°W
68°W
46°N
38°N
30°N
Canada
Fundy
United States
Taylorsville
Jedburg
Bermuda
N
0
1,000
Kilometers

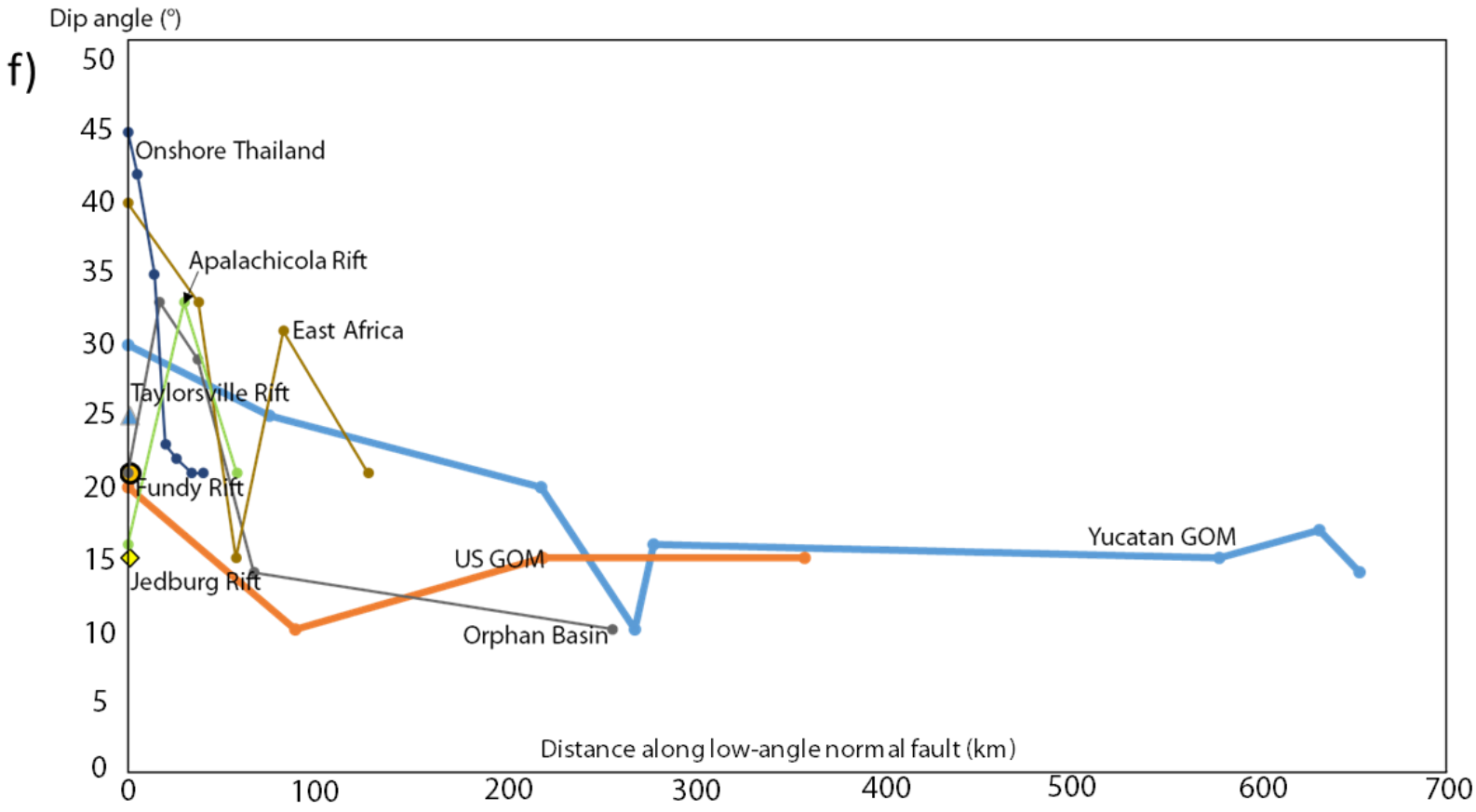
f)
Dip angle (°)
50
45
40
35
30
25
20
15
10
5
0
Onshore Thailand
Apalachicola Rift
East Africa
Taylorsville Rift
Fundy Rift
Jedburg Rift
US GOM
Orphan Basin
Yucatan GOM
0
100
200
300
400
500
600
700
Distance along low-angle normal fault (km)

The dip of the western boundary fault (Figure 4.15b) changes along strike from south to north in the Phitsanulok Basin of onshore Thailand as measured by Morley (2009). The Apalachicola rift (AR) located in the northeastern GOM that was imaged on several seismic reflection profiles presented by Storey (2020) and show that these LANFs range in dip from 16° to 33°. The Lokichar basin in East Africa Rift displays low-angle normal fault dips that range from 21° to 40°. More examples of LANFs along the Mesozoic rifted margin of eastern North America, include the Jedburg, Taylorsville, and Fundy rifts as described by Schlische et al. (2002).

The LANF dip angles of marginal rifts range from 10° to 30° (Figure 4.15f). The range of the fault dips from the GOM marginal rifts is within the dip range of the other LANFs described above. Morley (2009) interpreted that the low-angle dips in Thailand appear to follow preexisting low-angle fabrics, such as thrusts, shear zones, and other low-angle ductile foliations (Figure 4.15b). In the Phitsanulok Basin, the fault dip angle is higher to the south adjacent to the Mae Ping transfer fault zone compared to the north along strike (Figure 4.15b).

Similarities could be observed from these low-angle normal faults of Asia with those along the Atlantic margin and the GOM. For example, the Mesozoic Orphan Basin, Jedburg, Fundy, and Taylorsville rifts along with other marginal rifts of the GOM all show similar ranges of LANF fault dips that are relatively lower (15°-25°) than the active LANFs of onshore Thailand (20°-45°) and East Africa Rift (15°-40°).

4.4.4. Change in width of the rift zone and beta factor in response to changes in the orientation of basement structural grain

Reuber and Mann (2019) compiled beta factors from rifts along passive margins and used these data to propose that lower beta factor rifts are common to areas where the rift propagates parallel to the weak structural grain inherited from previous orogenic events. In this fabric-parallel

rift setting, the resulting rift zone is narrow and the observed amount of crustal stretching is low because the crust requires less extension to fully rupture the continental crust and initiate oceanic spreading.

In contrast, higher beta factor rifts and wider zones of rifting are common to areas where the rift propagates at right angles to a stronger grain inherited from previous orogenic events. In this fabric-orthogonal situation, the rift zone is much wider and the observed amount of crustal stretching is higher because the continental crust requires much more extension to fully rupture and initiate oceanic spreading.

In Figures 16a and b, I used the crustal thickness map from Chapter 3 to remove the late Jurassic oceanic crust from the center of the GOM basin and realign the pre-Phase 2 oceanic features. Higher beta factors cluster in the northeast GOM and eastern Yucatan conjugate margins and tend to be roughly similar on both conjugates as might be predicted using the Reuber and Mann (2019) model based on the orientations of orogenic, basement fabrics (Fig. 4.16c and d). The marginal rift disappears as the rift was propagating to the southeast and normal fault displacements progressively decrease in that direction.

Following the Reuber and Mann (2019) model, the explanation for higher beta factors in this area of the eastern GOM is explained by the orthogonal orientation of the southeastward rift propagation direction relative to the northeast-trending basement fabrics as expressed on the magnetic map in Figure 4.5. The resulting trend of the crustal fabrics at a high angle to the direction that the rift was propagating requires more extension and extension to fully rupture the continental crust and may have ultimately led the GOM rift to stop propagating southeastwards into this area to the northwest of Cuba.

Figure 4.16. a) Crustal thickness map that was developed and discussed in detail in Chapter 3 of this dissertation. **b)** Crustal thickness map overlay on late Jurassic reconstruction at 160 Ma by removing the oceanic crust prior to late Jurassic seafloor spreading. **c)** Beta factor map for the GOM Phase 2 opening that was presented and discussed in detail in Chapter 3. **d)** Beta factor map overlain on late Jurassic reconstruction at 160 Ma during the period of Phase 2 rifting prior to the formation of oceanic crust in the GOM. Thin, yellow lines are the structural grain in basement rocks from late Paleozoic orogeny and Triassic-early Jurassic, Phase 1 rifting. Central yellow line with numbers 1-4 is the site of future oceanic crust formation with **number 1** showing the area where the rift crosses at right angles to the basement structural grain; **number 2** showing area where the rift crosses obliquely to the basement structural grain; **number 3** where the West Main Transform fault parallels the basement structural grain; and **number 4** where the tip of the GOM Phase 2 rift terminated near Cuba. Inferred Triassic-early Jurassic rifts formed during Phase 1 northwest to southeast rifting are shown as purple lines. Better-imaged, Late Jurassic Phase 2 marginal rifts described shown in Figures 4.6-4.12 of this chapter are shown as red lines. Off-axis, Phase 2 marginal rifts that include the Bravo trough in the western GOM (Hudec et al., 2013) and the Apalachicola and the Elbow rifts in the northeastern GOM (Storey, 2020). These off-axis, Phase 2 rifts also shown in red in the NE GOM are attributed to a wider zone of Phase 2 rifting resulting from rift propagating at right angles to the basement structural grain of late Paleozoic orogeny and older Phase 1 rifts.

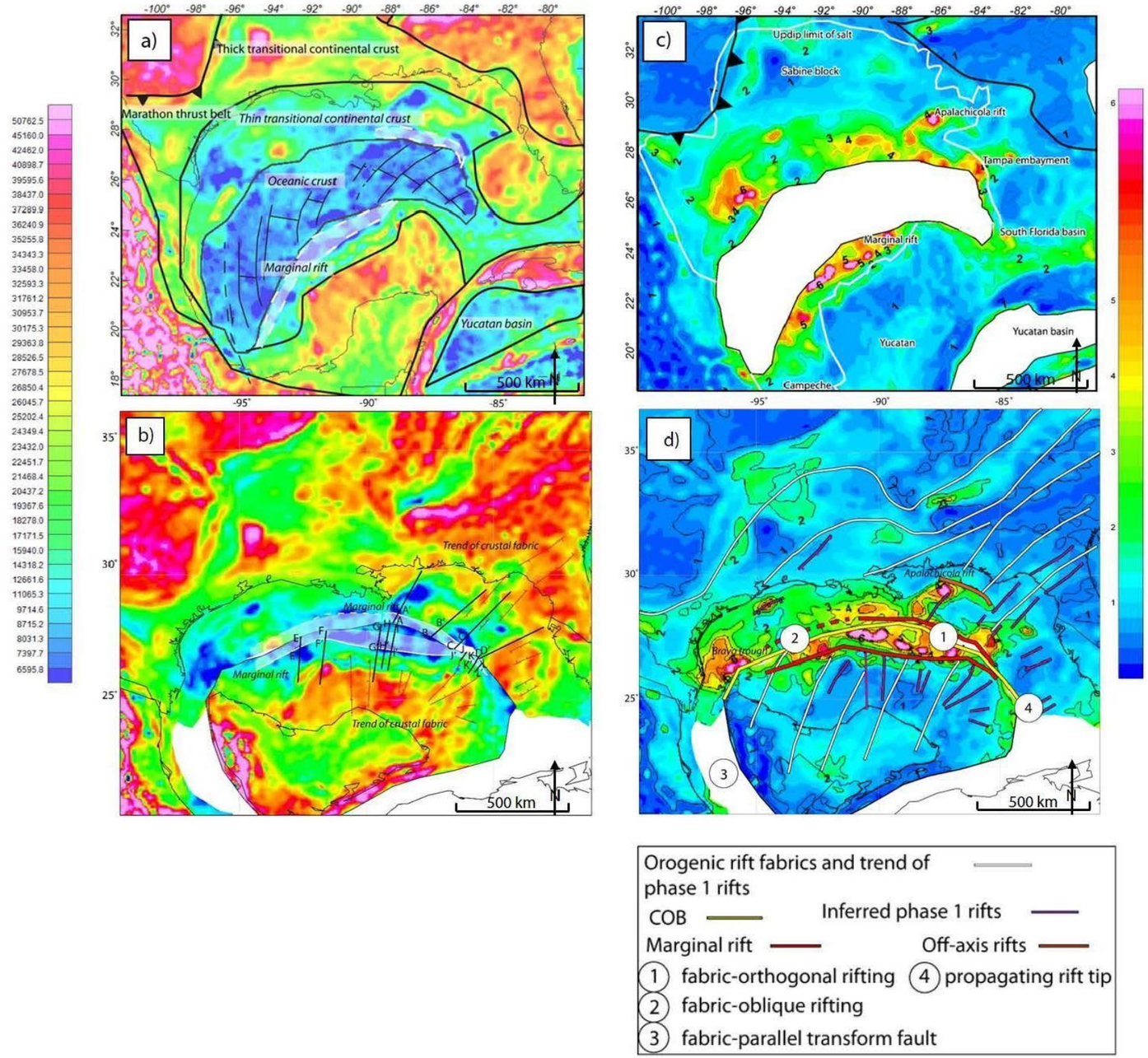
a)
Thick transitional continental crust
Marathon thrust belt
Thin transitional continental crust
Oceanic crust
Marginal rift
Yucatan basin
500 km
b)
Trend of crustal fabric
Marginal rift
Gulf
Marginal rift
Trend of crustal fabric
500 km
c)
Updip limit of salt
Sabine block
Apalachicola rift
Tampa embayment
South Florida basin
Marginal rift
Yucatan
Yucatan basin
Campeche
500 km
d)
Apalachicola rift
Bravo trough
500 km
Orogenic rift fabrics and trend of phase 1 rifts
COB
Inferred phase 1 rifts
Marginal rift
Off-axis rifts
1 fabric-orthogonal rifting
4 propagating rift tip
2 fabric-oblique rifting
3 fabric-parallel transform fault

A plot based on a worldwide compilation of rift beta factors to the orientation of basement fabric modified from Reuber and Mann (2019) shows that rifts with low beta factors correlate with rift-parallel fabric orientations while rifts with higher beta factors correlate with rift-orthogonal orientation (Figure 4.17a). In this chapter I measured the marginal rift orientation relative to the preexisting crustal fabrics inferred from gravity and magnetic maps and estimated the beta factor (Figure 4.17b) from a 3D crustal model by Liu et al. (2020).

Seven out of eight measurements for the GOM are within the rift orthogonal orientation and support the younger crosscutting relation of the Phase 2 rifts with the older Phase 1 rifts. One outlier measurement from the most eastern GOM shows more rift parallel characteristics on the plot. For this outlier measurement, the angle to this fabric is 49° and the beta factor is two.

Figure 4.17. a) Plot of beta factor values versus angle of orientation modified from Reuber and Mann (2019) to support their hypothesis that rifts that form perpendicular to the trends of basement crustal fabrics require more prolonged and intensive stretching (i.e., higher, observed beta factors in the 4-5 range) compared to those rifts that form parallel to the trends of crustal fabrics (i.e., lower, observed beta factors in the range of 2-3). b) Beta factor map produced by a 3D crustal model by gravity inversion (Chapter 3, this dissertation). The red lines are the late Paleozoic orogenic and Phase 1 late Triassic-early Jurassic rift fabrics interpreted from potential fields data that define the overall crustal fabric of the area. The angle between these crustal trends and the trends of the marginal rift system are shown for three locations for Florida rifted margin and range from 49-100°. The angle between these crustal trends and the trends of the marginal rift system are shown for three locations for the Yucatan rifted margin and range from 77-90°. The wider zone of rifting with higher beta factors of 4-5 in the northeastern GOM is consistent with more intensive stretching in this area to thin the crust to the point of formation of a late Jurassic oceanic spreading ridge.

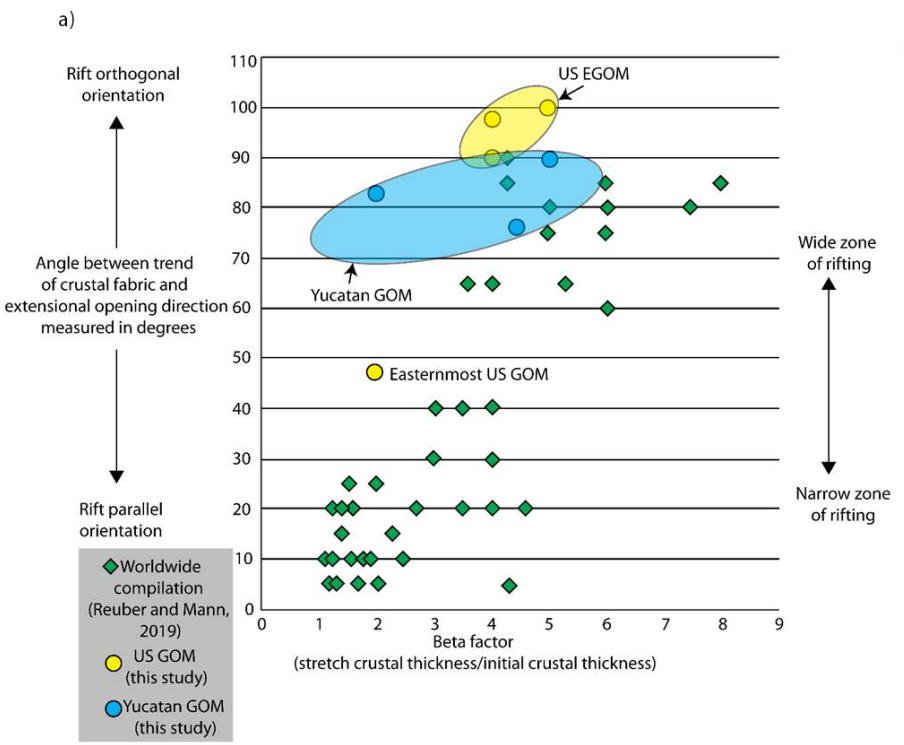
a)
Rift orthogonal orientation
Angle between trend of crustal fabric and extensional opening direction measured in degrees
Rift parallel orientation
US EGOM
Yucatan GOM
Easternmost US GOM
Wide zone of rifting
Narrow zone of rifting
Beta factor
(stretch crustal thickness/initial crustal thickness)
Worldwide compilation (Reuber and Mann, 2019)
US GOM (this study)
Yucatan GOM (this study)

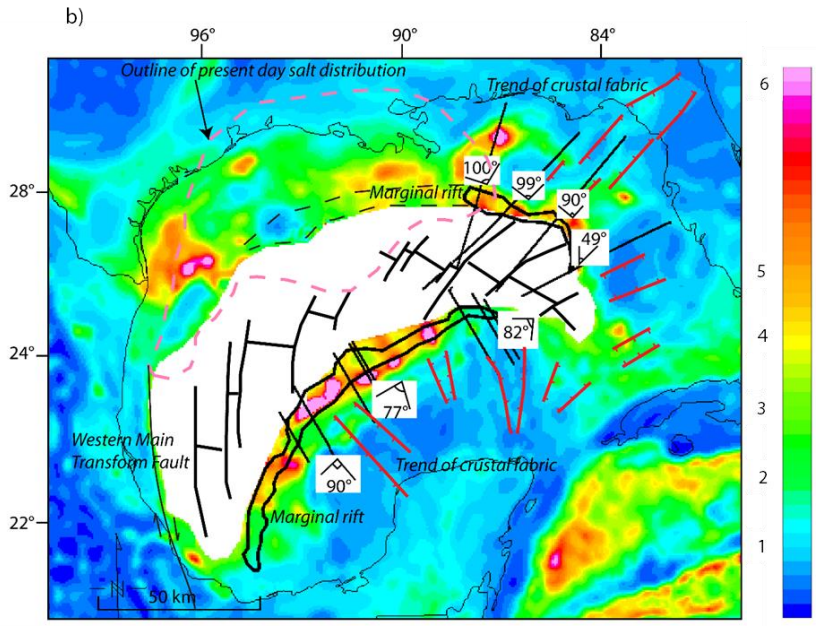
b)
96°
90°
84°
28°
24°
22°
Outline of present day salt distribution
Trend of crustal fabric
Marginal rift
100°
99°
90°
49°
82°
77°
90°
Western Main Transform Fault
Trend of crustal fabric
Marginal rift
50 km
6
5
4
3
2
1

4.4.5. Testing models of crustal structure and the tectonic origin of the marginal rift zone.

I use gravity modeling to support the sediment- or volcaniclastic-filled nature of the GOM marginal rift system. My gravity modeling shows that the rift infill has an estimated density of 2.6 g/cc that is consistent with clastic or volcaniclastic origin (Figure 4.5a) – rather than along narrow, fault-bounded belt of exhumed, higher-density mantle (Figure 4.5b) or lower continental crust (Figure 4.5c) as proposed by previous workers.

The characteristic low gravity and magnetic signature of the GOM marginal rift system is not a surprising result given the 1-9 km stratigraphic thicknesses that were observed from the seismic profiles described in this chapter (Figure 4.7-4.12). The presence of this sediment-filled rift adjacent to the late Jurassic oceanic crust underlying the central GOM supports the crustal necking mechanism and terminology as proposed by Peron-Pinviidic et al. (2019) for other circum-Atlantic, rifted margins (Figure 4.5a). Replacing the area of marginal rift with serpentinized mantle with a density of 2.8 g/cc (Lutz et al., 2018) results in a higher gravity response and larger modeled gravity misfit as compared to the better gravity fits using a sediment or volcaniclastic-filled rift (Figure 4.18).

SDRs have been proposed from the interpretation of seismic reflection and gravity data from the northern GOM by various authors including Imbert (2005), Kneller and Johnson (2011); Rowan (2014); Eddy et al. (2014) and Liu et al. (2019). As described in Chapter 2, the southern SDR in the NE GOM is adjacent to the marginal rift to the landward direction and therefore would have formed prior to the marginal rift – likely in the Late Triassic based on regional geological

inferences. This pre-rift SDR is less than 10 km in thickness and localized and does not appear to have any equivalent SDR on the southern GOM rifted margin on the Yucatan Peninsula.

Figure 4.18. a) 2D gravity model along the seismic profile in c by assuming the density for marginal rift is 2.6 g/cc as previously shown and discussed in Figure 4.6D. b) 2D gravity model along the seismic profile in c by replacing marginal rift with exhumed mantle density of 2.8 gm/cm3 taken from Lutz et al. (2018). The computed gravity anomaly using this inferred shape of the exhumed mantle from Pindell et al. (2014) and Curry et al. (2018) is higher than the gravity anomaly resulting from a sediment-filled marginal rift as proposed in this chapter. c) Regional seismic profile along A-A' in the NE GOM also shown in Figure 4.6a that supports the presence of a sediment-filled marginal rift.

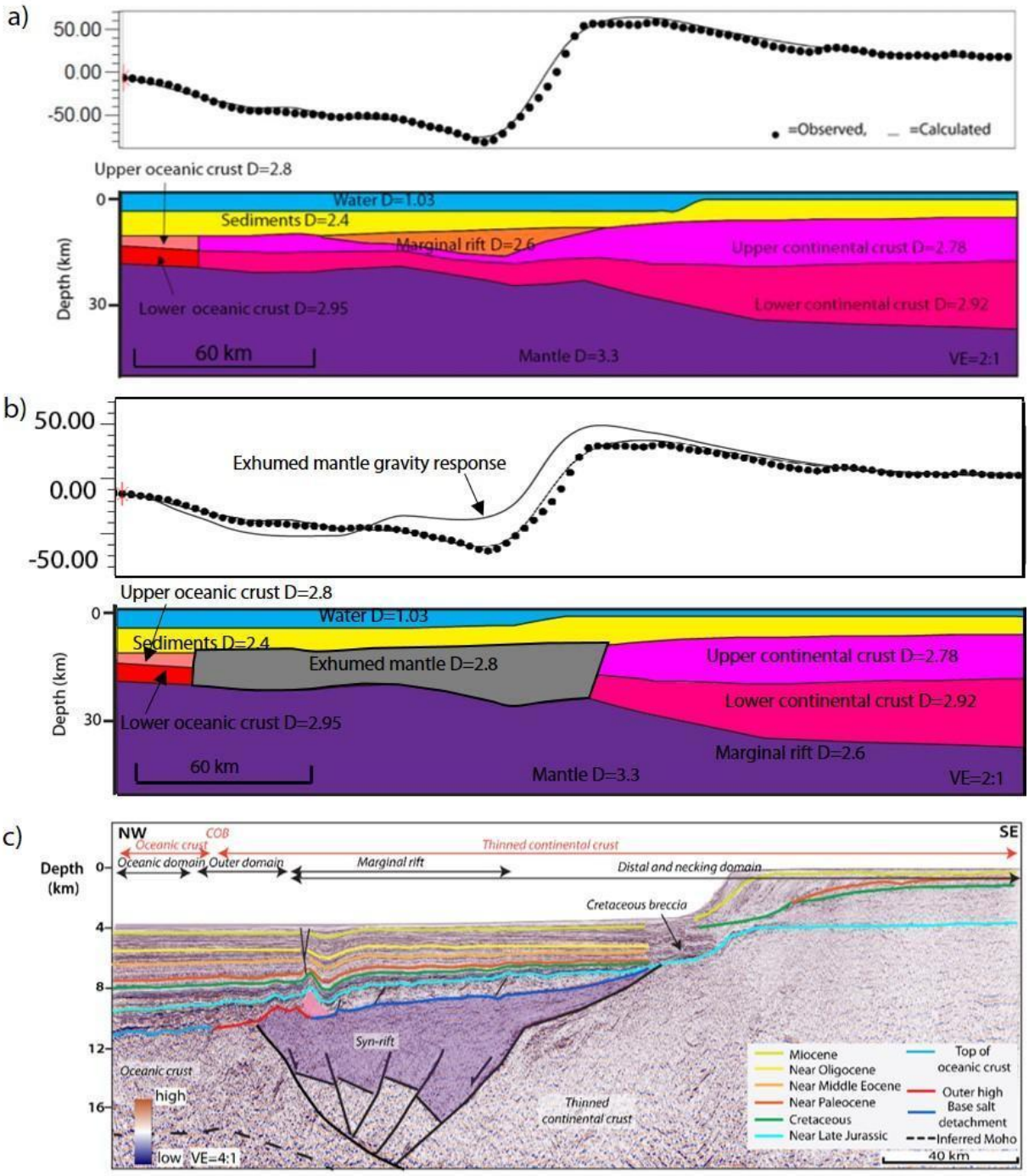
a)
50.00
0.00
-50.00
=Observed, _ =Calculated
Upper oceanic crust D=2.8
Water D=1.03
Sediments D=2.4
Marginal rift D=2.6
Upper continental crust D=2.78
Lower oceanic crust D=2.95
Lower continental crust D=2.92
Depth (km)
0
30
60 km
Mantle D=3.3
VE=2:1
b)
50.00
0.00
-50.00
Exhumed mantle gravity response
Upper oceanic crust D=2.8
Water D=1.03
Sediments D=2.4
Exhumed mantle D=2.8
Upper continental crust D=2.78
Lower continental crust D=2.92
Lower oceanic crust D=2.95
Marginal rift D=2.6
Depth (km)
0
30
60 km
Mantle D=3.3
VE=2:1
c)
NW
SE
COB
Oceanic crust
Thinned continental crust
Oceanic domain
Outer domain
Marginal rift
Distal and necking domain
Cretaceous breccia
Depth (km)
0
4
8
12
16
Syn-rift
Oceanic crust
high
low
VE=4:1
Thinned continental crust
Miocene
Near Oligocene
Near Middle Eocene
Near Paleocene
Cretaceous
Near Late Jurassic
Top of oceanic crust
Outer high
Base salt detachment
Inferred Moho
40 km

4.5. Conclusions

This study used 12 seismic reflection profiles and seismic refraction studies from previous workers to develop two, regional 2D gravity models of both conjugate margins of the GOM. The seismic interpretation of the industry 2D seismic reflection transects shows that the GOM marginal rift system extends over 600 km on the Yucatan margin and 380 km on the northeastern GOM. The result of the gravity modeling improved the understanding of the sedimentary fill composition in the circum-GOM marginal rift system as well as the nature of the crust associated with features of this necked region of the rifted, continental margin.

Based on the gravity model, the inferred composition of the marginal rift system is volcaniclastics according to the modeled density of 2.6 g/cc. The sequential structural restoration result suggests the salt present in the marginal rift area accumulated as the result of in-situ deposition and by accumulation of salt from downslope sliding along salt rollers. These observations support the tectonic explanation of crustal necking as proposed by Peron-Pinviidic et al. (2019) from other rift settings in the circum-Atlantic Ocean (Figure 4.5a) rather than models proposed by previous workers in the GOM for the exhumation of the mantle (Figure 4.5b) or lower continental crust (Figure 4.5c).

4.6 Bibliography

Brune, S., Heine, C., Clift, P.D., Pérez-Gussinyé, M., 2017. Rifted margin architecture and crustal rheology: Reviewing Iberia-Newfoundland, Central South Atlantic, and South China Sea. Mar. Pet. Geol. 79, 257–281.

Buck, W.R., 1991. Models of continental lithospheric extension. J. Geophys. Res. 96, 20161–20178.

Buck, W.R., 1988. Flexural rotation of normal faults. Tectonics 7, 959–973.

Cawood, A.J., Ferrill, D.A., Morris, A.P., Norris, D., McCallum, D., Gillis, E., Smart, K.J., 2021. Tectonostratigraphic evolution of the Orphan Basin and Flemish Pass region – Part 1: Results from coupled kinematic restoration and crustal area balancing. Mar. Pet. Geol. 128, 105042.

Curry, M.A.E., Peel, F.J., Hudec, M.R., Norton, I.O., 2018. Extensional models for the development of passive-margin salt basins, with application to the Gulf of Mexico. Basin Res. 30, 1180–1199.

Eddy, D.R., Avendonk, H.J.A. Van, Christeson, G.L., Norton, I.O., Karner, G.D., Johnson, C.A., Snedden, J.W., 2014. Deep crustal structure of the northeastern Gulf of Mexico: Implications for rift evolution and seafloor spreading. Journal of Geophysical Research : Solid Earth 1–21.

Erlich, R.N., Pindell, J., 2020. Crustal origin of the West Florida Terrane, and detrital zircon provenance and development of accommodation during initial rifting of the southeastern Gulf of Mexico and western Bahamas. In Davison, I., Hull, J.F. and Pindell, J. (eds), The basins, orogens, and evolution of the southern Gulf of Mexico and northern Caribbean, Geological Society, London, Special publications, 504.

Filina, I., Hartford, L., 2021. Subsurface structures along western Yucatan from integrated geophysical analysis. Mar. Pet. Geol. 104964.

Finn, C., Pilkington, M., Cuevas, A., Hernandez, I., Urrutia, J., 2001. New digital magnetic anomaly database for North America. Leading Edge, v.20, 8, 870-872.

Franke, D., Barckhausen, U., Baristeas, N., Engels, M., Ladage, S., Lutz, R., Montano, J., Pellejera, N., Ramos, E.G., Schnabel, M., 2011. The continent-ocean transition at the southeastern margin of the South China Sea. Mar. Pet. Geol. 28, 1187–1204.

Frederick, B.C., Blum, M.D., Snedden, J.W., and Fillon, R.H., 2020. Early Mesozoic synrift Eagle Mills Formation and coeval siliciclastic sources, sinks, and sediment routing, northern Gulf of Mexico basin, GSA Bulletin, 1-20.

Galloway, W.E., 2008. Chapter 15: Depositional evolution of the Gulf of Mexico sedimentary basin, in: Miall, A.D. (Ed.), *Sedimentary Basins of the World*. Elsevier, pp. 505–549.

Gomez, E., Doe, M., Villarroel, S., Noel, K., Ysaccis, R., Kornpihl, D., El-toukhy, M., Forrest, G., 2018. Recent Yucatan seismic survey revealing a new frontier for exploration in the Gulf of Mexico #30582. AAPG Search and Discovery.

Haupert, I., Manatschal, G., Decarlis, A., Unternehr, P., 2016. Upper-plate magma-poor rifted margins: Stratigraphic architecture and structural evolution. Mar. Pet. Geol. 69, 241–261.

Hudec, Michael R., Jackson, M.P. A., Peel, F.J., 2013. Influence of deep Louann structure on the evolution of the northern Gulf of Mexico. Am. Assoc. Pet. Geol. Bull. 97, 1711–1735.

Hudec, M.R., Norton, I.O., 2019. Upper Jurassic structure and evolution of the Yucatán and Campeche subbasins, southern Gulf of Mexico. Am. Assoc. Pet. Geol. Bull. 103, 1133–1151.

Hudec, M.R., Dooley, T.P., Peel, F.J., Soto, J.I., 2019. Controls on the evolution of passive-margin salt basins: Structure and evolution of the Salina del Bravo region, northeastern Mexico, GSA Bulletin, v.132, no.5/6, 997-1012.

Hunter, I., 2014. Origin and development of the Apalachicola Basin. University of Alabama, unpublished MS thesis, 1-93.

Ibrahim, A.K., Latham, J.C.G., Buffler, R.T., 1981. Crustal structure in Gulf of Mexico from OBS refraction and multichannel reflection data. Am. Assoc. Pet. Geol. Bull. 65, 1207–1229.

Imbert, P., Philippe, Y., 2005. The Mesozoic opening of the Gulf of Mexico — Part 2: Integrating seismic and magnetic data into a general opening model: 25th Annual Bob F. Perkins Research Conference: Petroleum Systems of Divergent Continental Margin Basins, 1151–1189.

Kenning, J.J., Mann, P., 2021. Regional thermal maturity modelling of hydrocarbons along the deep-water Yucatan margin, southern Gulf of Mexico. In Davison, I., Hull, J., and Pindell, J., eds, *The Basins, Orogens, and Evolution of the southern Gulf of Mexico and northern Caribbean*, Geological Society of London, Special Publications, 504, 203–231.

Klitgord K.D., Schouten, H., 1986. Plate kinematics of the central Atlantic. In Vogt, P.R., and Tucholke, B.E., eds., *The Geology of North America*, vol M, The western North Atlantic Region: Geological Society of America.

Kneller, E.A., Johnson, C.A., 2011. Plate kinematics of the Gulf of Mexico based on integrated observations from the Central and South Atlantic. Gulf Coast Assoc. Geol. Soc. Trans. 61, 283–299.

Kukla, P.A., Strozyk, Ft., Mohriak, W.U., 2018. South Atlantic salt basins- Witnesses of complex passive margin evolution. Gondwana Research, 53, 41-57.

Lawton, T.F., Bradford, I.A., Vega, F.J., Gehrels, G.E., Amato, J.M., 2009. Provenance of Upper Cretaceous-Paleogene sandstones in the foreland basin system of the Sierra Madre Oriental,

northeastern Mexico, and its bearing on fluvial dispersal systems of the Mexican Laramide Province. Bull. Geol. Soc. Am. 121, 820–836.

Lin, P., 2018. Crustal structure and tectonostratigraphic evolution of the eastern Gulf of Mexico Basin. Unpublished PhD dissertation, University of Houston, 154 p.

Lin, P., Bird, D.E., Mann, P., 2019. Crustal structure of an extinct, late Jurassic-to-earliest Cretaceous spreading center and its adjacent oceanic crust in the eastern Gulf of Mexico. Mar. Geophys. Res.

Lister, G.S., Etheridge, M.A., Symonds, P.A., 1991. Detachment models for the formation of passive continental margins. Tectonics 10, 1038–1064.

Liu, M., Filina, I., Mann, P., 2019. Crustal structure of Mesozoic rifting in the northeastern Gulf of Mexico from integration of seismic and potential fields data. Interpretation 7, T857–T867.

Liu, M., Bird, D.E., Mann. P., 2020. Distribution and thickness of crustal types of the Greater Gulf of Mexico region based on constrained 3D gravity inversion, AGU Fall Meeting poster.

Lutz, R., Franke, D., Berglar, K., Heyde, I., Schreckenberger, B., Klitzke, P., Geissler, W.H., 2018. Evidence for mantle exhumation since the early evolution of the slow spreading Gakkel Ridge, Arctic Ocean. Journal of Geodynamics, 154-165.

Marton, G., Buffler, R.T., 1994. Jurassic reconstruction of the Gulf of Mexico Basin. Int. Geol. Rev. 36, 545–586.

Marton, G.L., Buffler, R.T., 2016. Jurassic-Cretaceous tectonic evolution of the southeastern Gulf of Mexico, Constraints on the style and timing of Gulf of Mexico rift-drift development. AAPG Search and Discovery. Article. 26, 701–725.

McKenzie, D., 1978. Some remarks on the development of sedimentary basins. Earth Planet. Sci. Lett. 40, 25–32.

Minguez, D.E. Gerald Hensel, E.A.E.J., 2020. A fresh look at Gulf of Mexico Tectonics: Testing rotations and breakup mechanisms from the perspective of seismically constrained potential fields modelling and plate kinematics. Interpretation.

Mohriak, W.U., Nemcok, M., Enciso, G., 2008. South Atlantic divergent margin evolution: rift-border uplift and salt tectonics in the basins of SE Brazil. In: Pankhurst RJ, Trouw RAJ, Brito Neves BB, de Wit MJ (eds) *West Gondwana Pre-Cenozoic Correlations across the South Atlantic region*, vol 294. Geological Society of London, Special Publication, 365–398.

Mohriak, W., 2019. Rifting and salt deposition on continental margins: Differences and similarities between the Red Sea and the South Atlantic sedimentary basins, in Rasul N.M.A and Stewart I.C.F.(editor) *Geological Setting, Palaeoenvironment and Archaeology of the Red Sea*. Springer International Publishing.

Morley, C.K., 2009. Geometry and evolution of low-angle normal faults (LANF) within a Cenozoic high-angle rift system, Thailand: Implications for sedimentology and the mechanisms of LANF development. Tectonics 28, 1–30.

Nguyen, L.C., Mann, P., 2016. Gravity and magnetic constraints on the Jurassic opening of the oceanic Gulf of Mexico and the location and tectonic history of the Western Main transform fault along the eastern continental margin of Mexico. *Interpretation* 4, SC23–SC33.

Péron-Pinvidic, G., Manatschal, G., 2009. The final rifting evolution at deep magma-poor passive margins from Iberia-Newfoundland: A new point of view. Int. J. Earth Sci. 98, 1581–1597.

Peron-Pinvidic, G., Manatschal, G., Osmundsen, P.T., 2013. Structural comparison of archetypal Atlantic rifted margins: A review of observations and concepts. Mar. Pet. Geol. 43, 21–47.

Peron-Pinvidic, G., Osmundsen, P.T., 2016. Architecture of the distal and outer domains of the Mid-Norwegian rifted margin: Insights from the Ran-Gjallar ridge system. *Marine and Petroleum Geology*, v. 77, 280-299.

Pilcher, R.S., Murphy, R.T., Ciosek, J.M., 2014. Jurassic raft tectonics in the northeastern Gulf of Mexico. Spec. Sect. Salt Tectonics, Interpretation, SM39–SM55.

Pindell, J., Graham, R., Horn, B., 2014. Rapid outer marginal collapse at the rift to drift transition of passive margin evolution, with a Gulf of Mexico case study. Basin Research, v26, pp. 1-25.

Pindell, J., Miranda C, E., Cerón, A., Hernandez, L., 2016. Aeromagnetic map constrains Jurassic-Early Cretaceous synrift, break up, and rotational seafloor spreading history in the Gulf of Mexico, in: Lowery, C.M., Snedden, J.W., Rosen, N.C. (Eds.), *Mesozoic of the Gulf Rim and Beyond: New Progress in Science and Exploration of the Gulf of Mexico Basin*. SEPM Society for Sedimentary Geology, pp. 123–153.

Pindell, J., Weber, B., Hale-Erlich, W., Cossey, S., Bitter, M., Molina Garza, R., Graham, R., Erlich, R.N., 2020. Strontium isotope dating of evaporites and the breakup of the Gulf of Mexico and Proto–Caribbean Seaway. South. Cent. Mex. Basement Fram. Tecton. Evol. Proven. Mesozoic–Cenozoic Basins 2546.

Pindell, James L, Kennan, L., 2009. Tectonic evolution of the Gulf of Mexico, Caribbean and northern South America in the mantle reference frame : an update, in: James, K.H., Lorente, M.A., Pindell, J L (Eds.), *The Origin and Evolution of the Caribbean Plate*: Geological Society of London Special Publications 328. Geological Society of London, London, UK, pp. 1–55.

Planke, S., Eldholm, O., 1994. Seismic response and construction of seaward dipping wedges of flood basalts: Vøring volcanic margin. J. Geophys. Res. 99, 9263–9278.

Pulham, A.J., Peel, F.J., Delph, B., Nicholson, T., Wu, J., 2019. The age of the Louann Salt;Insights from historic isotopic analyses in salt stocks from the onshore Interior Salt Basins of the Northern Gulf of Mexico, 37th Annual GCSSEPM Foundation Perkins-RosenResearch Conference 64–66.

Reuber, K., Mann, P., 2019. Control of Precambrian-To-Paleozoic orogenic trends on along-strike variations in Early Cretaceous continental rifts of the South Atlantic Ocean. Interpretation 7, 1–80.

Rowan, M.G., 2014. Passive-margin salt basins: Hyperextension, evaporite deposition, and salt tectonics, Basin Res., 26, 154-182.

Rowan, M.G., 2018. Conundrums in loading-driven salt movement. J. Struct. Geol. 0–1.

Rowan, M.G., 2020. The outer domain of the southern Gulf of Mexico margin: along-strike variations in the continent-ocean transition and salt distribution, AAPG Hedberg abstract.

Salvador, A., 1987. Late Triassic-Jurassic paleogeography and origin of Gulf of Mexico basin. Am. Assoc. Pet. Geol. Bull. 71, 419–451.

Sandwell, D.T., Muller, R.D., Smith, W.H.F., Garcia, E., Francis, R., 2014. New global marine gravity model from CryoSat-2 and Jason-1 reveals buried tectonic structure. Science. 346, 65–67.

Sanford, J.C., Snedden, J.W., Gulick, S.P.S., 2016. The Cretaceous-Paleogene boundary deposit in the Gulf of Mexico: Large-scale oceanic basin response to the Chicxulub impact. J. Geophys. Res. Solid Earth 121, 1240–1261.

Schlische, R.W., Withjack, M.O., Olsen, P.E., 2003. Relative timing of CAMP, rifting, continental breakup, and basin inversion: Tectonic significance. Geophys. Monogr. Ser. 136, 33–59.

Schlüter, H.U., Hinz, K., Block, M., 1996. Tectono-stratigraphic terranes and detachment faulting of the South China Sea and Sulu Sea. Marine Geology 130, 39-51.

Sclater, J.G., Christie, P.A.F., 1980. Continental stretching: An explanation of the post-Mid-Cretaceous subsidence of the central North Sea Basin. J. Geophys. Res. Solid Earth 85, 827 3711–3739.

Smith, D.L., Lord, K.M., 1997. Tectonic evolution and geophysics of the Florida Basement, in Geology of Florida, edited by A. F. Randazzo, and D. S. Jones, 13-26.

Snedden J.W., Norton I., Christeson G., Sanford J., 2014. Interaction of deepwater deposition and a mid-ocean spreading center, eastern Gulf of Mexico Basin, USA. GCAGS Trans 64, 371–383.

Steier, A., Mann, P., 2019. Late Mesozoic gravity sliding and Oxfordian hydrocarbon reservoir potential of the northern Yucatan margin. Mar. Pet. Geol. 103, 681–701.

Storey, M.L., 2020. Tectonic setting, structure, and seismic stratigraphy of the Apalachicola Rift and its overlying sag basin in the northeastern Gulf of Mexico, unpublished MS thesis, University of Houston, 1-102 p.

Talwani, M., Worzel, J.L., Landisman, M., 1959. Rapid gravity computations for two-dimensional bodies with application to the Mendocino submarine fracture zone. Journal of geophysical research, v. 64, No. 1, 49-59.

Van Avendonk, H.J.A., Christeson, G.L., Norton, I.O., Eddy, D.R., 2015. Continental rifting and sediment infill in the northwestern Gulf of Mexico. Geology 43, 631–634.

Wernicke, B., 1981. Low-angle normal faults in the Basin and Range Province: Nappe tectonics in an extending orogen. Nature 291, 645–648.

Xiao, L., Zhao, J.W., Liu, H.S., Xiao, Z.Y., Morgan, J., Gulick, S., Kring, D., Claeys, P., Riller, U., 2017. U/Pb geochronology of devonian and older Paleozoic beds in the southeastern Maya block, Central America: Its affinity with Peri-Gondwanan terranes. Lunar Planet. Sci. 1–2.

The following chapter has been submitted to the Journal of Applied Geophysics.

CHAPTER 5: INVERSE MODELING AND INTERPRETATION OF FULL TENSOR GRAVITY (FTG) ANOMALIES IMPROVES SALT CANOPY GEOMETRIES IN THE NORTHERN GULF OF MEXICO

5.1 Introduction

The continental crust of the northern Gulf of Mexico (GOM) formed as a rifted margin prior to the formation of a Mid-to-Late Jurassic oceanic basin that now underlies the central GOM. The northern GOM is now filled with up to 15 km of sedimentary rocks and with complex structures caused by salt halokinesis (Figure 5.1). Seismic imaging through salt is complicated by salt structures and layer geometries, as well as high-velocity contrasts between salt and surrounding sedimentary rocks (Routh et al., 2001). Incident seismic energy arriving at these velocity contrasts is commonly reflected and scattered along the irregular-shaped top salt surface and is not able to penetrate into the deeper section so that the seismic reflections cannot be easily interpreted (Simmons, 1992; Coburn, 1999; Etgen, 2004). There are velocity model limitations around salt diapirs with steeply-dipping sides and adjacent sedimentary horizons, including complex, internal structuring of salt bodies (Jones & Davison, 2014). Thus, FTG data provides a new constraint for mapping complex, subsurface architecture produced by remobilized salt (Routh et al., 2001).

Gravity models, combined with wells and seismic reflection data, have been previously used in the GOM to map deeper structures and crustal structure (e.g., Schenk et al., 1996; Parsons et al., 2004; Bird et al., 2005; Filina et al., 2015; Liu et al., 2019). In addition to 2D forward models, 3D gravity models have been used for inverse modeling of base salt horizons in the GOM (Jorgensen

& Kisabeth, 2000; Routh et al., 2001). Full Tensor Gravity (FTG) data are used to further delineate the size, shape, and thickness of more subtle, localized density anomalies (Zhdanov et al., 2004), including small salt and karst bodies, which are often difficult to image with seismic data. For example, Jorgensen et al. (2011) inverted the base of allochthonous salt in a GOM 3D model using the Tzz component of FTG data to produce a salt isopach map. I used the Tzz component to invert the base salt layer and calculate the salt thickness to isolate the gravity anomalies produced solely by the salt masses. I then used the Txz and Tyz components to map the 3D salt geometries across a 19,134 km^2 area of the northwestern GOM.

Figure 5.1 The black polygon shows the location of the FTG dataset in the northwestern Gulf of Mexico (GOM). Pink polygons are mapped salt diapirs from Huffman et al. (2004). Salt bodies shown in white and labeled ab and cd correspond to the Txz and Tyz mapping results shown in Figure 5.4.

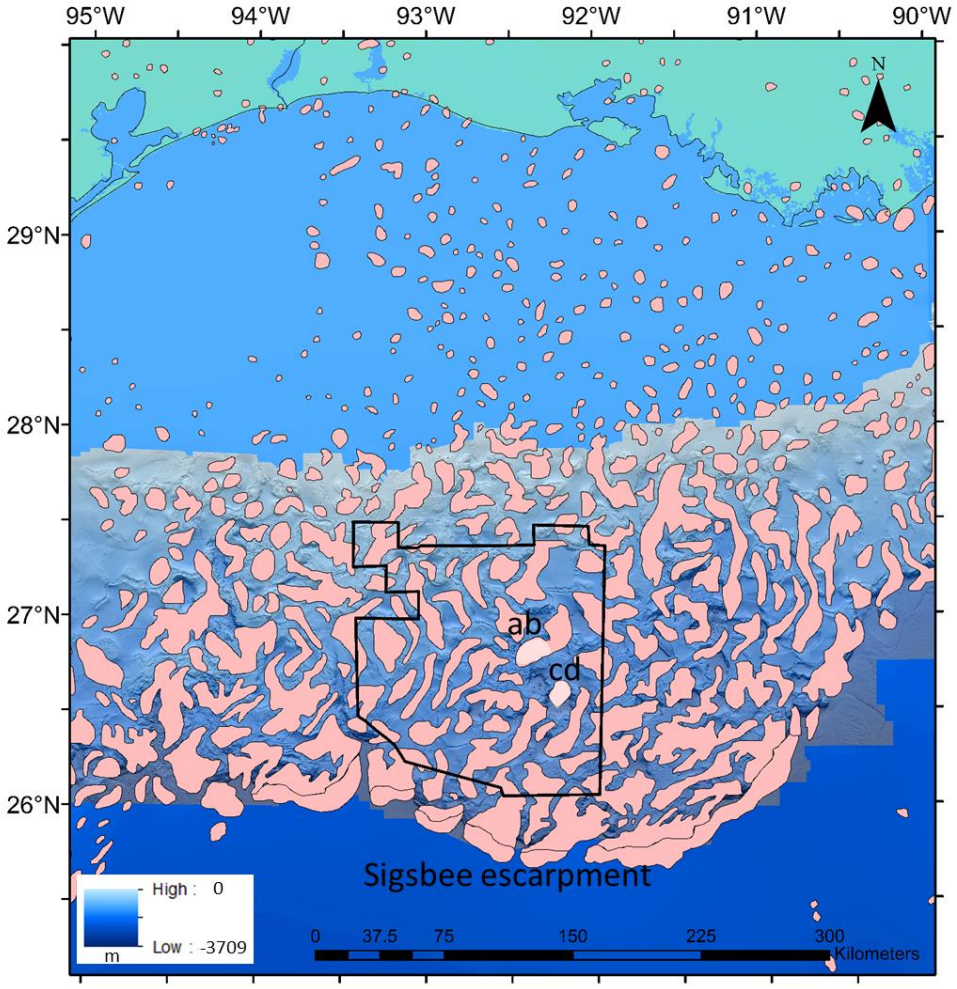

5.2 Data and methods

The top and base salt horizons were interpreted using depth converted PSDM (Pre Stack Depth Migrated) 2D multichannel seismic reflection data, the DeepFocus seismic survey, provided by Spectrum (now TGS) and acquired in 2007 (Figures 5.2a and 5.2b). The seismic data consist of a grid of NE- and NW-trending lines with an average spacing of 3 km with a shot interval is 37.5 m and a streamer length of 10 km. The top and base salt horizons were identified by applying commonly used criteria, such as seismic attribution analyses and tracing high amplitude reflections above reflection-free zones. Over the study area, salt canopies are shallower to the north and deeper near the edge of the Sigsbee escarpment (Figures 5.2a and 5.2b). For the comparison of base salt between the seismic interpretation and gravity inversion, this chapter used a seismic profile from the SuperCache dataset provided by Dynamic group. These seismic data were collected in 2012 with a streamer length of 15 km and a shot interval of 62.5 m and were depth migrated.

Figure 5.2 (a) Map of top of salt canopy from 2D seismic interpretations. (b) Base of salt canopy from 2D seismic interpretations. (c) Map of base of salt from 3D gravity inversion of FTG data. (d) Difference between seismic and gravity inverted base salt maps.

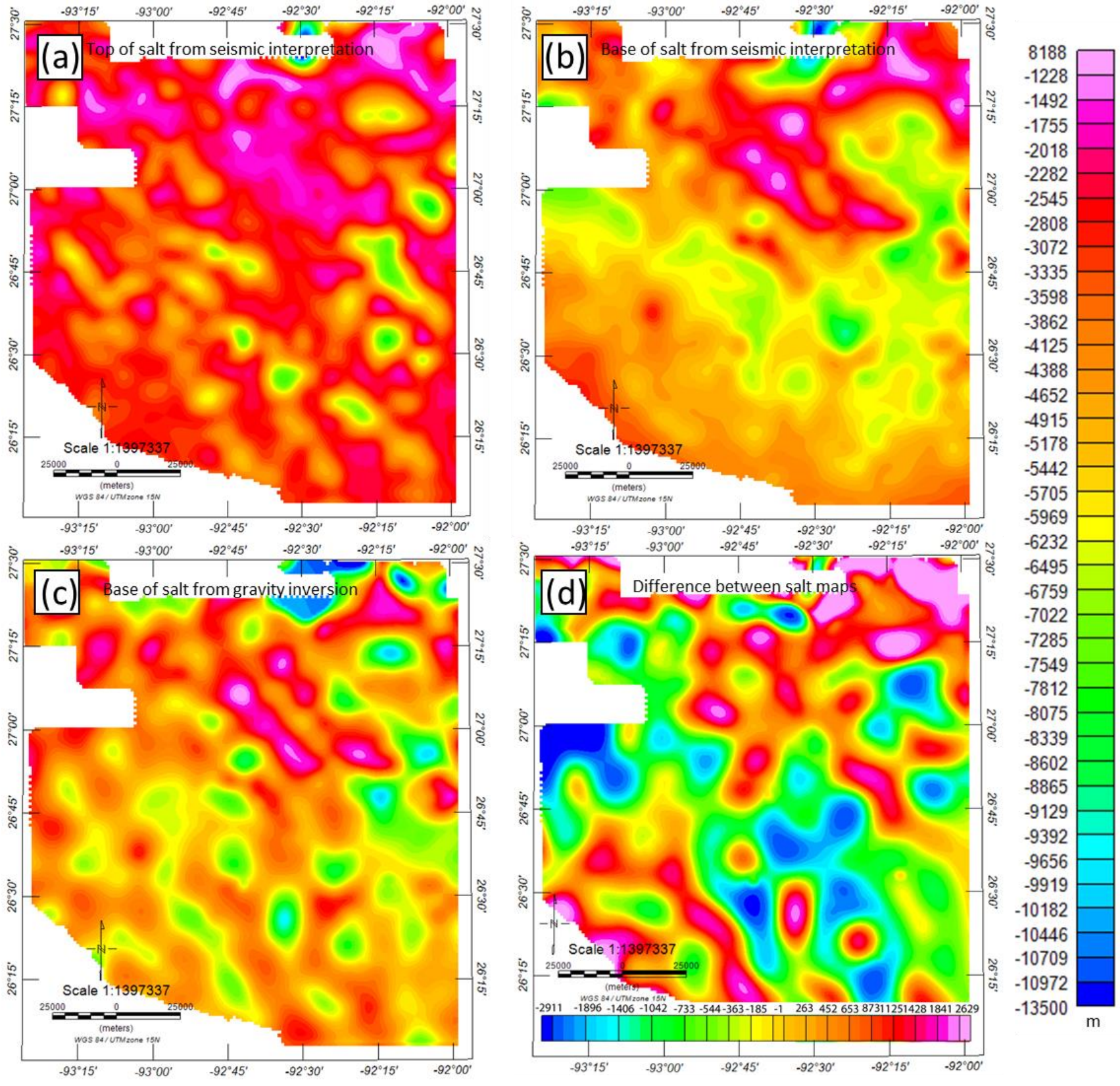
(a) Top of salt from seismic interpretation
(b) Base of salt from seismic interpretation
(c) Base of salt from gravity inversion
(d) Difference between salt maps
Scale 1:1397337
25000 0 25000
(meters)
WGS 84 / UTM zone 15N
-93°15' -93°00' -92°45' -92°30' -92°15' -92°00'
27°30' 27°15' 27°00' 26°45' 26°30' 26°15'
8188 -1228 -1492 -1755 -2018 -2282 -2545 -2808 -3072 -3335 -3598 -3862 -4125 -4388 -4652 -4915 -5178 -5442 -5705 -5969 -6232 -6495 -6759 -7022 -7285 -7549 -7812 -8075 -8339 -8602 -8865 -9129 -9392 -9656 -9919 -10182 -10446 -10709 -10972 -13500
m
-2911 -1896 -1406 -1042 -733 -544 -363 -185 -1 263 452 653 873 1125 1428 1841 2629

Sigsbee escarpment that forms the southern edge of the salt province (Figure 5.1). Traditional gravimeters measure the scalar of the field strength, Gz, or the square root of the sum of X-Y-Z vector components squared (Coburn, 1999). FTG data measures rates of change of each gravity vector field component (Tx, Ty, Tz, where T is gravitational force) in three dimensions (Figure 5.3). Of these nine-tensor components, five are independent (Txx, Tyy, Txy, Txz, Tyz) (e.g., Bell et al., 1997; Pawlowski, 1997; Mikhailov & Diament; Zuo & Hu, 2015). Tyz is the rate of gravitational change in the Z-direction of the Y-vector component, and Txz is the rate of gravitational change in the Z-direction of the X-vector component (Jorgensen et al., 2001; Oruc, 2010). Physically, Tzz (rate of change in Z-direction of the Z-component) points to the center of mass of the density source, and Txz and Tyz components produce minimum and maximum anomalies over density boundaries, such as faults or the edges of salt bodies.

The 3D gravity model consists of seven density layers: air, water, upper sediment, salt, lower sediment, crystalline crust, and upper mantle. The bathymetric surface, separating water and upper sediment layers, is compiled from the high-resolution bathymetry dataset of the U.S. Bureau of Ocean Energy Management (BOEM). As noted above, the top and base of the salt layers were interpreted using the 2D PSDM seismic grid (Figures 5.2a and b). The top of the salt canopy is a strong reflector with a positive amplitude across the study area. The base of the salt canopy is a weaker negative amplitude reflector and difficult to identify in places. Seismic attributes and geomorphologic features such as truncation of salt with underlying strata provided confidence in the seismic interpretation. The basement surface could not be mapped from the available seismic with high confidence due to image quality at deeper levels. Instead, a basement surface between lower sediment and crystalline crust layers was generated by integrating seismic refraction control (Ebeniro et al., 1988) with regional horizon grids (Laske et al., 2013; Straume et al., 2019). The

Moho surface was extracted from a regional gravity model (Liu et al., 2020). All layer densities were constant except for the sedimentary layers surrounding the salt canopies: 1.03 g/cc for water, 2.16 g/cc for the salt layer, 2.85g/cc for the crustal layer, and 3.3 g/cc for the upper mantle. This study used 45 density logs from wells near the Gulf coast to derive an exponential decay depth density function (D= 2.7-0.65*exp (-0.0002*depth)) for the sedimentary layers.

Three-dimensional forward and inverse calculations of potential fields data were based on frequency-domain techniques described by Cordell and Henderson (1968), Parker (1972), Bott (1973), and Li and Chouteau (1998). Three-dimensional inversions typically involve multiple iterations of automated calculation and examination of modeled results. This chapter used GM-SYS 3D within Seequent software package to perform these inversion calculations and the Tzz inversion, which includes a gravity structural inversion algorithm patented by Chavarria et al. (2006). The inversion process implemented a two-stage approach: fit longer wavelengths first, then focus on fitting shorter wavelengths. The 3D base salt structural inversion was computed, using both Tz gravity and Tzz FTG components, such that the RMS misfit between calculated and observed gravity and FTG data was minimized.

Gradients are organized into the north-east-down (NED) standard, which means that horizontal gradients are calculated from south-to-north and west-to-east, and the vertical gradient points down. Minima and maxima Txz and Tyz are located over boundaries formed by density contrasts, thus allowing salt geometries to be mapped directly from the FTG data. A 3D test model was built with a 16 x16 km low-density square basin (Figure 5.3b). Calculated Txz produces a minimum over the western edge of the basin and a maximum over the eastern edge; similarly, Tyz produces minima and maxima anomalies over the southern and northern edges of the salt body. Salt density (~2.16 g/cc) is typically lower than surrounding sedimentary rocks, which is analogous

to the basin test model, except the model uses a low-density block instead of a salt body. I then interpreted edges of salt bodies from Txz and Tyz components.

Figure 5.3 (a) Six components of the FTG dataset and comparison with salt canopy distribution in the area (lower left). (b) Simple 3D modeled density boundaries show how Txz and Tyz anomalies are calculated over source edges according to the NED standard. Ticks point toward the low-density side of the edges.

(a)

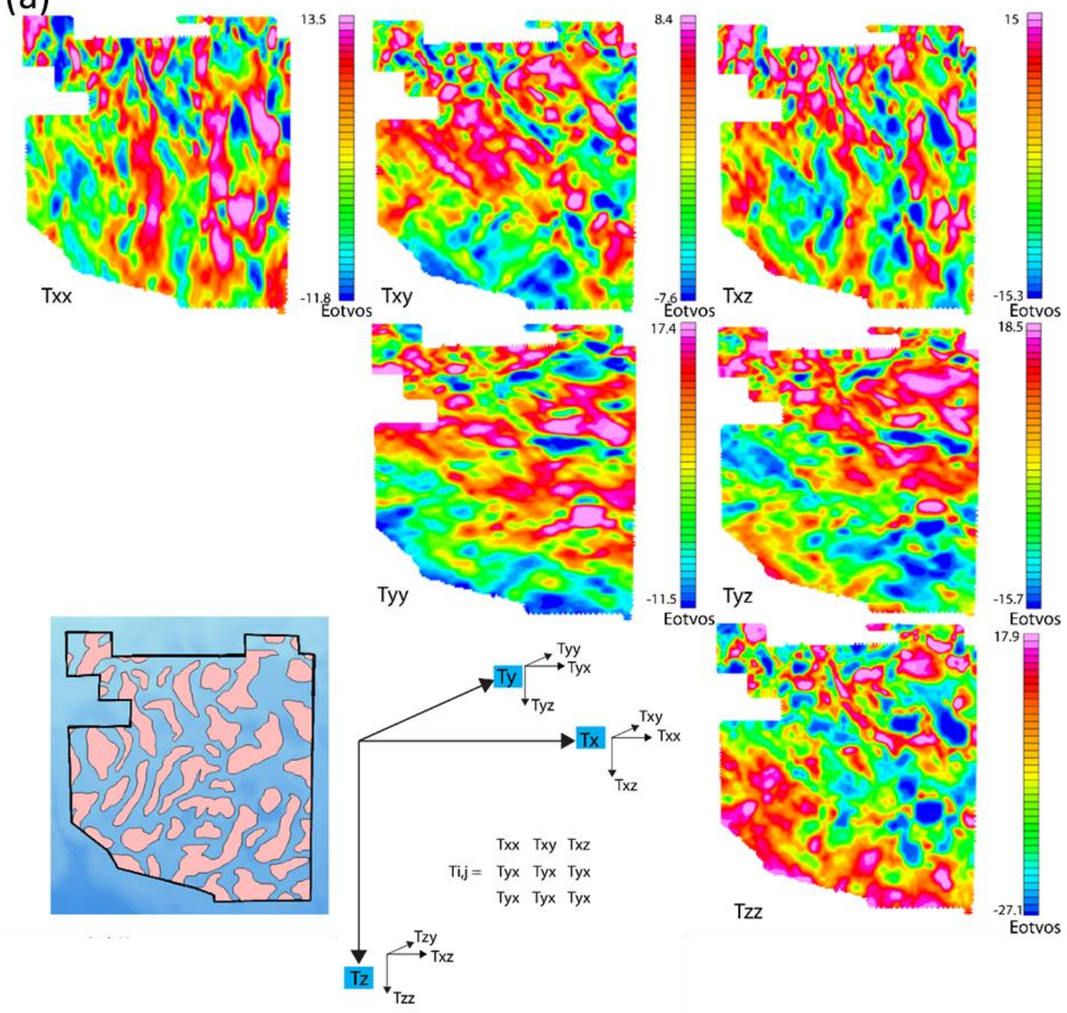
13.5
-11.8
Eotvos
Txx
8.4
-7.6
Eotvos
Txy
15
-15.3
Eotvos
Txz
17.4
-11.5
Eotvos
Tyy
18.5
-15.7
Eotvos
Tyz
17.9
-27.1
Eotvos
Tzz
Ty
Tyy
Tyx
Tyz
Tx
Txy
Txx
Txz
Tz
Tzy
Txz
Tzz
Ti,j =
Txx Txy Txz
Tyx Tyx Tyx
Tyx Tyx Tyx

(b)

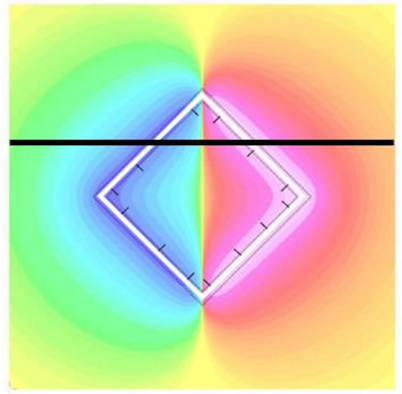
XZ

yz

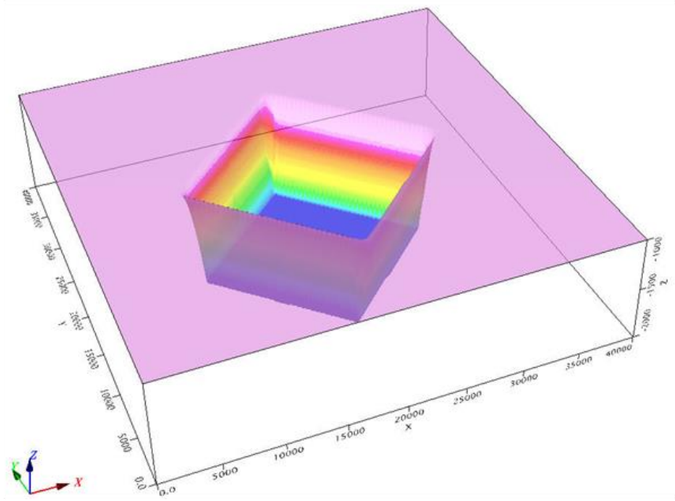

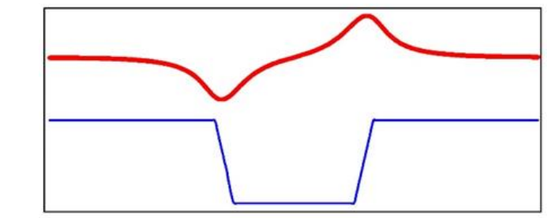
NED: Gradient calculated W-to-E or S-to-N

The last step was to integrate a 2D seismic interpretation with the base of salt inversion and Txz and Tyz interpretation results. The modeled base salt is a quantitative comparison with the seismic interpretation. The qualitatively mapped FTG components indicate horizontal density changes associated with diapir and lobe edges of the salt canopy.

5.3 Results and interpretation

The FTG inversion converged to RMS 0.05 Eotvos after 33 iterations, with a misfit mean and standard deviation of 0.75 and 2.75 Eotvos, respectively. Details of these results are provided in the supplementary material.

Tracing maxima and minima of Txz and Tyz components, I interpreted the edges of low-density sources (Figure 5.4). Interpreted salt edges from seismic data are located directly beneath Txz and Tyz anomalies, where, as stated above, Txz minima indicate low-density sources to the east, and Txz maxima indicate low-density sources to the west. Similarly, Tyz minima indicate the low-density sources to the north, and Tyz maxima indicate the low-density sources to the south. Anomalies **a** and **b** in Figure 5.4a and anomalies **c** and **d** in Figure 5.4b suggest two pairs of anomalies that highlight the edges of salt bodies.

Figure 5.4 Comparison of fault interpretations between FTG datasets and seismic reflection data. The NE-SW-oriented black line shows the location of seismic data (Figure 5). Letters **a**, **b**, **c**, **d** are anomaly pairs mapped along minima and maxima on Txz and Tyz maps. Ticks point towards low-density. (a) Faults interpretation from the Txz component are shown as white lines. (b) Faults interpretation from Tyz component are shown in green. (c) Overlay of fault interpretation from Txz and Tyz onto the gravity-inverted base of the salt map. Black line trends NE-SW.

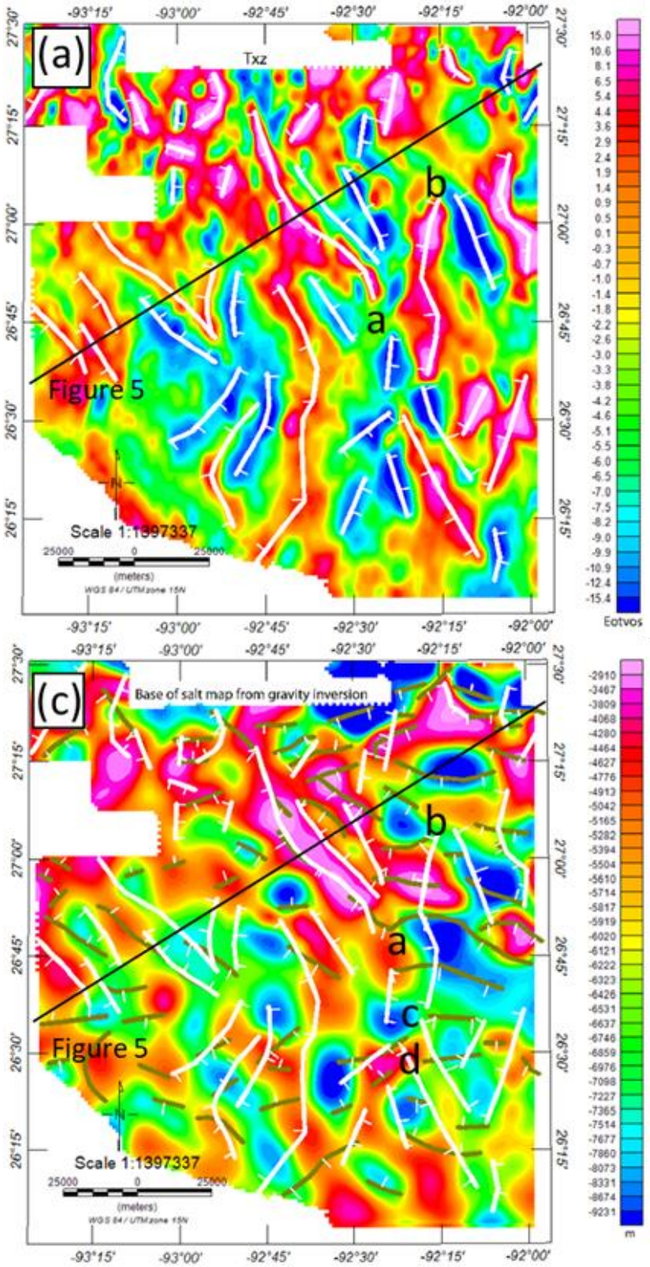
(a)
Txz
a
b
Figure 5
Scale 1:1997337
25000 0 25000
(meters)
WGS 84 / UTM zone 15N
-93°15' -93°00' -92°45' -92°30' -92°15' -92°00'
27°30' 27°15' 27°00' 26°45' 26°30' 26°15'
15.0 10.6 8.1 6.5 5.4 4.4 3.6 2.9 2.4 1.9 1.4 0.9 0.5 0.1 -0.3 -0.7 -1.0 -1.4 -1.8 -2.2 -2.6 -3.0 -3.3 -3.8 -4.2 -4.6 -5.1 -5.5 -6.0 -6.5 -7.0 -7.5 -8.2 -9.0 -9.9 -10.9 -12.4 -15.4
Eotvos

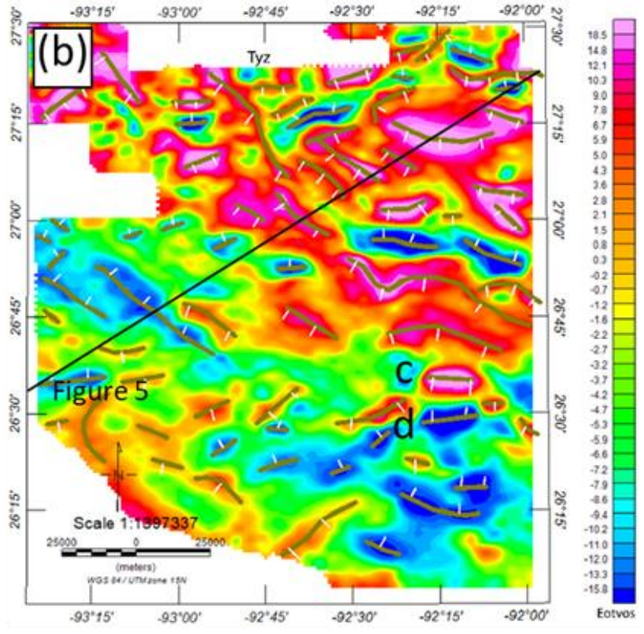
(b)
Tyz
c
d
Figure 5
Scale 1:1997337
25000 0 25000
(meters)
WGS 84 / UTM zone 15N
-93°15' -93°00' -92°45' -92°30' -92°15' -92°00'
27°30' 27°15' 27°00' 26°45' 26°30' 26°15'
18.5 14.8 12.1 10.3 9.0 7.8 6.7 5.9 5.0 4.3 3.6 2.8 2.1 1.5 0.8 0.3 -0.2 -0.7 -1.2 -1.6 -2.2 -2.7 -3.2 -3.7 -4.2 -4.7 -5.3 -5.9 -6.6 -7.2 -7.9 -8.6 -9.4 -10.2 -11.0 -12.0 -13.3 -15.8
Eotvos

(c)
Base of salt map from gravity inversion
a
b
c
d
Figure 5
Scale 1:1397337
25000 0 25000
(meters)
WGS 84 / UTM zone 15N
-93°15' -93°00' -92°45' -92°30' -92°15' -92°00'
27°30' 27°15' 27°00' 26°45' 26°30' 26°15'
-2910 -3467 -3809 -4068 -4280 -4464 -4627 -4776 -4913 -5042 -5165 -5282 -5394 -5504 -5610 -5714 -5817 -5919 -6020 -6121 -6222 -6323 -6426 -6531 -6637 -6746 -6859 -6976 -7098 -7227 -7365 -7514 -7677 -7860 -8073 -8331 -8674 -9231
m

The average difference between the interpreted seismic and inverted gravity base salt horizons is 140 m with a standard deviation of 1360 m (Figure 5.2d). Positive values suggest the inverted base salt is deeper than the base salt horizon interpreted from seismic reflection. Therefore, the FTG data suggest that salt bodies are more deeply rooted in the northeastern and southwestern parts of the study area. The inverted base salt in the center of the study area is shallower than the seismic interpretation but provides a closer match in other parts of the study area (Figure 5.5). The lateral density contrast in the shallower section is caused by surrounding sediments and salt and the density distribution along the cross-section is shown in Figure 5.6. The combined Txz and Tyz mapping results show closures that I associate with a deeper salt area, such as between anomalies c and d in Figure 5.4c.

Figure 5.5 Dynamic Group seismic profile, oriented SW-NE (displayed in Figure 5.4), and corresponding FTG anomalies. a) FTG anomaly profiles: Txz (red) and Tyz (green). b) Seismic cross-section beneath the FTG anomaly. Arrows point in the low-density direction. Base salt comparisons are shown in the inset map. c) Base salt surface is shown on the seismic data. The yellow line is the gravity inverted base salt and the black line is the seismic interpreted base salt.

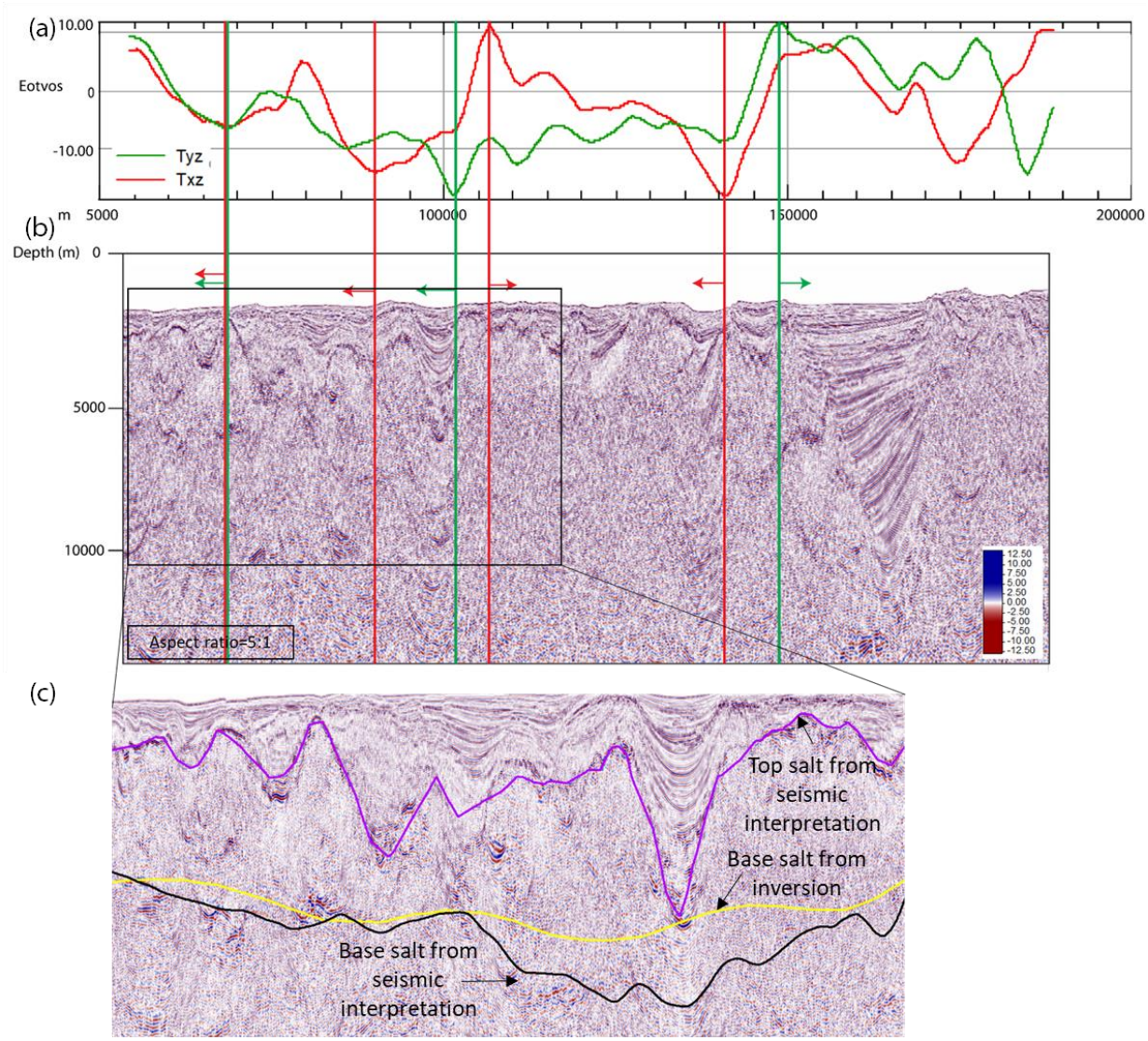

Figure 5.6 Density distribution alone the cross-section shown in Figure 5.5.

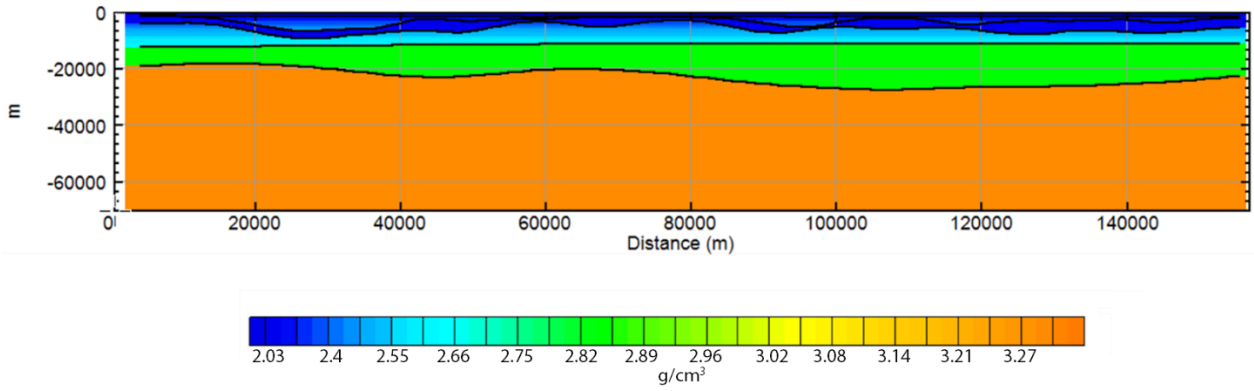

Txz and Tyz anomalies track edges of density contrasts (Figure 5.4a, b, and c), and these anomalies are interpreted to be produced by edges of salt bodies. On the Txz map, the anomalies vary from 5 km to 70 km in length (Figure 5.4a) with 30 Eotvos amplitudes. The length of anomalies on Tyz are shorter than those on Txz, ranging from 2 km to 50 km (Figure 5.4b) with -15 to 18 Eotvos amplitudes. Short wavelength Txz and Tyz anomalies are primarily located in the south, and correlate with the size of salt bodies. Hudec et al. (2013) explained that salt structures form smaller diapirs and salt-cored folds as the canopy translates seaward, and that the larger diapirs are located landward in the up-dip direction. Two possibilities may account for the distribution of FTG anomalies: 1) short-wavelength anomalies are more likely associated with smaller salt structures and long-wavelength anomalies with larger salt structures; or 2) the salt canopy near the Sigsbee escarpment is shallower and related to salt extrusion processes. This study favors the former because it is consistent with the seismic interpretation and inverse modeling results (Figure 5.2).

The interpretations indicate four-way closures over deep base salt features (Figure 5.4c). Thick salt bodies create large lateral density variations that produce FTG anomalies. The difference between modeled and seismic base salt maps (+/- 3 km) may be due to unclear base salt seismic imaging.

5.4 Conclusions

FTG directional guidance can provide a significant advantage over traditional gravity methods for seismic reflection mapping of salt canopy geometries. Although gradient anomalies, such as

Txz and Tyz, may be calculated from traditional gravity data, the resolution may be far lower (10-20 Eotvos), indicating an uplift in FTG data interpretation.

In the GOM study area, negative density contrasts are dominant for salt bodies compared to basin fill such that Txz and Tyz anomalies track edges of these low-density sources; located east and north of Txz and Tyz minima, and west and south of Txz and Tyz maxima, respectively. Mapped Txz and Tyz density source edges and modeled Tzz inversion for base salt provide independent results to integrate with interpretations of seismic data.

5.5 Bibliography

Bell, R. E., Anderson, R., Pratson, L., 1997. Gravity gradiometry resurfaces. *The Leading Edge*, vol.16, no. 1, p. 55–59.

BOEM website, 2017. "BOEM Northern Gulf of Mexico deepwater bathymetry grid from 3D seismic". Retrieved from: https://www.boem.gov/Gulf-of-Mexico-Deepwater-Bathymetry.

Bott, M. H. P., 1973. Inverse methods in the interpretation of magnetic and gravity anomalies, 133–162.

Chavarria, J.A., Routh, P.S., Kisabeth, J.L., Jorgensen, G.J., 2006. Modeling gravity and tensor gravity data using Poisson's Equation for airborne, surface and borehole applications: US Patent No. 6,993,433 B2, ConocoPhillips Company, https://patents.justia.com/patent/6993433.

Coburn, G.W., 1998. 3D full tensor gradient method improves sub-salt interpretation, *Oil and Gas Journal*, vol. 96, no. 37, p.60–66.

Cordell, L., Henderson, R. G., 1968. Iterative three-dimensional solution of gravity anomaly data using a digital computer: *Geophysics*, v. 33, n. 4, p. 596-601.

Ebeniro, O., Sawyer, D. S., 1988. Crustal structure of the northwestern Gulf of Mexico, *93*, 9075–9092.

Etgen, J. T., Corporation, B. P., Kingdom, U., 2004. The four big challenges of subsalt i maging, AAPG International Conference Abstract, Mexico.

Filina, I., Delebo, N., Mohapatra, G., Coble, C., Harris, G., Layman, J., 2015. Integration of seismic and gravity data — A case study from the western Gulf of Mexico. *Interpretation*, *3*(4), SAC99--SAC106.

Hammer, S., 1963. Deep gravity interpretation by stripping: *Geophysics*, v. 28, n. 3, p. 369-378.

Hudec, M. R., Jackson, M. P. A., Peel, F. J., 2013. Influence of deep Louann structure on the evolution of the northern Gulf of Mexico. *AAPG Bulletin*, *97*(10), 1711–1735.

Huffman, A. C. J., Kinney, S. A., Biewick, L., Mitchell , H. R., Gunther, G. L., 2004. Gulf Coast Geology (GCG) Online — Miocene of Southern Louisiana, Version 1: *USGS Data Series* 90-A.

Huh, S., Watkins, J.S., Kasande, R., Fiduk, J.C., Bryant, S., Silver, K. E., Bradshaw, B. E., Xue, F., Xi, J., 1996. Regional structure and tectonics of the Texas shelf, in Jones, J. O. and Freed, R.L., eds., Structural framework of the northern Gulf of Mexico: *Gulf Coast Association of Geological Societies Special Publication* 39, p. 39–51.

Jackson, M. P. A., C. J. Talbot, 1989. Salt canopies: *SEPM Gulf Coast Section Tenth Annual Research Foundation Conference, Program and Abstracts*, p. 72-78.

Jones, I. F., Davison, I., 2014. Seismic imaging in and around salt bodies. *Interpretation*, *2*(4), SL1–SL20.

Jorgensen, G. J., Kisabeth, J. L., 2000. Joint 3-D inversion of gravity, magnetic and tensor gravity fields for imaging salt formations in the deepwater Gulf of Mexico. *2000 SEG Annual Meeting*.

Jorgensen, G. J., Kisabeth, J. L., Routh, P., 2001. The role of potential fields data and joint inverse modeling in the exploration of the deepwater Gulf of Mexico mini-basin province. *Petroleum Frontiers*, 18–36.

Laske, G., Masters, G., Ma, Z., Pasyanos, M. E., 2013. Update on CRUST 1.0: a 1-degree global model of earth's crust: *European Geosciences Union*, 2658.

Lehner, P., 1969. Salt tectonic and Pleistocene stratigraphy on continental slope of northern Gulf of Mexico: *AAPG Bulletin*, v. 53, p. 2431-2479.

Li, X., Chouteau, M., 1998. Three-dimensional gravity modeling in all space: *Surveys in Geophysics*, v. 19, n. 4, p. 339-368.

Liu, M., Filina, I., Mann, P., 2019. Crustal structure of Mesozoic rifting in the northeastern Gulf of Mexico from the integration of seismic and potential fields data. *Interpretation*, 1–33.

Liu, M., Bird, D.E., Mann. P., 2020. Distribution and thickness of crustal types of the Greater Gulf of Mexico region based on constrained 3D gravity inversion, *AGU Fall Meeting*.

Miroslav, B., Michael, R., Michael, L., 2013. Tutorial: the gravity-stripping process as applied to gravity interpretation in the eastern Mediterranean: *The Leading Edge*, v. 32, n. 4, p. 410-416.

Oruc, B., 2010. Depth estimation of simple causative sources from gravity gradient tensor i nvariants and vertical component. *Pure and Applied Geophysics*, *167*, 1259–1272.

Parker, R. L., 1972. The rapid calculation of potential anomalies: *Geophysical Journal of the Royal Astronomical Society*, v. 13, p. 447-455.

Parsons, M., Price, A., Bian, J., Mulcahy, S., Pawlowski, R., 2004. From 2 dimensional to 3 d imensional : Modeling the western Gulf of Mexico using recently acquired long offset seismic and gravity data. *Gulf Coast Association of Geological Societies Transactions*, *54*, 573–580.

Pawlowski, R., 1997. Gravity gradiometry in resource exploration, *The Leading Edge*, EdgeNet, January 1997, http://www.edge-online.org.

Routh, P. S., Jorgensen, G. J., Kisabeth, J. L., 2001. Base of the salt imaging using gravity and tensor gravity data. *SEG Technical Program Expanded Abstracts*, *20*(1), 1482–1484.

Schenk, R. L., Morris, J. J., Hall, S. A., 1996. Integrated gravity modeling of salt feature in the Mississippi salt basin. *Transactions of the Gulf Coast Association Geological Society*, *46*, 367–372.

Simmons, G. R., 1992. The regional distribution of salt in the northwestern Gulf of Mexico: Styles of emplacement and implications for early tectonic history, unpublished d issertation, Texas A&M University, 197 p.

Straume, E. O., Gaina, C., Medvedev, S., Hochmuth, K., Gohl, K., 2019. GlobSed: updated total sediment thickness in the world's oceans: *Geochemistry, Geophysics, Geosystems*, v. 20, p. 1756-1772.

Zuo, B., Hu, X., 2015. Edge detection of gravity field using eigenvalue analysis of gravity gradient tensor. *Journal of Applied Geophysics, 114,* 263–270.

Zhdanov, M. S., Ellis, R., Mukherjee, S., 2004. Three-dimensional regularized focusing inversion of gravity gradient tensor component data. *Geophysics, 69*(4), 925–937.